Ion Beam Studies of Pure and Nanoparticle (Si, Ag) Embedded HfO_2 Thin Films

A thesis submitted by

Munthala Dhanunjaya

in the partial fulfillment of the requirement for the award of the degree of

Doctor of Philosophy

in

Physics

Under the supervision of

Supervisor: Prof. S. V. S. Nageswara Rao

and

Co-Supervisor: Prof. A. P. Pathak

School of Physics
University of Hyderabad
Central University P.O.
Hyderabad 500046
Telangana State, India

May – 2018

Dedicated to

***my* Mother**

and

Lord Sri Venkateshwara

Declaration

I, **Mr. M. Dhanunjaya,** hereby declare that the matter embodied in this thesis entitled **"Ion Beam Studies of Pure and Nanoparticle (Si, Ag) Embedded HfO_2 Thin Films"** is the result of investigations carried out by me in the School of Physics, University of Hyderabad, India, under the supervision of **Prof. S. V. S. Nageswara Rao** and **Prof. A. P. Pathak**. This work has not been submitted for any other degree either in part or in full to this or to any other University or Institution.

A report on plagiarism statistics from the University librarian is enclosed.

Place: Hyderabad **(M Dhanunjaya)**

Date: 31-05-2018 **(Reg. No. 12PHPH13)**

Certificate

This is to certify that the work embodied in this thesis entitled **"Ion Beam Studies of Pure and Nanoparticle (Si, Ag) Embedded HfO_2 Thin Films"** has been carried out by **Mr. Munthala Dhanunjaya (Reg. No. 12PHPH13)**, in partial fulfilment of the requirements for award of Doctor of Philosophy in Physics, is a bona fide work carried out by him under our supervision and guidance.

This thesis is free from plagiarism and has not been submitted previously, in part or in full to this or any other University or Institution, for an award of any degree or diploma. Further, the student has the following publications before the submission of the thesis for adjudication.

[1]. **M. Dhanunjaya,** S.A. Khan, A. P. Pathak, D.K. Avasthi and S. V. S. Nageswara Rao, "Ion Induced Crystallization and Grain Growth of Hafnium Oxide Nano-particles in Thin-films deposited by Radio Frequency Magnetron Sputtering*" J. Phys. D: Appl. Phys.* **50**, 505301, 2017 (**Chapter 4**).

[2]. **M. Dhanunjaya,** D.K. Avasthi, A. P. Pathak, S.A. Khan, and S. V. S. Nageswara Rao, "Grain Fragmentation and Phase Transformations in Hafnium Oxide induced by SHI Irradiation" (under review) (**Chapter 5**).

[3]. **M. Dhanunjaya,** A. P. Pathak and S. V. S. Nageswara Rao, "Silicon Nanoparticles Embedded in Hafnium Oxide Matrix and SHI Effects", (NIMB: Under revision) (**Chapter 6**).

[4]. **M. Dhanunjaya,** Venugopal Rao Soma, Chandu Byram, V. S. Vendamani, A. P. Pathak and S. V. S. Nageswara Rao. "Hafnium Oxide Nanoparticles Fabricated by Femtosecond Laser Ablation in Water" (to be Submitted) (**Chapter 6**).

[5]. **M. Dhanunjaya,** K. Vinod, A. P. Pathak, D. Kabiraj and S. V. S. Nageswara Rao. "100 MeV Ag Ion Assisted Ag Nanoparticles Embedded in Hafnium Oxide Matrix" (to be submitted) (**Chapter 6**).

Conference Proceedings

[1]. **M. Dhanunjaya**, N. Manikanthababu, A. P. Pathak and S. V. S. Nageswara Rao "Effect of Growth Rate on Crystallization of HfO_2 Thin Films Deposited by RF Magnetron Sputtering" *AIP Conference Proceedings*, **1731**, 080071, (2016).

Further, the student has passed the following courses towards fulfilment of coursework requirement for Ph.D.:

Course Code	Name of the Course	Credits	Pass/Fail
PY801	Advanced Quantum Mechanics	4	Pass
PY803	Advanced Statistical Mechanics	4	Pass
PY804	Advanced Electromagnetic Theory	4	Pass
PY821	Research Methodology	4	Pass

Prof. S V S Nageswara Rao
(Supervisor)

Prof. Anand P Pathak
(Co-Supervisor)

Dean
(School of Physic)

Acknowledgements

First, I would like to express my sincere thanks and gratitude to my thesis supervisors Prof. S. V. S. Nageswara Rao and Prof. A. P. Pathak, School of Physics, University of Hyderabad for their esteemed supervision, inspiration, constant encouragement, support and help throughout my research carrier. I personally and individually thank both of my supervisors.

I thank Prof. Bindu A Bambha, Dean, School of Physics and former Deans Prof. Rajendra Sing, Prof. S. Chaturvedi, Prof. S. P. Tewari for their co-operation in providing facilities and infrastructure in School of Physics. I am very privileged to have Prof. M. Ghanashyam Krishna and Dr. V. S Ashoka as my Doctoral committee members whose suggestions, encouragement and insights have improved the understanding of our results.

I express my sincere gratitude to Dr. D. K. Avasthi for his valuable suggestions during my beam time experiments at Inter University Accelerator Center (IUAC), New Delhi and during his visits to of University of Hyderabad. I thank Dr. D. Kanjilal, Director, IUAC for his useful suggestions during discussions. I express my sincere thanks to Dr. S. A. Khan (Our local experiment collaborator at IUAC) for technical discussions and help during beam time. I thank Dr. D. Kabiraj and Mr. Abhilash for allowing us to utilize the facilities in target lab. I would like to thank Mr. Sunil Ojha for his help during RBS measurements. I am also thankful to the members of Pelletron Accelerator group and other scientists at IUAC for necessary support during experiments.

I sincerely thank Prof. S. Venugopal Rao, ACRHEM and his students Mr. B. Chandu for extending his help in fabrication of Hafnium Oxide Nanoparticles by laser ablation method.

I would like to thank IUAC, New Delhi for providing fellowship under UFR project as JRF and SRF. At the same time, I would like to thank the UoH for BBL fellowship. I thank DST-SERB-ITS for their international travel support to present my work in 24th CAARI 2016 international conference in FT, Worth, Texas, USA.

I also thank personally the technical staff Mr. Durga Prasad, Mr. Lakshmi Narayana, Mr. Naresh, Ms. Sunitha, and Mr. Thirumalaiah for their help during the experiments. I would like to thank all non-teaching staff in school of physics and nano center for their help during my Ph.D. time.

I personally thank my close friends Mr. Srihari, Dr. Ajit Kumar and Dr. Siva Prasad K for sharing their experiences, views and fun times. I thank all my friends who have helped me when I was in struggle. I would like to thank my seniors Dr. V Saikiran, Dr. G Devaraju, Dr. Manikanthababu, and Dr. Vendamani for sharing their knowledge and lab experiences. I would like to thank to Mr. Arun, Mr. Vinod, and Mr. Mangababu for their help in various aspects.

It wouldn't be enough to say simply thanks to my mother, Narayanamma, who brought me where I am now. This wouldn't have happened without the contiguous and tireless support of my wife, Deepthi. I would like to express my sincere thanks to my sister, Santhi and, brother-in-law, Mallikarjun for their constant support. Also, I specially thank my sisters, Girija kumari, and brother-in-law, G V L Prasad, Sujatha and her family and all other family members for their timely support.

I would like to thank all of them who are involved either directly or indirectly for the completion of my Ph.D. successfully.

Munthala Dhanunjaya

Glossary

AC	Alternative Current
AD	As-Deposited
ALD	Atomic Layer Deposition
AN	Annealed
BRIT	Board of Radiation and Isotope Technology
C-V	Capacitance-Voltage
CFN	Center for Nano Technology
CVD	Chemical Vapor Deposition
DC	Direct Current
DIW	De Ionized Water
EB	e-beam evaporation
EDS	Energy Dispersive x-ray Spectroscopy
EHPs	Electron Hole Pairs
EOT	Equivalent Oxide Thickness
FESEM	Field Emission Scanning Electron Microscopy
FET	Field Effect Transistor
FeFET	Ferroelectric Field Effect Transistor
FS	Femtosecond
GIXRD	Glancing Incidence X-Ray Diffraction
GUI	Graphical User Interface
HRTEM	High Resolution Transmission Electron Microscope
IC's	Integrated Circuits
IFFT	Inverse Fast Fourier Transform
ISFET	Ion Sensitive Field Effect Transistor
I-V	Current-Voltage
IUAC	Inter University Accelerator Centre
JCPDS	Joint Committee on Powder Diffraction Standards
MBE	Molecular Beam epitaxy
MCSNICS	Multi Cathode Source of Negative Ions by Cesium Sputtering
ML	Multi Layer
MOS	Metal Oxide Semiconductor

MOSFET	Metal Oxide Semiconductor Field Effective Transistor
NEC	National Electrostatics Corporation
NS	Nanosecond
NVM	Non-Volatile Memory
PL	Photo Luminescence
PVD	Physical Vapor Deposition
RAM	Random Access Memory
RBS	Rutherford Backscattering Spectrometry
RCA	Radio Corporation of America
RF	Radio Frequency
ROM	Read Only Memory
MROM	Masked Read Only Memory
PROM	Programmable Read Only Memory
EPROM	Erasable Programmable Read Only Memory
EEPROM	Electronically Erasable Programmable Read Only Memory
RRAM	Resistive Random-Access Memory
SEAD	Selective Area Electron Diffraction
SF6	Sulphur Hexa-Fluoride
SHI	Swift Heavy Ion
SIMNRA	Simulation of Ions in Matter and Nuclear Reaction Analysis
SPR	Surface Plasmon Resonance
SRIM	Stopping and Ranging of Ions in Matter
TEM	Transmission Electron Microscope
T&R	Transmittance and Reflectance
UHV	Ultra-High Vacuum
UV-Vis-IR	Ultra-Violet Visible and Infra-Red
XRD	X-Ray Diffraction

Table of Contents

Declaration i

Certificate ii

Acknowledgements iv

Glossary vi

Table of content viii

Abstract xi

Chapter 1: Introduction and Motivation **1-23**

1.1 Materials of Interest: Importance of HfO_2 03

1.2 Basics of ion-solid interactions 08

1.2.1 Swift Heavy Ion (SHI) irradiation 10

1.2.2 Thermal spike model 12

1.2.3 Coulomb explosion model 13

1.3 SHI induced amorphization and crystallization 14

1.4 Objectives of the thesis 15

1.5 References 18

Chapter 2: Experimental Details **24-45**

2.1 Introduction 25

2.2 Fabrication methods 25

2.2.1 DC and RF magnetron sputtering methods 25

2.2.2 Thermal and e-beam evaporation systems 27

2.3 Sample Preparation and Description 29

2.4 Swift Heavy Ion (SHI) irradiation and ion beam studies 30

2.4.1 The 15 UD Pelletron Accelerator 30

2.4.2 Ion beam analysis: (RBS) 32

2.5 Irradiation details 34

2.6 Characterization Techniques 35

2.6.1 X-Ray Diffraction (XRD) 35

2.6.2 Field Emission Scanning Electron Microscope (FESEM) 37

2.6.3 Transmission Electron Microscope (TEM) 39

2.6.4 UV-Vis-NIR spectrometer 41

2.6.5 Micro-Raman spectroscopy 42
2.6.6 Photo Luminescence (PL) Spectroscopy 43
2.7 References 44
Chapter 3: Optimization of RF magnetron sputtering system and fabrication of HfO_2 thin films 46-66
3.1 Introduction 47
3.2 Experimental details 48
3.3 Results and discussion 50
3.3.1 Variation of deposition power 50
3.3.2 Dependence on deposition pressure 56
3.3.3 Oxidization of the HfO_2 films 60
3.4 Conclusion 64
3.5 References 64
Chapter 4: Ion induced crystallization and grain growth of hafnium oxide Nano-particles in thin-films deposited by radio frequency magnetron sputtering 67-88
4.1 Introduction 68
4.2 Experimental 69
4.2.1 Sample preparation 69
4.2.2 Swift Heavy Ion Irradiation Details 70
4.3 Results and Discussion 72
4.3.1 Synthesis and characterization of as-deposited samples 72
4.3.2 SHI induced phase transformations 75
a) Electron microscopy and diffraction 75
b) X-Ray diffraction analysis 78
c) Kinematics of the SHI induced defects 80
4.3.3 Thermal Spike Analysis and Discussion 82
4.3.4 SHI induced phase transitions in HfO_2 84
4.5 Conclusion 84
4.6 References 85
Chapter 5: Grain fragmentation and phase Transformation in HfO_2 thin films by SHI irradiation 88-110
5.1 Introduction 89
5.2 Experimental Details 91

5.2.1 Sample preparation 91
5.2.2 SHI irradiation details 91
5.3 Results and Discussion 93
5.3.1 Synthesis and characterization of as-deposited samples 93
5.3.2 SHI induced phase transformation and grain fragmentation 96
a) Surface morphology and grain fragmentation 96
b) Phase transformations and crystallinity 97
c) Ion induced reconfiguration and annihilation of defects 102
5.3.3 Thermal spike model and conclusions 105
5.4 Conclusions 106
5.4 References 107
Chapter 6: SHI Assisted Fabrication of Embedded Nanoparticles (Si and Ag) in HfO_2 Matrix and Laser Ablated HfO_2 Nanoparticles 113-141
6.1 Introduction 114
6.2 Experimental details 115
6.2.1 HfSiOx composite thin film 116
6.2.2 HfO_2 and Ag multilayer thin films 117
6.2.3 Fabrication of HfO_2 NPs by laser ablation method 118
6.3 Results and Discussion 119
6.3.1 HfO_2 and Si composite films and SHI irradiation effects 119
6.3.2 HfO_2 and Ag multilayer films and SHI irradiation effects 125
6.3.3 HfO_2 NPs by laser ablation method 130
6.4 Conclusions 136
6.5 References 137
Chapter 7: Conclusions and Scope of future work 142-144
7.1 Conclusions 142
7.2 Further outlook 145
List of publications and conferences attended 146

Abstract

Swift heavy ion (SHI) irradiation induced grain fragmentation, grain growth and phase transitions in Hafnium Oxide (HfO_2) thin films have been studied in detail. Further, nano-particles of Silicon (Si) and Silver (Ag) embedded in HfO_2 thin-films were fabricated by employing SHI irradiation and colloidal HfO_2 nano-particles were prepared in water using ultra-fast laser ablation. HfO_2 films used in this study were deposited by Radio Frequency (RF) magnetron sputtering and electron beam (e-beam) evaporation techniques. Initially, the RF sputtering system was optimized to fabricate good quality and reproducible HfO_2 thin-films. The influence of growth parameters (like RF power and Ar-pressure) and thermal annealing on the phase and stoichiometry of films was studied in detail.

It is shown that the effects of SHI irradiation critically depend on the initial state of the material. Amorphous HfO_2 Nanoparticles (NPs) were transformed into monoclinic crystallites when subjected to 100 MeV Ag ion irradiation. Whereas, the tetragonal phase was introduced into nanocrystalline films of HfO_2 under the same irradiation conditions. Irradiation-induced changes in the size and shape of grains are also found to be sensitive to their initial state. The surface of the polycrystalline films is smoothened due to grain fragmentation mediated by SHI induced relaxation of strains within the films. Photoluminescence studies suggest annealing and reconfiguration of defects during SHI irradiation. This defect rearrangement phenomenon is likely to facilitate the observed surface modifications and phase transitions in HfO_2. Thermal spike calculations have been performed for a deeper understanding of ion-induced modifications in these materials. The track diameters and damage cross-section extracted from x-ray diffraction patterns of thicker films agree with thermal spike model. Nanoparticle (Si, Ag) embedded HfO_2 thin films were fabricated by subjecting HfSiOx nano-composite thin-films and "HfO_2/Ag" multi-layers deposited by RF magnetron sputtering to SHI irradiation. SHI induced crystallization and grain growth of these NPs are studied in detail. Further, tunable colloidal HfO_2 NPs were fabricated by ultra-fast laser ablation in deionized water. HfO_2 NPs in monoclinic phase was observed when ablation was performed at lower fluences. However, at higher input energies, interestingly, both monoclinic and hexagonal phases corresponding to HfO_2 and Hf_6O were observed. Hf_6O is otherwise expected only at high pressures. These results are expected to provide useful information for understanding the electronic excitation induced modification of technologically important materials and can lead to applications in electronic and photonic devices.

Chapter 1

Introduction and Motivation

This chapter provides a brief introduction to the materials and methods that are used in this thesis.

1.1 Materials of Interest: Importance of HfO_2

Hafnium Oxide has attracted significant interest ever-since it has been envisaged as a potential gate dielectric to replace SiO_2 in Metal Oxide Semiconductor (MOS) Device Technology [1,2]. Many of its properties still need thorough investigations, although it finds its place in modern integrated circuits to meet market demands [3-5]. Most importantly the effects of ion irradiation, radiation damage, and reliability studies are critical for long-term applications, particularly when used in space and other radiation environments. On the other hand, ion-beam studies would also yield essential information to tune the properties of materials with spatial selectivity.

Hafnium Oxide, better known as hafnia with chemical formula HfO_2, is an inorganic compound and has no color. HfO_2 is the most stable and oxidized form of a metal Hafnium (Hf), which is a fourth elemental group metal in Mendeleev's periodic table like Titanium (Ti) and Zirconium (Zr). Hafnium was first discovered by Dutch physicist Dirck Costar and a Hungarian physicist Georges de Hevesy in the year 1923 while they were studying the Zirconium ores [6]. Hafnium is a byproduct of Zirconium. Since the chemical properties of both the elements are same, it was very difficult to separate them from each other. The electronic structure of the Hafnium was predicted by using X-Ray elemental analysis. Hafnium is one of the most abundant materials in the Earth's crust, and its abundance is three parts per million (ppm). The name, hafnium came after the ancient Latin name for the Danish capital city Copenhagen "Hafnia." [7]. Two years later in 1925, two scientists J. H. De Boer and A. E. Van Arkel succeeded in separation of metallic Hafnium from the Zirconium ores using crystal bar process [8]. The commercial production of Hafnium was started in 1940's. Hafnium has 600 times more neutron absorption cross section value [9] when compared to Zirconium. That is why in 1951, it was selected as a material to be used in nuclear reactor's control rods along with Zirconium [10]. United States, Russia, Japan and France used the Hafnium metal heavily for their commercial (land-based nuclear reactors for electricity generation) and military defense (nuclear submarines) applications [11, 12].

HfO_2 occurs in four different polymorphic phases [13]. HfO_2 can exist in the amorphous state from room temperature to ~500 ^oC. Monoclinic is the most stable phase at temperatures (1000 ^oC) with space group ($P2_1/c$). HfO_2 exists in tetragonal phase at temperatures ~1700 ^oC with space group ($P4_2/nmc$) and exists in cubic phase at higher temperatures > 2500 ^oC with space group (Fm-3m). The temperature induced polymorphic phases of HfO_2 are shown in Fig-1.1

and corresponding lattice parameters, space groups are shown in Table-1.1. HfO_2's melting point is about 2900 ºC, and boiling point is about 5400 ºC [14]. The temperature and pressure phase diagram of HfO_2 shown in Fig-1.2. Hafnium binary compounds are the known best refractory materials. Hafnium Boride (HfB_2), Hafnium Nitride (HfN) can sustain the very high temperatures and act as a refractory material in high-temperature ovens [15]. Materials with the HfO_2 exhibit corrosion resistant property and hence it has been used in hypersonic glide vehicles, coatings on rocket engine parts and aerospace applications [16]. The cubic phase of the hafnia has low thermal conductivity and high corrosion resistance so that it can also be used as a thermal barrier in jet and diesel engines [17]. Material properties of the HfO_2 are shown in Table-1.2.

Table1.1: The phase evaluation temperatures, lattice parameters and space group of the HfO_2.

S. No	Phase	Phase transition Temperature	Lattice parameters	Space group	Ref
1	monoclinic	>500 ºC	a=5.117 Å b=5.175 Å c=5.290 Å β=99.77	$P2_1/c$	[18]
2	Tetragonal	>1700 ºC	a=5.14 Å c=5.25 Å	$P4_2/nmc$	[19, 20]
3	Cubic	>2500 ºC	5.08 Å	Fm-3m	[21]

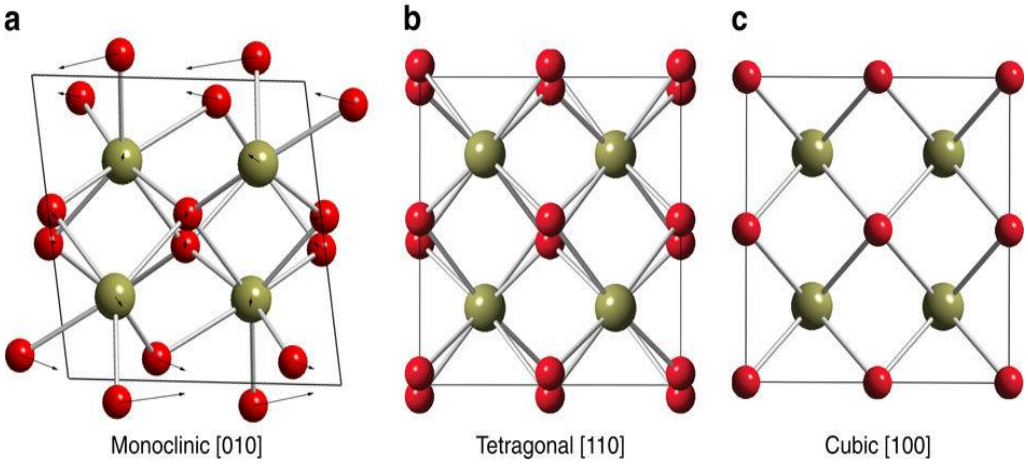

Fig 1.1: Crystal structure of the HfO_2 a) monoclinic, b) tetragonal, and c) cubic [23, 23].

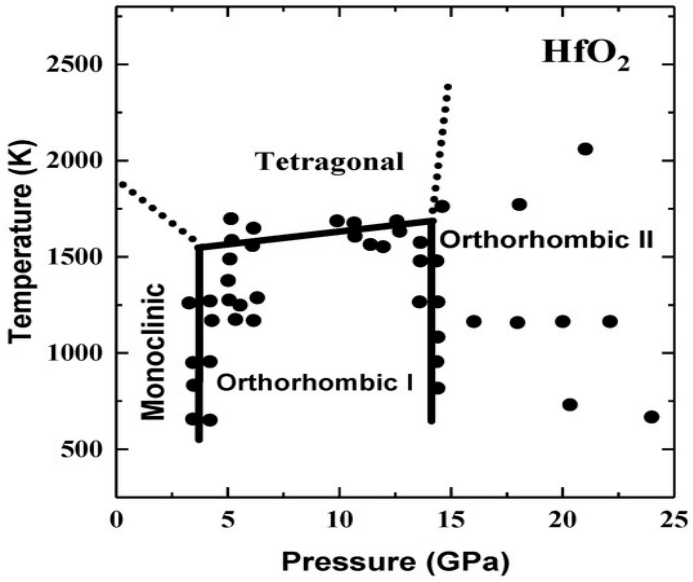

Fig 1.2: Phase diagram of HfO_2 [24].

Table1.2: Properties of the Hafnium Oxide.

Formula	HfO_2
Dielectric constant	(25 – 30)
Band gap	5.7 eV
Refractive Index	~ 2
Melting point	3000º K
Boiling point	5500º K
electron mean free path	9.2 nm
Thermal conductivity	~ 1.2 W/ (m· K) (~500 nm) at 300º K
	(0.27-0.49) W/ (m· K) (~3 nm) at 300º K
Specific heat	272 J/ kg. K
density	9.68 g/cm^3
Young's module	57 GPa
Specific Heat Capacity	120 J/kg-K
Thermal Conductivity	1.1 W/m-K
Thermal Diffusivity	0.95 m^2/s
Thermal Expansion	6.0 µm/m-K
Linear expansion	5.8X10^{-6} /k

HfO_2 is one of the high dielectric constant materials (25-30), it exhibits better-offset values, and good thermal stability with Si when compared to other high-k dielectric materials [25]. These exceptional qualities made the HfO_2 as a gate dielectric in new generation Metal Oxide Semiconductor (MOS) devices. G.E Moore predicted that the number of transistors in the integrated circuit doubles in every two years [26]. Obeying with Moore's law, the device size decreased drastically to increase the number of registry transistors on ICs. Further scaling down of a MOS structure up to the increase in leakage current in the gate oxide material SiO_2 to unacceptable levels. These high leakage currents extremely affect the device tolerance and jeopardize the performance, durability and reliability [27]. The prerequisite of reduced off-state leakage currents in MOS devices demands an innovative era of device evolution with relatively new materials to replace SiO_2 [28].

To keep up Moore's law, alternative gate oxide materials with higher dielectric constant than SiO_2 are desired. Efforts have been made to study several high dielectric materials like Al_2O_3, Ta_2O_5, Gd_2O_3, TiO_2, Er_2O_3, ZrO_2, HfO_2 etc. for their suitability to replace the SiO_2 [29, 30]. In early 2007, Intel Corporation announced that HfO_2 is the suitable replacement for SiO_2 as a gate dielectric material in metal oxide semiconductors for their next generation 45nm technology [31]. Around the same time, in 2008 IBM corporation also announced their plans for the incorporation of high-k dielectric material for their new products [32]. Because of its superior properties in microelectronics, NEC electronics also announced inclusion of hafnium Silicate Oxy Nitride compound (HfSiON) in their 55 nm ultra-low power technology [33]. The schematic diagram of the MOS is shown in Fig-1.3. The high-k dielectric materials such as HfO_2, with leakage current several orders of magnitude smaller than that of SiO_2 for the same equivalent oxide thickness (EOT) can result in superior data retention property [34].

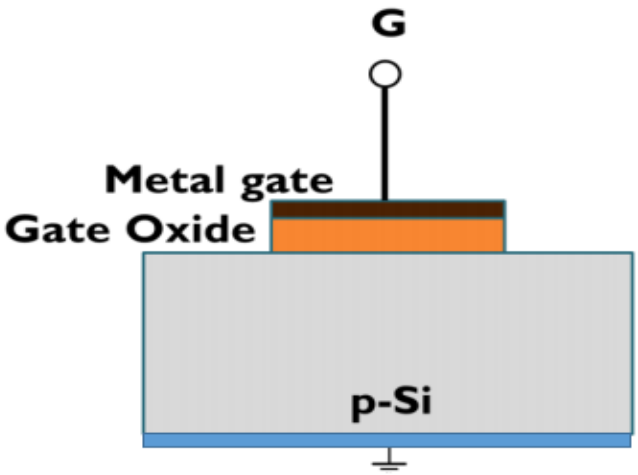

Fig-1.3: The schematic diagram of the Metal Oxide Semiconductor (MOS) structure.

Memory devices are mainly two categories: First, the devices with volatile memory also known as Random Access Memory (RAM), which lose the stored information when the power is switched off and second, the devices with non-volatile memory, also known as Read Only Memory (ROM), which do not lose the stored information even when the power is switched off. Examples of devices with volatile memory are MOS, Complementary MOS, and Dynamic RAM. While the examples of the devices with non-volatile memory include Masked ROM (MROM), Programmable ROM (PROM), Erasable Programmable ROM (EPROM), Electronically Erasable Programmable ROM (EEPROM) and flash memory devices [35]. There is a subsequent interest growing on the developments of the flash memory because of its potential for storage applications. In the recent years, much attention is being paid onto nanocrystal-based storage devices in the non-volatile memory applications [36] because of their low-cost device fabrication, better retention time due to quantum confinement effects and excellent immunity to stress-induced leakage currents. There have been numerous reports on metal (Au, Ag, Pt.,etc) and semiconductor (Si and Ge) embedded in SiO_2 [37-41]. The fact that HfO_2 has an advantage of reducing the size of the device embedded NPs in HfO_2, attains significance for NVMs. S. Tiwari et al [42, 43] have reported HfO_2 based nanoparticle (NP) non-volatile memory devices. The schematic diagram of NP embedded floating gate memory structure is shown in Fig-1.4. HfO_2 based Resistive Random-Access Memory (RRAM) is another emerging field in non-volatile memory applications [44-45].

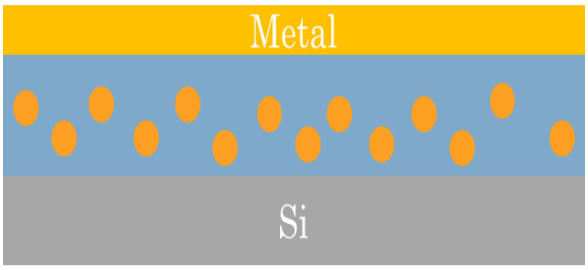

Fig-1.4: The schematic diagram of the floating gate memory structure.

HfO_2 has a high refractive index (~ 2), large bandgap (5.7 eV) [46], wide transparent range from Ultra Violet (UV) region to Infra-Red (IR) region. A fully oxidized HfO_2 film doesn't absorb radiation from 300 nm to about 10 μm. The transparency of hafnia in the near-ultraviolet (near-UV) to far-infrared (far-IR) region has various applications such as astronomical Si-based CCDs [47], night vision and IR optical devices [48], UV-IR protective layers [49, 50], solar cells antireflection coatings [51], etc.

HfO_2 exhibits better cytocompatibility with biological samples. There are reports on usage of HfO_2 nanoparticles for cancer radiotherapy. Researchers have found a unique approach to increase the radiation dose within the tumor tissue by using elements of high atomic numbers (z). Maggiorella et al. [52] have studied the flexibility of usage of HfO_2 NPs for cancer therapy. Recent studies suggested the use of cubic HfO_2 NPs in medical applications [53]. In the current scenario, the technology is tending towards nanoscale to enhance and improve the properties of these materials for various applications. HfO_2 NPs have broad-ranging applications in various fields including biomedical applications. Recent studies have shown that the inert behavior of HfO_2 NPs makes them suitable candidates for cancer therapy [54], nanocrystalline HfO_2 based biosensors [55], HfO_2 nanowire-based Ion-Sensitive Feld Effect Transistor (ISFT) for pH sensors [56], X-ray contrast agent and mid-IR biosensor [57] applications.

As mentioned earlier HfO_2 is the state of the art material in integrated circuit technology [26, 29, 31]. Many of its properties still need thorough investigations even though it has seen high usage in modern integrated circuits to meet market demands [43, 45]. Further, the effects of ion irradiation, radiation damage, and reliability studies are critical for long-term applications, mainly when used in space and other radiation environments. On the other hand, ion-beam studies would also yield essential information to tune the properties of materials with spatial selectivity. A brief discussion on ion-solid interactions and ion beam studies of materials has been presented in the following sections.

1.2 Basics of ion-solid interactions

The research on ion beams in physics dates back to more than hundred years ago. The journey started in 1911 with Rutherford's ion matter interaction in his famous gold foil experiment [58]. Following Rutherford's gold foil experiment, many researchers started the understanding of ion beams and interaction of ion beams with matter. Later in 1932, John Cockcroft and Ernest Walton developed the Cockcroft–Walton–accelerator and studied the transmutation of Lithium into Helium after irradiation with energetic protons [59]. When an energetic ion interacts with the material atoms, this leads to the modification of the material. When an accelerated ion beam is incident on solid materials, this can lead to a number of phenomena as discussed below:

When an energetic ion is incident on a solid, it interacts with atoms and molecules of that solid depending on its energy. Interaction of ions with electronic subsystems is more significant when its velocity is comparable or greater than the Bohr velocity of electrons [60, 61]. The

interaction of ions with atoms is mostly by elastic collisions and energy lost by ion in this process is called as nuclear energy loss ($\left(\frac{dE}{dx}\right)_{nuc}$ or S_n). Whereas the interactions of ions with electrons is inelastic in nature that leads to the excitations and ionization of atomic electrons. The energy lost by ions in this process named as electronic energy loss ($\left(\frac{dE}{dx}\right)_{ele}$ or S_e). Depending on the strength of these interactions, ion can pass through a maximum depth (called projected range, Rp) in a given material before they come to rest. S_e, S_n, and R_p critically depend on ion-solid combination. The charge (Z_1), mass and energy (E), of incident ion and the charge (Z_2), and density of target material are the crucial parameters as seen in following equations. The values of S_e, S_n, and R_p can be estimated for any ion-sold combination by a famous computer simulation program known as Stopping and Range of Ions in Matter (SRIM-2013) [62].

$$\left(\frac{dE}{dx}\right)_{total} = \left(\frac{dE}{dx}\right)_{elec} + \left(\frac{dE}{dx}\right)_{nuc} = -N\varepsilon(E) \qquad (1.1)$$

The ions backscattered from the beneath of surface will have less energy than those of backscattered at the surface, owing to electronic energy loss. The nuclear energy loss is depending on the elastic collision between the projectile and stable material atom. In this case, the initial momentum and final momentum conserves. The nuclear energy loss can be described by the equation,

$$\left(\frac{dE}{dx}\right)_{nuc} = \left(\frac{4\pi Z_1^2 Z_2^2 e^4 N}{v^2 M_2}\right) * \left(\frac{b_{max}}{b_{min}}\right) \qquad (1.2)$$

where N is the number of atoms per unit volume Z_1 e, M_1 and v are the projectile charge, mass, and velocity while Z_2 e, M_2 is the target atom charge and mass, b is impact parameter. Electronic energy loss is an inelastic process. Most of the projectile ion energy is shared by an electronic system of the target. The energy loss of incident ion per unit distance is calculated by multiplying the energy transfer with the differential cross section and integrates over all the impact parameters (from b_{min} to b_{max}). The electronic energy loss per unit distance is given by the equation,

$$\left(-\frac{dE}{dX}\right)_{ele} = \left(\frac{4\pi Z_1^2 e^4 n}{v^2 m}\right) * \left(ln\frac{b_{max}}{b_{min}}\right) \qquad (1.3)$$

1) If the incident ion energy is of the order of few eV (~ 5 eV), the incident ion may be absorbed into the solid or bouncing off from the solid surface may happen. In this case, the momentum of the incident ion is not enough to influence the atomic bindings of the solid.

2) If the incident ion energy is between the 5eV to 5 keV, the resulting momentum transfer between the incident ion and solid cause the electron pickup, ionization, desorption and sputtering of the solid surface will occur. The surface atoms are ejected from the solid surface when the incident ion kinetic energy overcomes the surface binding energy. Generally, the average surface binding energy and covalent bonding energy of solids are of the order of few eV (~ 5 eV). The elastic collision between the projectile ion and solid atom cause the sputtering and similarly inelastic collisions cause the ionization and charge exchange.

3) If the incoming ion energy is more than 5 keV to MeV, the projectile passes into the solid and lose their energy by either elastic scattering or inelastic scattering. In this case, phonons and secondary electrons are produced due to scattering. The average penetration depth of an ion in particular material is known as ion range. The ion range may vary depending on the material and typically ion range varies from 1 nm to several μm. The resulting phenomena of Ion implantation is the most important technique for semiconductor and certain device fabrication.

4) The swift ions lose their energy by two main processes 1) transferring to target electrons known as electronic energy loss (Se), transferring the energy to target atoms known as nuclear energy loss (Sn). The stopping cross section describes the energy loss of swift ion in the material per unit length as given in below equations [63, 64]. In addition to that, ionization, sputtering of the target atoms, defect creation in the target, charge state modification takes place in the process of ion irradiation. The SHI irradiation and consequent effects will be discussed in the following sections.

1.2.1 Swift Heavy Ion (SHI) irradiation:

Irradiation of a material with high energy ions has imperative effects on the electrical and optical properties of materials. SHI irradiation is a versatile technique to modify various materials, nanoparticles and embedded nanostructures in the materials [65]. Along with, ion beams can be used as a tool to synthesize the materials as well as characterize the materials [66]. Smaller systems of ion accelerators are used for basic studies in physics [67], chemistry [68], medicine [69] and nano-electronics [70] applications. The ion energies, ion flux, fluence,

and temperatures affect their respective phenomenon like sputtering, preferential sputtering by surface modification and nanostructures.

SHI irradiation is a unique method to modify the material in a controlled manner. With SHI irradiation, one can increase the critical current density, improve the magnetism in magnetic materials, create the nanostructure materials for sensor devices applications and modify the nanostructured materials that are embedded in dielectrics for memory applications. SHI can attain energies in the order of MeV/amu and can travel with 15 % of velocity of light. The subsequent energy losses create damage in cylindrical zone throughout the ion path known as "ion track." The ion track diameter can range between 1 nm to several nm and purely depend on the type of material and ion energy. There are few models explaining the energy transfer mechanism in the material and the main emphasis in these models is on describing energy transfers from projectile to the material. For example, "thermal spike model" explains the lattice heating, that can lead to melting, vaporization and thermal quenching via track formation. The "Coulomb Explosion model" mainly focuses on the formation of charged cylindrical zones along the ion tracks and leading to atomic displacements. "Self-trapping exciton model" explains the high concentrated excitons created and consequent defect formation. The "Bond weakening model" explains the atomic bonding which excludes the physical parameters.

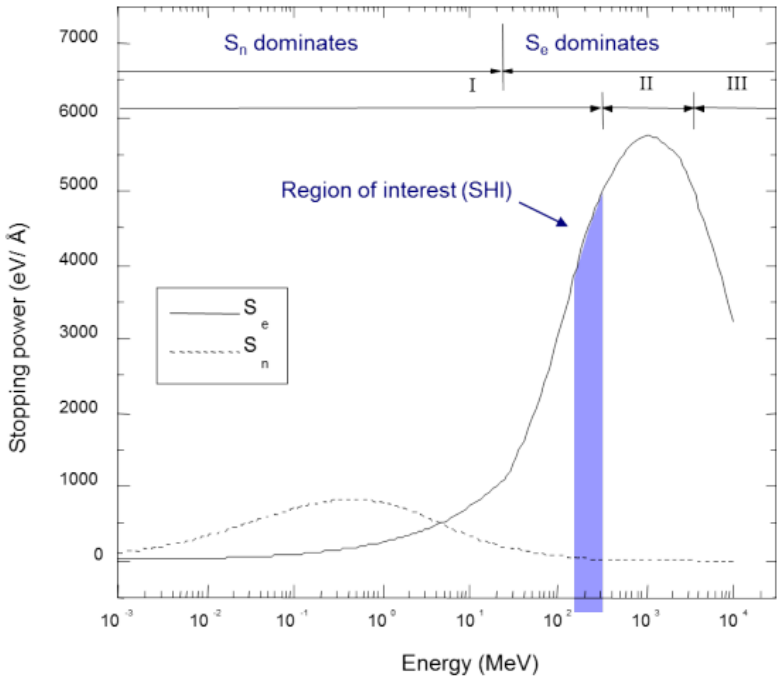

Fig-1.5: Stopping powers calculations of ions in the range of 10 keV to 10 GeV, calculated using the Monte-Carlo software SRIM-2003 [71].

Among all these models the thermal-spike and Coulomb explosion models are prominent to explain the latent track formation and subsequent effects. A model of the formation of the latent track during SHI irradiation is shown in Fig-1.5.

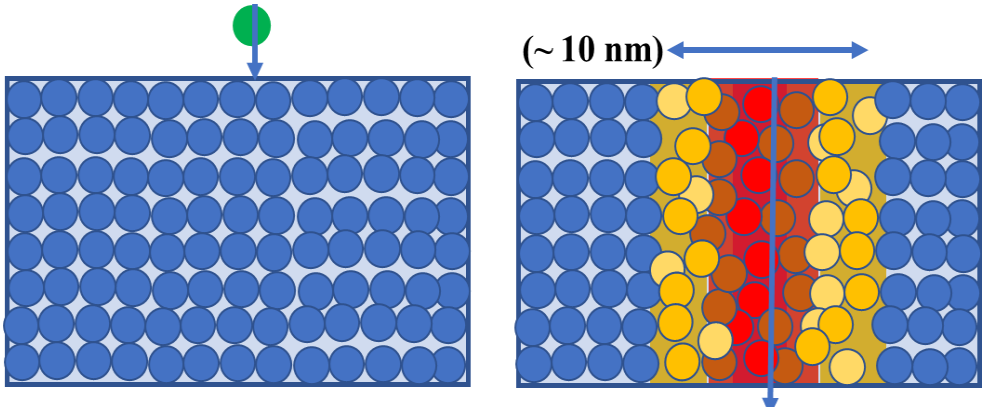

Fig-1.6: Sketch diagram of SHI irradiation.

1.2.2 Thermal spike model:

Thermal spike model [72] is used to explain the structural modifications and track formation in materials. The thermal spike model is also responsible for the defect creation or annihilation and phase transformations in the material. This model accounts for the atomic and electronic systems separately. Thermal spike model explains the transient energy converted to the thermal energy in the subatomic system. Initially, the energetic ions share their energy with the target electrons, known as ionization process. The excited electrons ionize and jump to conduction band leaving a hole in the valence band. This process happens on the time scale of 10^{-17} sec, just like a delta distribution. The excited incoherent electrons interact with the target electrons and lose their energy via quasi-thermal distribution. This process happens within 120 fs after the excitation. The electron-electron interaction increases the electronic temperatures. The quasi-thermal electrons in the conduction band further lose their energy via electron-phonon interaction. This process happens on the time scale of 1-10 ps after the excitation. In this situation, the sharp rise of temperature in the target material attains the melting temperatures [73, 74]. The affected region is around 1-100 nm diameter along the ion trajectory known as ion track. The track diameter depends on the irradiation parameters and irradiated material. In this process, the rate of quenching of the raised temperature will be 10^{14} K/s. This model can be explained by time-dependent coupled partial differential equations that represent the heat transfer between the two systems.

$$C_e \frac{\partial T_e}{\partial t} = \frac{1}{r}\frac{\partial}{\partial r}\left[rK_e \frac{\partial T_e}{\partial r}\right] - g(T_e - T_\alpha) + A(\mathrm{r,t}) \qquad (3.3)$$

$$C_a \frac{\partial T_a}{\partial t} = \frac{1}{r}\frac{\partial}{\partial r}\left[rK_a \frac{\partial T_a}{\partial r}\right] \mp g(T_e - T_\alpha) \quad (3.4)$$

where C_e *and* C_a are specific heats of electronic and atomic subsystems, respectively, K_e, K_a are thermal conductivities. T_e, T_a are electronic and atomic temperatures. g is electron phonon coupling parameter and r is the radial distance. The coupled differential equations predict the rise of temperature in the sub atomic lattice.

1.2.3 Coulomb explosion model :

The "Coulomb explosion" is another model to explain the SHI ion interaction with the mater and track formation. The major difference between the thermal-spike model and Coulomb explosion models are difference in SHI energy is transformation into the subatomic lattice. The similar way in the above case, the SHI energy transferred to the material electrons in the time scale of 10^{-17} sec. The excited electron cloud produces charge separation in the SHI passage region. The transiently produced positive charge core repel each other cause a track formation, which is called "Coulomb explosion" model [75]. The transiently generated electric field is enough to overcome the bond strength of the material and cause the displacements of atoms in the ionic core. Fleisher, Price, and Walker [76] established the Coulomb explosion model for causing of ion tracks in solids. They define the sensibility of atomic displacement concerning the physical parameters of a solid as follows

$$\sigma_e = \frac{ne^2}{\varepsilon a_0^4} \quad (3.5)$$

Where σe is the electronically generated stress in the ion core, e is the charge, n is the charge state, ε is the dielectric constant of a material and a_0 is the average separation between the atoms. The condition for the electrostatic stress exceeding the mechanical strength of a material is defined by

$$n^2 > R = \frac{Y\varepsilon a_0^4}{10e^2} \quad (3.6)$$

Here, Y is Young's modulus, R is the stress ratio considered for sensitivity of track formation in solids. The interatomic force or tensile strength of a material depends on Young's modulus of the material [77]. Coulomb explosion model is more prominent in insulators and semiconductors than the metals where neutralization and screening is much faster than lattice relaxation. Plasmon frequencies are much higher than phonon frequencies [78]. Therefore, electrons return to their vacant orbitals much faster than lattice atoms can move.

1.3 SHI induced amorphization and crystallization

Metal oxide semiconductors and binary oxides like ZrO_2, HfO_2 show a huge response to SHI irradiation. Generally, the binary oxides are radiation resistant materials; they show defect creation but no significant changes due to irradiation. Some materials in the same category are more prominent to show the radiation response. They show changes in chemical composition and a phase transition including amorphization. The initial state (sub-oxides) of the material plays a critical role in radiation response. For example, ThO_2 irradiation by Au ions up to 2.2 GeV induces only point defects through single impact mechanism [79, 80]. UO_2 shows defect tracks annihilation via precipitation of loops, due to irradiation [81]. Some of the fluoride samples show grain growth and grain fragmentation during irradiation [82, 83]. These materials show resistance to the SHI irradiation and manage somehow, to produce/ annihilate the defects. Amorphization is commonly observed in complex oxides like SiO_2, Al_2O_3, alpha- SiO_2 up to several MeV/amu for several ions [84, 85]. They all undergo the structural relaxation during SHI irradiation. "O" vacancy concentration and diffusion play an important role for the structural relaxations after exceeding certain critical defective region [86]. Although some computational models suggest that, even though the thermal spike leads the material to melting temperatures inside the track, multiple ion impact mechanism could lead to the amorphization of material. This effect has been observed in ZrO_2 and Al_2O_3 also [87].

In some other cases, the material shows the phase transition depending on the initial phase and irradiation conditions. In this category, ZrO_2 and HfO_2 are the best examples and amorphous to monoclinic, monoclinic to tetragonal phase transitions have been reported in the literature [88, 89]. ZrO_2 and HfO_2 materials exhibit different polymorphic phases concerning the temperature. The similar kind of phase transition has also been observed in Dy_2O_3 and TiO_2 powders also [90]. The grain size, chemical composition, initial phase and oxygen defects play a critical role in phase transformation of material or thin films.

Metal and semiconductor NPs that are embedded in the dielectric matrix have applications in electronics, optoelectronics, and plasmonic applications [91, 92]. Especially metal and semiconductor NPs embedded in the HfO_2 matrix have proved suitable for non-volatile memory and plasmonic applications [93]. The NPs shape, size, and surrounding environment can alter the surface plasmon resonance peak position [94]. SHI irradiation has a unique capability feature of creating tracks in insulators. The SHI induced ion tracks can tailor the properties of embedded NPs within the track diameter [95]. These are few observations made

after studying the literature of SHI induced modifications of materials and NPs [96-99]. Hence it is important to elucidate the underlying mechanisms.

1.4 The objective of the thesis

The aim of this thesis is to study the effects of SHI irradiation on the structural and optical properties of HfO_2 films and NS's that are embedded in HfO_2 matrix. In brief, the motivations are: 1) To optimize the RF sputtering system for preparation of HfO_2 thin films, and NP embedded HfO_2 thin films. 2) To fabricate the HfO_2 films at those optimized conditions and further study the SHI irradiation effects on these films and nature of evolution of defects during irradiation, 3) To fabricate the Ag/HfO_2/Ag multilayered structure and study the SHI induced effects on their optical and structural modifications and 4) To perform SHI assisted fabrication of Si and Ag NPs embedded in HfO_2 and laser ablated HfO_2.

Chapter-1: Introduction and Motivation

Chapter 1 outlines the motivation and aim of the present thesis work. This chapter explains the importance of the currently used materials and signifies the research needs in the cutting edge of the scientific field. The literature survey provides detailed information about the existing knowledge in this area. This chapter briefly explains the need for the present work and possible areas in which this dissertation is to build up.

Chapter-2: Experimental Methods

Chapter 2 describes the synthesis of the films, various characterization techniques and facilities employed to investigate the present work. HfO_2 thin films were synthesized by a newly installed RF magnetron sputtering system in our School. Some of the samples were prepared by electron beam (e-beam) evaporation method at Inter University Accelerator Center (IUAC), New Delhi. These samples were characterized by Grazing Incident X-Ray Diffraction (GIXRD), Field Emission Scanning Electron Microscope (FESEM), Transmission Electron Microscopy (TEM), Photo Luminescence (PL), Profilometer and optical spectroscopy at University of Hyderabad while the Rutherford Backscattering Spectroscopy (RBS) measurements were performed at IUAC, New Delhi. This chapter also explains the working principle of 15 MV Pelletron accelerator facility at IUAC, New Delhi. Applicability of Thermal spike and Coulomb explosion models to understand the results on HfO_2 based materials have been discussed. In essence, the details of the experimental setups, the basics of experimental methods and characterization techniques are described in this chapter.

Chapter-3: Fabrication of Hafnium Oxide Thin Films by RF Magnetron Sputtering

Chapter 3 gives the information about the optimization of RF magnetron sputtering system to fabricate HfO_2 thin films by various techniques. Good quality HfO_2 thin films were deposited on Si and quartz substrates after the optimization of the RF magnetron sputtering machine. Characterization techniques such as RBS, GI-XRD, FESEM, and Profilometer techniques have been employed. The thickness of the HfO_2 films increased linearly with an increase in RF power. At lower deposition powers, the HfO_2 grains are spherical and deposition at higher powers led to irregular grain growth. The thickness of the HfO_2 films decreased with increase in deposition pressure. The porosity in the films increased with increase in deposition pressure. We noticed that 60 W power and 10 mtorr deposition pressure are a possible for fabricating HfO_2 thin films. Films annealed up to 400^oC have shown amorphous nature and further annealing at higher temperatures showed monoclinic nature. These results suggest that reliable HfO_2 films have been synthesized and can be used for further studies with the optimized conditions.

Chapter-4: Ion Induced Crystallization and Grain Growth of Hafnium Oxide Nano-particles in Thin-films deposited by RF Magnetron Sputtering

In this chapter, we report on the SHI irradiation induced crystallization and grain growth of HfO_2 NPs, within the HfO_2 thin-films deposited by RF Magnetron sputtering technique. As grown films consisted of large amorphous clusters of non-spherical HfO_2 NPs. These amorphous clusters are transformed into crystalline clusters under 100 MeV Ag ion irradiation. These crystallites are found to be spherical and well dispersed within the films. The average size of these crystallites are found to increase with fluence. Pristine and irradiated films have been characterized by High Resolution Transmission Electron Microscopy (HRTEM), Selected Area Electron Diffraction (SAED), GIXRD and PL measurements. The PL measurements suggested the existence of different types of oxygen-related defects in pristine and irradiated samples. The observed results on crystallization and grain growth under the influence of SHI are explained within the framework of thermal spike model. The results are expected to provide useful information for understanding the electronic excitation induced crystallization of NPs and can lead to useful applications in electronic and photonic devices.

Chapter-5: Swift Heavy Ion Induced Grain Fragmentation and Phase Change in Thick Hafnium Oxide Films

This chapter explains the ion-induced surface modifications and phase transformation in HfO_2 films. Thick HfO_2 films (~ 500 nm) were deposited by RF magnetron sputtering method at high RF powers (~ 120 W) and were irradiated by 100 MeV Ag ion. As grown HfO_2 films were in monoclinic phase, self-oriented nano-flake structure due to high deposition rates and film growth conditions adopted in this study. Phase transformation and grain fragmentation within the film were investigated by studying the change in peak areas and peak widths of various peaks in the GIXRD patterns. After irradiation, the films got transformed from monoclinic to tetragonal phase. The obtained damage cross sections, ion track radii from the normalized GIXRD peak areas and averaged GIXRD peak widths are in agreement with each other. The FESEM data further confirms the grain fragmentation. The grain size (long axis) varied from 70 nm to 15 nm with increase in irradiation fluences. PL emission confirms the shallow oxygen defects and F-centers present in HfO_2 films. After irradiation, some of the defect states disappeared while some other defect states were not modified much. The grain fragmentation, phase transformation, and defect annihilation have been discussed in detail with respect to ion irradiation in the framework of thermal spike model.

Chapter-6: SHI Assisted Fabrication of Silicon (Si) and Silver (Ag) NPs Embedded in Hafnium Oxide Matrix and Laser Ablated HfO_2 NPs.

This chapter presents the synthesis of "HfO_2-Silver" multilayer structures deposited by the e-beam evaporation method and Si co-doped HfO_2 films by RF magnetron sputtering method respectively. In these HfO_2-Silver multilayer structures, one set of samples were kept at room temperature and another set of samples were annealed at 500º C. All these multilayered structures, co-doped samples, and annealed samples were irradiated with 100 MeV Ag ions using different ion fluences at IUAC New Delhi. GIXRD, PL, FESEM and optical measurements were performed at the University of Hyderabad and RBS measurement was performed at IUAC New Delhi on all these samples. Changes observed in the structural and optical characteristics as a function of fluence and relevant physical mechanisms for all these samples will be discussed in detail. HfO_2 pellets were subjected to laser ablation at different energies. It was found that pure HfO_2 NPs are formed at lower energies and hafnium sub-oxide hexagonal (Hf_6O) with rhombohedral structure have been formed at higher energies. The particle size increased with the laser energy. HfO_2 exhibits distinct phases depending on the

synthesis conditions; some are pressure-induced phase transitions, while others are temperature-induced phase transitions. All these phase transitions depend on "Hf" and "O" concentration levels as well.

Chapter-7: Conclusion and Scope of Further Work

This chapter summarizes the overall work done in this thesis and provides the scope and outlook for the possible future investigations in this field.

1.5 References

1. W. J. Zhu and Tso-Ping Ma, *IEEE Electr. Device. Lett.* **23**, 2 (2002).
2. Buhro W.E. and Colvin V.L., *Semiconductor nanocrystals: Shape matters, Nat. Mater.* **2**, 138-139 (2003).
3. Jermey N, A. Matthews, *Phys Today* **61**, 25 (2008).
4. M. L. Green, E.P. Gusev, R. Degraeve, E.L. Garfunkel, *J. Appl. Phys*. **90**, 2057 (2001).
5. T.D. Dongale, K.V. Khot, S.V. Mohite, S.S. Khandagale, S.S. Shinde, V.L. Patil, S.A. Vanalkar, A.V. Moholkar, K.Y. Rajpure, P.N. Bhosale, P.S. Patil, P.K. Gaikwad, R.K. Kamat, *J. Nano- Electron. Phys*, **8**, 04030 (2016).
6. D. Coster, G. de Hevesy, *Nature*, **111**, 2777, 79-80 (1923).
7. Weast, Robert CRC, Handbook of Chemistry and Physics. Boca Raton, Florida: Chemical Rubber Company Publishing. pp. E110 (1984).
8. Van Arkel, A. E., de Boer, J. H, **148**, 345–350 (1925). *(https://doi.org/ 10.1002/ zaac. 19251480133)*
9. Roland Tricot, *J. Nuc. Mat.* 189, 277-288 (1992)
10. E. Wuchina, E. Opila, M. Opeka, W. Fahrenholtz, and I. Talmy, *Elec. Soci. Inter.* **16**, 30-34 (2007).
11. V.D. Riso vary, E.P. Kolochkov, V.B. Ponomarenko, *American Nuclear Society* / ASM International Russian Materials Monograph Series. (2001).
12. B.G. Arabey, V. V. Chekunov, Atomizdat, Russian editors Klochkov E.P, Risovany V. D. *Hafnium in Nuclear Engineering*, **10**, 12-16 (1987).
13. Terki, R, Bertrand, G, Aourag, H & Coddet, C, *Mater. Lett.* **62**, 1484-1486 (2008).
14. T. D. Huan, V. Sharma, G. A. Rossetti, Jr. R. Ramprasad, Phys. Rev. B **90**, 064111 (2014).
15. Steven Munnoch, Avon Metals Ltd.

16. J.F. Justin, A. Jankowiak, *J. of Aero. Lab*, Issue-3 (2011).
17. J. Wang, H. P. Li, and R. Stevens, *J. Mater. Sci.* **27**, 5397-5430 (1992).
18. J. Adam and M. D. Rodgers, *Acta. Crystallogr*.**12**, 951(1959).
19. R. E. Hann, P. R. Suttch, and J. L. Pentecost, *J. Am. Ceram. Soc.* 68C-285 (1985).
20. G. B. Bokiy, *Introduction into Crystallochemistry* Moscow State University, (1954).
21. Hong Jiang, Ricardo I. Gomez-Abal, Patrick Rinke, and Matthias Scheffler, *Phys. Rev.* B **81**, 085119 (2010).
22. Q. Zeng, A. R. Oganov, A. O. Lyakhov, C. Xie, X. Zhang, J. Zhang, Q. Zhu, I. Grigorenko, L. Zhang and L. Cheng, *Acta Crystallogr., Sect. C: Struct. Chem.* **70**,76–84 (2014)
23. O. Ohtaka, H. Fukui, T. Kunisada, T. Fujisawa, K. Funakoshi, W. Utsumi, T. Irifune, K. Kuroda, and T. Kikegawa, *J. Am. Ceram. Soc.* **84**, 1369–1373 (2001).
24. Bethany M. Hudak, Sean W. Depner, Gregory R. Waetzig, Anjana Talapatra, Raymundo Arroyave, Sarbajit Banerjee, Beth S. Guiton, *Nature Communications*, **8**, 15316, (2017)
25. Akira Onodera and Masaki Takesada, *Crystals, 7*, 232 (2017).
26. G.E Moore, Progress in digital integrated electronics. in *Electron Devices Meeting*, (1975).
27. Seung-Hwan Song and Jongyeon Kim, *IEEE Electr. Device. Lett.* **61**, 11 (2014).
28. Cristian Zambelli, *IEEE Electr. Device. Lett.* **61**, 11 (2014).
29. Huang et al., "Hf-based high-k dielectrics", Advances in Solid State Technologies, P. K. Chu (Ed.)
30. Zhenjie Tang, Ma Dongwei, Zhang Jing, Jiang Yunhong, Wang Guixia, and Zhao Dongqiu, *IEEE Electr. Device. Lett.* **15**, 241-244 (2014).
31. www.chemistryworld.com/news/hafnium-oxide-helps-make-chips-smaller-and-faster/3001905.article.
32. A. Callegari, P. Jamison, D. Neumayer, F. Mc. Feely, J. Shepard, W. Andrioni, A. Curioni, and C. Pignedoli, Electrical Engineering, RC23700, W0508-110 (2005),
33. Fukase Tadashi, Nakahara Yasushi, Takahashi Toshifumi and Imai Kiyotaka, *Nec Technical Journal*, **1**, 42-46, (2006).
34. W. J. Zhu, T. P. Ma, S. Zafar and T. Tamagawa, *IEEE Electr. Device. Lett.* **23**, 597-599 (2002).
35. Patterson, David A.; Hennessy, John L. (2005). Computer Organization and Design: The Hardware/Software Interface (3rd ed.).

36. Souvik Mahapatra, S. Shukuri, and Jeff Bude, *IEEE Electr. Device. Lett.* **49**, 1296-1301 (2002)
37. Héctor Sánchez-Esquivel, Karen Y. Raygoza-Sánchez, Raúl Rangel-Rojo, Emanuele Gemo, Niccolò Michieli, Boris Kalinic, Jorge Alejandro Reyes-Esqueda, Tiziana Cesca and Giovanni Mattei, *Scientific Reports*, **7**, 5307(1-9) (2017).
38. Tiziana Cesca, Emma Vianey Garc´ıa-Ram´ırez, Hector Sanchez-Esquivel, Niccolo Michieli, Boris Kalinic, Juan Manuel Gomez-Cervantes, Raul Rangel-Rojo, Jorge Alejandro Reyes-Esqueda and Giovanni Mattei, *RSC Adv.* **7**, 17741 (2017).
39. V. Saikiran N. Srinivasa Rao, G. Devaraju, G.S. Chang and Anand P. Pathak, *Nucl. Inst. Meth.* B **315**, 161-164 (2013).
40. N Srinivasa Rao, A.P. Pathak, G. Devaraju and V. Saikiran, *Vacuum.* **85**, 927-931 (2011).
41. Eric Bersch, Sylvie Rangan, Robert Allen Bartynski, Eric Garfunkel, and Elio Vescovo, *Phys. Rev. B* **78**, 085114 (2008)
42. S. Tiwari, F. Rana, H. Hanafi, A. Hartstein, E.F. Crabbe and K. Chan, *Appl. Phys. Lett.*, **68**, 10-16 (1996).
43. Zengtao Liu, Chungho Lee, Venkat Narayanan, Gen Pei, and Edwin Chihchuan Kan, IEEE ELECTR DEVICE L **49**, 1606-1613 (2002)
44. Kwan Su Kim, Myung Ho Jung, Goon Ho Park and Won Ju Cho, *Journal of the Korean Physical Society*, **55**, 962-965 (2009).
45. Paolo Pavan, Roberto Bez, Piero Olivo, And Enrico Zanoni, *Proceedings of Ieee,* **85**, 1248-1271 (1997).
46. G. D. Wilk, R. M. Wallace and J. M. Anthony, *J. Appl. Phys.* **89**, 5243-3257 (2001).
47. The International Technology Roadmap for Semiconductors, Semiconductor Industry Association; see also http: //public.itrs.net for the most recent updates (1999).
48. M. Lesser, *Opt. Eng.* **26**, 911-915 (1987).
49. M. Fadel, O.A. Azim, O.A. Omer, and R.R. Basily, *Appl. Phys. A* **66**, 335-343 (1998).
50. A. Callegari, E. Cartier, M. Gribelyuk, J.F. Okorn-Schmidt, and T. Zabel, *J. Appl. Phys*. **90**, 6466-6475 (2001).
51. M. Toledano-Luque, E. San Andrés, A. del Prado, I. Mártil, M. L. Lucía, and G. González-Díaz, F. L. Martínez, W. Bohne, J. Röhrich, and E. Strub, *J. Appl. Phys.* **102**, 044106 (2007).
52. C. Iaru, Thesis No: PMP_15_10, Eindhoven University of Technology, 2015. (https://pure.tue.nl/ws/files/47038818/800691-1.pdf).

53. L. Maggiorella, G. Barouch, C. Devaux, A. Pottier, E. Deutsch, J. Bourhis, E. Borghi and Laurent Levy, *Future Oncol.* **8**, 1167–1181 (2012).
54. J. Shim, J. Rivera and R. Bashir, *Nanoscale* **21,** 10887-10893 (2013).
55. M. Lee, A. Baraket, N. Zine, M. Zabala, F. Campabadal, N. Jaffrezic-Renault and A. Errachid, *Sensors & Transducers.* **27**, 233-238 (2014).
56. T.L. McGinnity, O. Dominguez, T.E. Curtis, P.D. Nallathamby, A.J. Hoffman and R.K. Roeder, *Nanoscale*, **8,** 13627–13637 (2016).
57. L. Maggiorella, G. Barouch, C. Devaux, A. Pottier, E. Deutsch, J. Bourhis, E. Borghi and L. Levy, *Future Oncol.* **8**, 1167-1181 (2012).
58. *E. Rutherford. Series 6. **21**, 669–688 (1911).*
59. J.D. Cockcroft and E.T.S. Walton. *Nature*, **129**, 242-649 (1932).
60. Anand P. Pathak, Phy. Rev. B, **13**, 460-463 (1976).
61. Anand P. Pathak, *Radiation Effects & Defects in Solids*, **43**, 55-59 (1979).
62. J. F. Ziegler, "SRIM-2003". *Nucl. Instr. Meth. B.* **1027**, 219-220 (2004).
63. Jermey N. A. Matthews, *Physics Today*, **61**, 25 (2008).
64. M.L. Green, E.P. Gusev, R. Degraeve, E.L. Garfunkel, *J. Appl. Phys*. **90**, 2057 (2001).
65. Y. K. Mishra, F. Singh, and D. K. Avasthi, *Appl. Phys. Lett*. **91**, 063103 (2007).
66. S. Mohapatra, Y. K. Mishra, Jay Ghatak, and D. K. Avasthi, *Adv. Mat. Lett*. **4**, 444 (2013).
67. A. A. V. Krasheninnikov and K. Nordlund, *J. Appl. Phys.* **107**, 070301 (2010).
68. D.K. Avasthi, *Def. Sci. J.* **59**, 401-412 (2009).
69. Anand P. Pathak, *Radiation Effects & Defects in Solids*, **166**, 549–551 (2011).
70. L. C. Feldman, and J. W. Mayer "Fundamentals of surface and thin film analysis" Elsevier Science Publisher.
71. D. Fink, L.T. Chadderton, A. Kiv, A. Saad, M. Tabacnics, M. De A Rizutto, A.De O. D. Silva, W. R. Fahrner and K. H. Hoppe, *Radiation Effects & Defects in Solids*, **162**, 543-555 (2007).
72. A. Benyagoub, *Eur. Phys. J.* B **34**, 395–398 (2003).
73. M. Toulemonde, C. Dufour, A. Meftah, E. Paumier, *Nucl. Instr. Meth.* B *Beam. Interact. Atoms.* 166–167, 903–912 (2000).
74. G. Szenes, *Nucl. Instr. Meth.* B *Beam. Interact. Atoms.* **2**, 1–4 (1996).
75. M. Toulemonde, J.M. Costantini, C. Dufour, A. Meftah, E. Paumier, F. Studer, *Nucl. Instr. Meth.* B *Beam. Interact. Atoms.* **116**, 37–42 (1996).
76. A. Benyagoub, *Phys. Rev.* B **72**, 094114 (2005).

77. R.L. Fleischer, P.B. Price, R.M. Walker, *Nuclear Tracks in Solids*, University of California Press, (1975).
78. N. Itoh, D.M. Duffy, S. Khakshouri, and M. Stoneham, *J. Phys. Condens. Matter*. **21**, 474205 (2009).
79. T. Wiss, H. Matzke, C. Trautmann, M. Toulemonde, S. Klaumunzer, *Nucl. Instr. Meth.* B *Beam. Interact. Atoms.* **122**, 583–588 (1997).
80. C. L. Tracy, J. Mc Lain Pray, M. Lang, D. Popov, C. Park, C. Trautmann, *Nucl. Instr. Meth.* B *Beam. Interact. Atoms.* **326**, 169–173 (2014).
81. Manvendra Kumar, Ratnesh K. Pandey, Parasmani Rajput, S.A. Khan, Fouran Singh, D.K. Avasthi, Avinash C. Pandey, *J. Alloy and Comp.* **695**, 83-90 (2017).
82. M. Toulemonde, A. Benyagoub, C. Trautmann, N. Khalfaoui, M. Boccanfuso, C. Dufour, F. Gourbilleau, J. J. Grob, J. P. Stoquert, J. M. Costantini, F. Haas, E. Jacquet, K. O. Voss, and A. Meftah, *Phy. Rev. Lett*. 054112 (2012).
83. Anand P. Pathak, *Radiation Effects & Defects in Solids*, **61**, 1-46 (1982).
84. M. Dhanunjaya, S.A. Khan, A. P. Pathak, D.K. Avasthi and S. V. S. Nageswara Rao, *J. Phys. D: Appl. Phys.* **50**, 505301, (2017).
85. L. Douillard, J.P. Duraud, *Nucl. Instr. Meth.* B *Beam. Interact. Atoms.* **107**, 212–217 (1996).
86. A. Meftah, F. Brisard, J.M. Costantini, E. Dooryhee, M. Hage-Ali, M. Hervieu, et al., *Phys. Rev.* B. **49**, 12457–12463 (1994).
87. M. Tang, P. Lu, J. a. Valdez, K.E. Sickafus, *J. Appl. Phys.* **99**, 063514 (2006).
88. Aleksi A. Leino, Flyura Djurabekova, and Kai Nordlund, *Eur. Phys. J.* B 87, 242 (2014).
89. A. V. Krasheninnikov and K. Nordlund, *J. Appl. Phys*. **107**, 071301 (2010).
90. M. C. Ridgway, R. Giulian, D. J. Sprouster, P. Kluth, L. L. Araujo, D. J. Llewellyn, and A. P. Byrne, *Phys. Rev.* Lett. **106**, 095505 (2011).
91. A. A. Leino, F. Djurabekova, and K. Nordlund, *Current Opinion in Solid State and Materials Science*, **19**, 29-38, (2015).
92. B. Schmidt, K. H. Heinig, A. Mucklich, and C. Akhmadaliev, *Nucl. Inst. Meth*. B **267**, 1345 (2009).
93. Zengtao Liu, Chungho Lee, Venkat Narayanan, Gen Pei, and Edwin Chihchuan Kan, *IEEE Electr. Device. Lett.* **49**, 9 (2002).
94. E. Verrelli and D. Tsoukalas, *Microelectronic Engineering* **88**, 1189-11993 (2011).

95. R. Giulian, L. L. Araujo, P. Kluth, D. J. Sprouster, C. S. Schnohr, A. P. Byrne and M. C. Ridgway, *J. Phys. D Appl. Phys.* **44**, 155401, (2011).
96. Jung Yup Yang, Ju Hyung Kim, Won Joon Choi, Young Ho Do, Chae Ok Kim, and Jin Pyo Hong, *J. Appl. Phys.* **100**, 066102 (2006).
97. Jianyong Ouyang, *Organic Electronics* **14**, 1458–1466, (2013).
98. W. J. Zhu and T. P. Ma, *Ieee Transactions and Electron Devices* **25**, 2 (2004).
99. G Broglia, G Ori, L Larcher and M Montorsi, *Mater. Sci. Eng.* **22**, 065006 (2014).

Experimental Details

This chapter briefly explains the experimental methods that are used in entire thesis work. Essentially the fabrication methods, ion irradiation, working principles of various characterization techniques and equipment used, have been discussed.

2.1 Introduction

Various synthesis methods, characterization techniques, irradiation details and instruments that are used in the present thesis work, have been discussed briefly. The working principles of the different characterization techniques are pre-requisites to analyze and understand the experimented films. The pre-plan, necessary irradiation details are the crucial part of the work. The specific experimental parameters that are used in different experiments are given in the respective sections.

2.2 Fabrication methods

To complete this thesis work, Hafnium Oxide (HfO_2) thin films, HfO_2 and Silicon (Si) composite thin films, HfO_2 and Silver (Ag) multilayer thin films have been deposited using two different methods. HfO_2 films and composite thin films were deposited using a newly installed RF magnetron sputtering machine whereas multilayer films were deposited by e-beam evaporation method at IUAC New Delhi.

The above mentioned two methods belong to the Physical Vapor Deposition (PVD)techniques [1]. In these processes, solid material transforms to atomic species under applied external power. The atomic species with minimal kinetic energy (3 – 15 eV) travel through a distance (source to substrate) and get deposited on the substrate by nucleation process. As the time passes, the nucleation process increases and leads to the formation of a continuous film of desired thickness.

2.2.1 DC and RF magnetron sputtering methods:

The ejection of atoms from the surface of a target material by bombardment with energetic ions is called "*sputtering".* Sputtering is one of the PVD processes to deposit thin films. Basically, in this process the gas atoms are converted to positive ions and electrons by acquiring energy from the applied external energy source. The ionized Ar ions bombard the target surface that ejects the atoms/molecules of material. Using this sputtering process, we can deposit a wide range of materials like metals, insulators and plastics (polymers) by choosing the power supply like DC or AC. Usually, DC sputtering is employed for the metals and RF sputtering is employed for both metals and insulators. Among all the deposition processes sputtering is one of the efficient methods to fabricate the thin films. The disadvantage of both DC and RF sputtering process are the low ionization rates, which are around ~ 0.1 %. The less ionization

rates give the poor deposition rates. Another disadvantage of conventional sputtering is that it requires high Ar pressure to get the plasma, higher pressure further degrades the film quality.

When Compared to conventional sputtering process, the magnetron sputtering gives the clear advantage. The schematic representation of RF magnetron sputtering process is shown in Fig-2.1. The high strength fixed magnet beneath the target material confirms the energetic electrons in a spiral path. The confirmed electrons increase the ionization rate, which is generally 0.1-1 %. The higher ionization rates increase the deposition rates even at lower Ar pressures. After ionization, the positively charged Ar ions acquire energy in the range of 500-1000 eV.

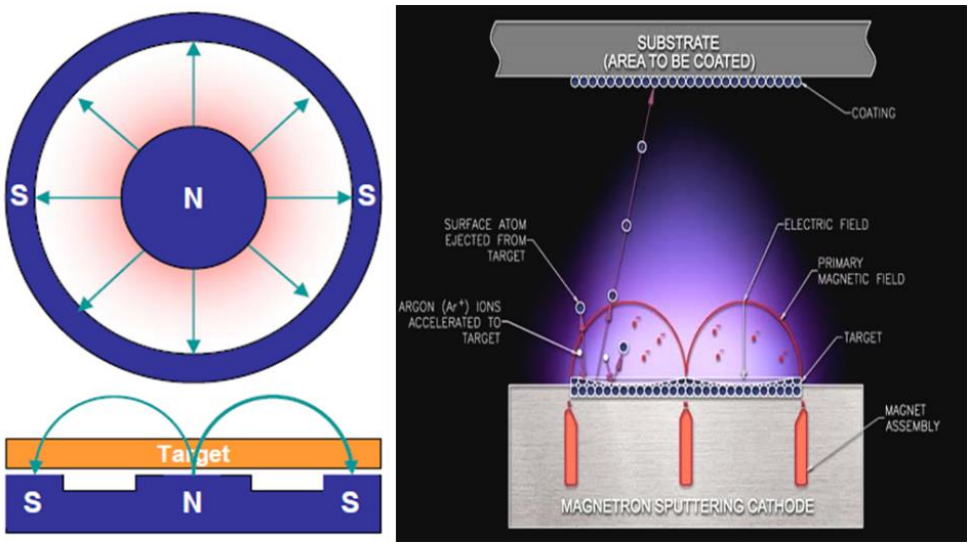

Fig 2.1. The schematic representation of magnetron sputtering process [2].

The deposition parameters like RF power, Ar pressure, and substrate to target distance can alter the film parameters greatly. In general DC sputtering voltage and currents can vary around 0.5-2 kV and 0.5 to 2 A respectively. In the case of RF sputtering the power is in the range of 30 W to 250 W according to the size of the target material. Ar pressure can vary from 5 mtorr to 50 mtorr. Sometimes both Ar and O gas can be introduced into the deposition chamber depending on the requirements. The advantages of the magnetron sputtering process are high deposition rates, low deposition pressures, better film quality, more reproducibility and control over the deposition. The disadvantages are that it requires large target material (2-inch diameter and 3 mm thickness). A picture of the newly installed semi-automatic RF Magnetron sputtering system at SOP, UOH is shown in Fig-2.2. RF magnetron sputtering system is optimized to fabricate the good quality HfO_2 thin films. At optimized conditions, thin (10-15 nm), and thick (500 nm) HfO_2 films were deposited for Swift Heavy Ion (SHI) irradiation studies. Further, HfO_2 and Si composite thin film were deposited using co-deposition process.

Fig-2.2: RF and DC magnetron sputtering system installed at SOP, UOH.

2.2.2 Thermal and e-beam evaporation systems:

Thermal and electron beam (e-beam) evaporation are well-known PVD processes for thin film deposition [3]. In both the cases the material is evaporated by applying the external energy and the evaporated material travels through a distance in vacuum and gets deposited on the substrate. Thermal evaporation is the simplest process of all the deposition systems. In this case, the evaporated material is placed on a high melting point metal (generally Tungsten or Molybdenum) boat and the applied high current or voltages can bring the material to melting temperatures. The schematic diagram of thermal evaporation system is shown in Fig-2.3(a). Whereas in the case of e-beam evaporation system, the high intense electron beam brings the material to melting point of the material. As shown in Fig-2.3(b), a powerful fixed magnet beneath the target material pocket bends the electron beam in such a way that it falls on the material. The disadvantages of both processes include the difficulty to evaporate high melting point materials, difficulty to control the film composition and the need of high vacuum to get the deposition pressure (~ 10^{-6} mbarr) compared to other systems. These methods also need high currents and high voltages. Advantages of these processes are high deposition rates, little wafer damage and excellent purity in the films.

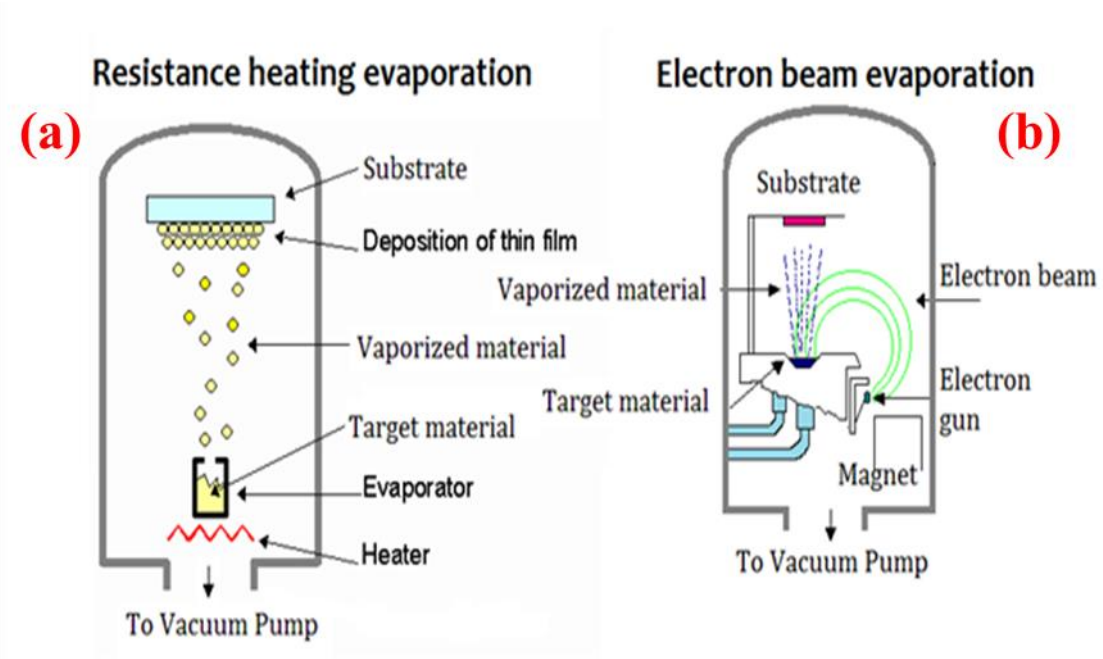

Fig-2.3: The ray diagram of a) thermal (left) and e-beam evaporation (right) systems [3, 4].

HfO_2 and Ag multilayer thin films were deposited using the above two systems. HfO_2 films were deposited by e-beam and Ag films were deposited by thermal evaporation systems layer by layer simultaneously. These depositions were carried out at IUAC New Delhi.

2.3 Sample Preparation and Description

A brief summary of sample specifications, material and characterization techniques that are used in this thesis are given in this section. Each sample series consists of many samples prepared at identical conditions. Initially, HfO_2 thin films were prepared using RF magnetron sputtering method to optimize the system. The sample preparation details are given in Table-2.1 and Table-2.2.

Table-2.1: Sample specifications and characterization details for optimization of experiments.

S. No	Parameter	Substrate	Range of parameter	Characterization techniques employed
1	Deposition power	Si and Quartz	40 to 120 W	Profilometer, RBS, FESEM, Transmission, PL
2	Deposition pressure	Si and Quartz	10 to 40 mbarr	Profilometer, RBS, FESEM, Transmission, PL
3	annealing temperature	Si and Quartz	100 to 600 ºC	Profilometer, RBS, FESEM, Transmission, PL

Table-2.2: Sample specifications and characterization details for irradiation work.

Sample Name	Preparation Method	Substrate	Sample Structure	Characterization
Set-A	RF magnetron sputtering	Si, Quartz, and TEM grids	~10 nm HfO_2 thin film/Si	TEM, XRD, FESEM, Transmission, PL
Set-B	RF magnetron sputtering	Si, Quartz	500 nm HfO_2 thick film/Si	RBS, FESEM, XRD, PL
Set-C	RF magnetron sputtering	Si, Quartz, and TEM grids	$HfSiO_x$ composite film	TEM, FESEM, XRD, Transmission, PL
Set-D	e-beam evaporation	Si, Quartz, and TEM grids	HfO_2: Ag multilayer films	RBS, TEM, FESEM, XRD, Transmission

2.4 Swift Heavy Ion (SHI) irradiation and ion beam studies

2.4.1 The 15 UD Pelletron Accelerator

SHI irradiation has been performed on the RF sputtered films and e-beam evaporated samples using 15 UD Pelletron accelerators installed at IUAC New Delhi [5]. The schematic representation of the Tandem type Pelletron accelerator manufactured by National Electrostatics Corporation (NEC) is shown in Fig-2.4. The Pelletron type accelerator can accelerate most ions from few keV to few hundred MeV [6]. Initially negative ions are produced and are pre-accelerated up to 300 keV at the ion source. The negatively charged ions are injected to the main accelerator tank with the assistance of injector magnet. The negatively charged ions accelerated towards the terminal in the robust positive electrical field. At the middle of the accelerator, terminal stage, negative ions pass through the stripper foil and get converted in to the positive ions leaving some of the electrons. Further the positive ions will be accelerated from terminal to ground potential.

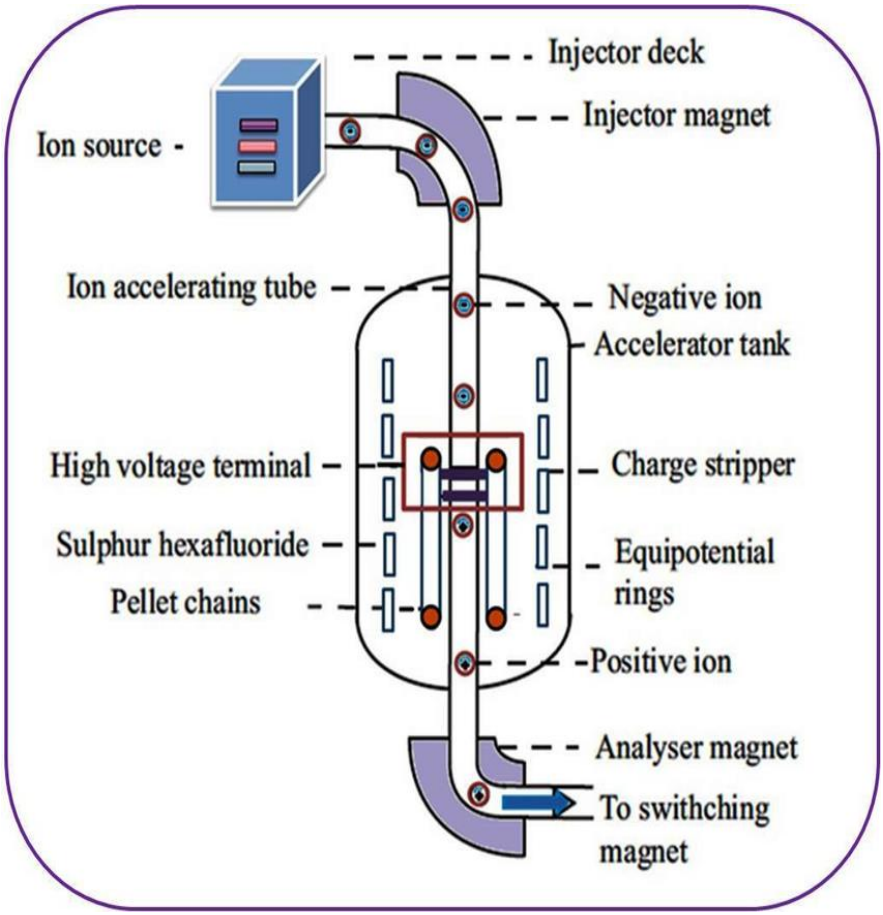

Fig-2.4: Schematic representation of IUAC Pelletron Accelerator [5].

The final energy of the ion beam can be calculated using the formula,

$$E = E_o + (q + 1)\, V_T \text{ MeV} \tag{2.1}$$

where, E_o is the initial energy of ions before acceleration, q is the charge state after stripping, V_T is the high terminal voltage at the middle of the tank. In general, V_T is few million volts generated at terminal. In IUAC New Delhi, there are seven beam lines and among these beam lines, materials science beam line is situated at 15° to the switching magnet. The accelerated ion beam can be switched to the desired beam line according to our experimental requirements. The material science irradiation beam line chamber is shown in Fig-2.5.

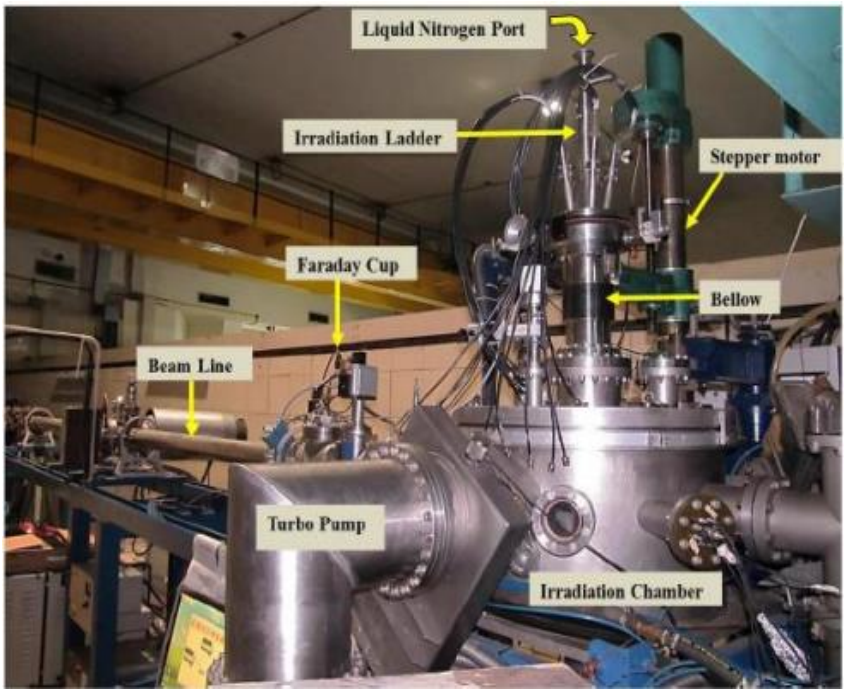

Fig-2.5: Material science beam line and irradiation chamber facilitated at IUAC [6].

The beam current can be measured by using Faraday cup (FC) as shown in Fig-2.5. FC's are facilitated along the beam lines at different stages. The irradiation ion fluence is directly proportional to the irradiation time.

$$T\ (\text{sec}) = \frac{Fluence \times A}{6.25\times10^{12}\times\frac{I}{q}} \tag{2.2}$$

where *T* is the required time (in seconds), *A* is the scan area of the material, the irradiation fluence measured in ions/cm^2, q is the charge state and *I* is the beam current which is measured by FC. In general, the beam current measured in particle nano-ampere (pnA) which is equal to the measured current divided by charge state (I/q).

2.4.1 Ion beam analysis: (RBS)

Rutherford in 1911 used the backscattering spectroscopy in his revolutionary gold foil experiment to determine the structure of atoms [7]. However, Rubin et al. [8] brought this method to modern material analysis applications. In recent years, RBS turned out to be one of the best and common techniques in material science. RBS measurements are widely used to analyze the composition of the material, thickness of the films and inter diffusion of layers of thin films. A target is bombarded by a light element (projectile) with MeV energy, which is backscattered at certain angle with a certain energy. The working principle of RBS is based on elastic collisions between the projectile and target atoms. Based on this principle, by measuring the backscattered momentum and energy, one can obtain the information about the target elements. The main advantage of the RBS is that it is very sensitive to the higher mass number elements with good depth resolution of several nm while the drawback of the RBS is low sensitivity for the lighter elements. RBS quantitatively determines the composition of the sample. For modern application purposes, generally a 2 MeV He^{2+} ions are preferred as incident projectile ions. The kinematics of the RBS is shown in Fig-2.6.

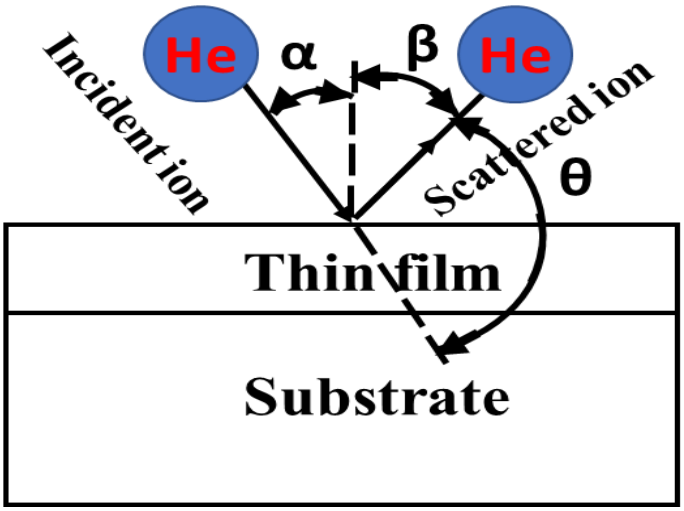

Fig-2.6: Kinetics of the RBS.

In the above diagram 'α' is the projectile incident angle to the sample normal, 'β' is the exit angle of the projectile with normal to the surface and 'θ' is the scattering angle. The kinetics of RBS is given by conservation of kinetic energy and momentum. The kinematic factor (K_{rbs}) can be expressed as,

$$K_{rbs} = \frac{E_1}{E_0} = \left[\frac{\left(M_2^{\,2} - M_1^{\,2} \sin^2 \theta\right)^{1/2} + M_1 \cos\theta}{M_2 + M_1} \right]^2 \qquad (2.3)$$

$$E_0 K_{rbs} = E_1 \quad (2.4)$$

where, M_1 and M_2 are the masses of projectile ion and target ion respectively. E_0 and E_1 are the projectile ion energy before collision and projectile ion energy after collision respectively. K_{rbs} is the kinematic factor which helps to identifying the target element precisely.

Fig-2.7: RBS facility at IUAC, New Delhi [9].

In our experiments, we have used 2 MeV He^{2+} ions to study the composition and thickness of HfO_2/Si films. RBS measurements were performed at IUAC, New Delhi. The obtained spectra were analyzed using SIMNRA simulation software to fit the spectra [10]. At the RBS facility at IUAC New Delhi, for most of our results, we used Calibration offset of 96 keV, energy per channel 0.961 keV/ch and detector resolution of 25 keV/nm that were obtained by calibration samples.

2.5 Irradiation details

All the samples of RF magnetron sputtered HfO_2 films and e-beam deposited multilayered thin films have been irradiated using 100 MeV Ag ions at different fluences from 3×10^{12} ions/cm^2 to 1×10^{14} ions/cm^2. The scanning area was chosen to be 1×1 cm^2 by using roster scan. Initially, Si and quartz substrates were pasted on middle of the ladder at separation of 1 cm each. The ladder has four sides, each side of the ladder is sufficiently stacked with the samples. The ladder

has been placed vertically into the irradiation chamber. The irradiation chamber is evacuated to a minimum pressure of 10^{-7} mbarr using high power turbo pumps. The ion current was maintained at 1 pnA to avoid the heating effect of the samples. Necessary precautions have been taken during irradiation to minimize the sample heating and channeling effects by maintaining low beam currents and 5° orientation of the sample, respectively. Irradiation details are given in Table-2.3.

Table-2.3: Sample type and irradiation details.

S. No	**Sample type**				**Fluence (Ions/cm^2)**	**Ion Energy (MeV)**
	Set-A (~15 nm)	**Set-B (500 nm)**	**Set-C (~15 nm)**	**Set-D (~15 nm)**		
1	HfO_2 -1	HfO_2 -5	$HfSiO_x$ -1	H/Ag/H– 1	Pristine	100, Ag^{7+}
2	HfO_2 -2	HfO_2 -6	$HfSiO_x$ -2	H/Ag/H – 2	3×10^{12}	
3	HfO_2 -3	HfO_2 -7	$HfSiO_x$ -3	H/Ag/H – 3	1×10^{13}	
4	HfO_2 -4	HfO_2 -8	$HfSiO_x$ -4	H/Ag/H – 4	3×10^{13}	
5	--	HfO_2 -9	$HfSiO_x$ -5	H/Ag/H – 5	1×10^{14}	

2.6 Characterization Techniques

HfO_2 films, composite films, and multilayered films before and after irradiation have been studied using suitable characterization techniques. Some of the techniques that are used for characterization are described in this section.

2.6.1 X-Ray Diffraction (XRD):

X-Rays were first discovered by German physicist W. Rontgen in 1895 [11]. Than after, two English physicists W.H. Bragg and W.L. Bragg in 1913 [12] explained the reason for the appearance of phases of crystals when exposed to X-Ray beams at certain angles. X-Ray diffraction technique is a fundamental, unique and nondestructive technique to characterize the sample to identify the phase, texture and particle/grain size of thin film or power.

The Bragg's law (Eq-2.5 and Fig-2.8) explains the diffraction patterns that are produced when X-Rays are incident on the material at certain angle. The constructive and destructive interference patterns of the reflected X-Rays reveal the information about lattice spacing, bonding angles and plane directions of the single crystal and poly crystals.

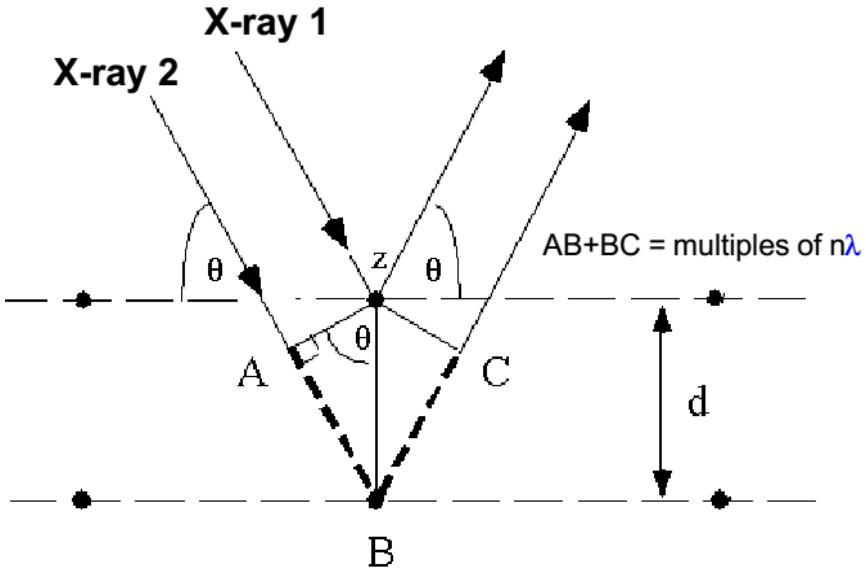

Fig-2.8: A model diagram shows the scatterings of X-Rays from crystal planes leading to X-Ray diffraction [12].

The Bragg's law can be derived as follows [12]:

$$2d\ sin\theta = n\lambda \tag{2.5}$$

where, d is the inter-planar spacing, θ is the angle between incident beam and lattice planes, λ is the wave length of X-ray and n is an integer (n=1, 2...). The average particle size or grain size calculated from the obtained peak width of the diffraction curve using Scherer equation [13] , as given below

$$d = \frac{0.9\lambda}{\beta cos\theta} \tag{2.6}$$

where λ is the wavelength of X-rays, β is the full width at half-maximum of the XRD peak and θ is the Bragg diffraction angle. Glancing Incident X-Ray Diffraction (GIXRD) is an appropriate technique to analyze thin films where the incident angle is kept very low to increase the path length through film. GIXRD measurement was performed on HfO_2 films, NPs and multilayered films using the in-house Bruker D8 Discover diffractometer, as shown in Fig-2.9. The instrument uses standard X-Ray wavelength (Cu Kα radiation, λ = 1.5405 Å). All the films

were scanned over the scan range 0º to 80º. The obtained peaks from the sample were analyzed by using Joint Committee on Powder Diffraction Standards (JCPDS) or PDF-4 software [14].

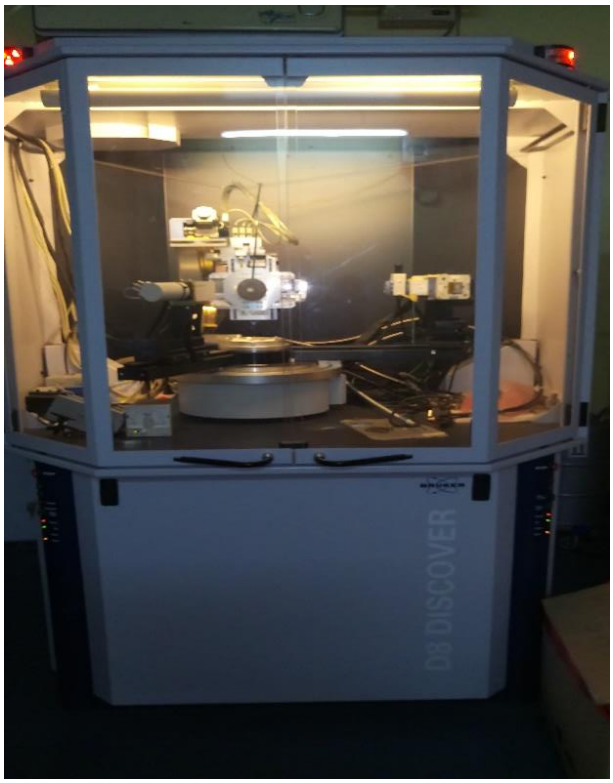

Fig-2.9: A picture of XRD instrument at SOP, UOH.

2.6.2Field Emission Scanning Electron Microscope (FESEM):

FE-SEM is an analytical technique used to study the surface morphology, structure of the material or a film surface. This technique was invented by Erwin Wilhelm Müller in 1936 [15]. The conventional microscopes are used to magnify feature size up to certain extent (10x to 100x) in real space. In the case of SEM or FESEM, energetic electrons are used to scan the surface beyond the detection lines of conventional microscopes and gives the spatial resolution up to 1 nm. A field emission scanning microscope consists of a sharp tip, usually a tungsten having tip area around 100 nm and high melting point. High energy electrons pass through the tip and can get focused at an area of 1-5 nm with the help of condenser electromagnetic lenses. The focused electron beam scans the whole surface bit by bit. Owing to interaction between electron beam and sample surface, the secondary electrons and back scattered electrons are emitted. These electrons are collected by the detector and give the electronic signal of surface morphology. The schematic representation diagram of FESEM is shown in Fig. 2.10.

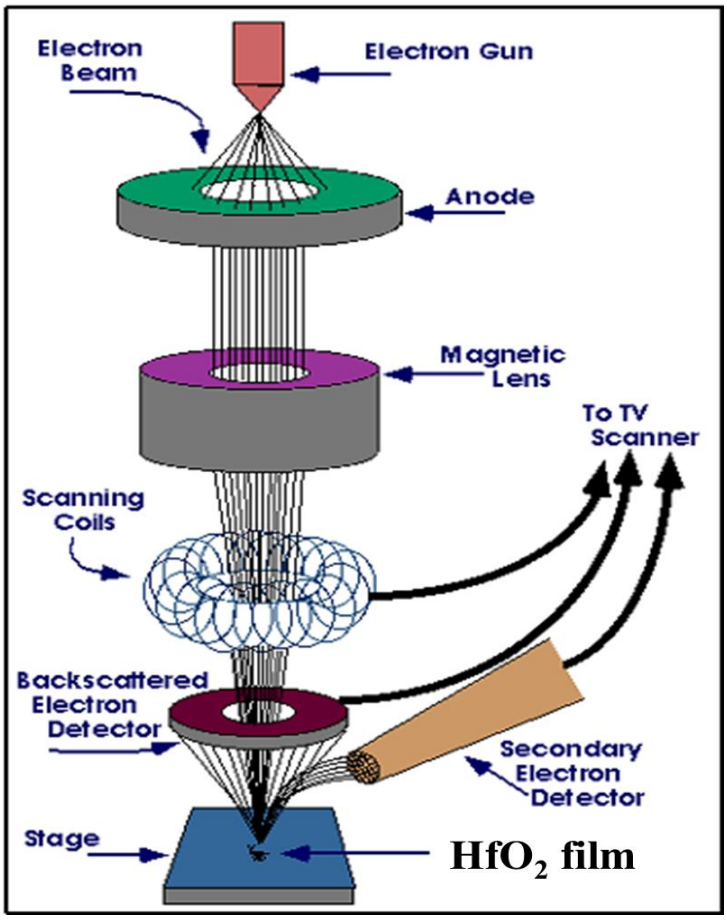

Fig-2.10: Schematic and ray diagram of a typical FESEM image [16].

The Energy Dispersive X-ray Spectroscopy (EDS) is a technique in conjunction with FESEM used to detect chemical contaminations present in the sample. X-Rays are generated when the energetic electrons interact with the sample along with secondary electrons and back scattered electrons. The electron beam ionizes the inner core shell electrons of each of element present in the sample. The inner core shells are filled by the outer electrons via emitting the characteristic X-Rays. These X-Rays are specific to the elements that are present in the sample.

In our case, we have used Field Emission Scanning Electron Microscope, model: Carl ZEISS, FEG, ultra-55 system [17] to scan the HfO_2 films, to estimate the grain sizes, to find out the Si percentage in the Si: HfO_2 co-deposited films through EDS spectrum and to find out the thickness of the HfO_2 films via cross sectional FESEM. Fig-2.11 shows the image of Carl ZEISS, FEG, ultra-55 system at SOP, UOH.

Fig-2.11: A picture of FESEM system at SoP, UoH [18].

2.6.3 Transmission Electron Microscope (TEM):

Transmission Electron Microscope (TEM) is commonly known as an electron microscopy characterization technique and is used to analyze the structural properties of a material, particle size distributions, etc. TEM is also an analytical technique in which the spatial resolution of up to 0.1 nm can be achieved. The first TEM was built by Ernst Ruska and Max Kroll in 1931 [19], but the first commercial TEM came out in 1939 [20]. A beam of electrons, having few hundreds of keV energy pass through the specimen and form the image in CCD detector. The accelerated electrons de-Broglie wavelength is much smaller than the UV-Vis light, therefore electron-beam can attain the magnification higher than the conventional microscopes. The maximum magnification of optical microscope is up to 1000 X, in the case of SEM, the magnification level is up to 100 kX, where as in the case of TEM, the magnification can be up to 500 kX. The specimen or sample thickness should be not more than 100 nm as electrons have to penetrate through the sample. The schematic representation of electron beam ray diagrams is shown in Fig-2.12.

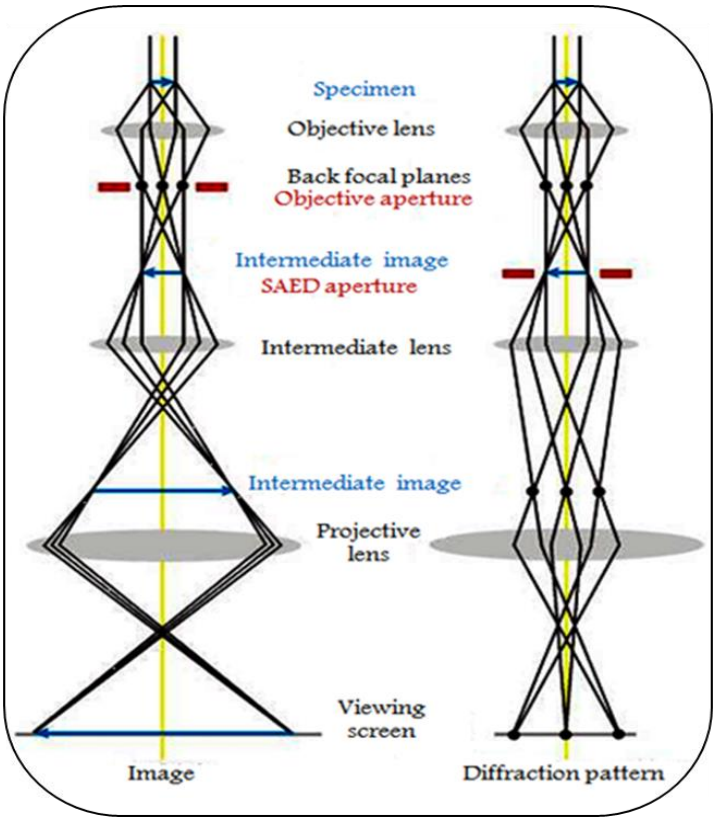

Fig-2.12: Schematic representation of TEM ray diagram [19, 20].

Generally, TEM uses the high energy electron beam (200 keV) which passes through the vacuum column of the microscope, then electromagnetic lenses which are used to focus the electron beam on to the specimen. The major portion of the electron beam passes through the specimen and is known as transmitted beam and some of the electrons get diffracted from the specimen, known as diffracted beam. We can get the specimen image by two different modes depending on the beam direction. One is bright field image mode, and another is dark field image mode. In the case of bright field image mode, the transmitted electron beam passes through the objective aperture and produces the specimen image. Where as in the case of dark field image mode, the diffracted electron beam passes through the objective aperture and produces the specimen image. In our case, we have used bright field image mode. Another advantage of the TEM is Selected Area Electron Diffraction (SEAD). SEAD can generate the diffraction patterns and images on the fluorescent screen, through which we can find out the phase of the material. Inverse Fast Fourier Transform (IFFT) calculations can also be performed. In this thesis, TEM was used to analyze SHI induced phase transformation and particle growth of HfO_2 nanoparticles and study the laser ablated HfO_2 colloidal nanoparticles. Fig-2.13 shows the TEM (*FEI Technai G2S- Twin 200 keV*) instrument installed at Center for Nanotechnology (CFN), University of Hyderabad.

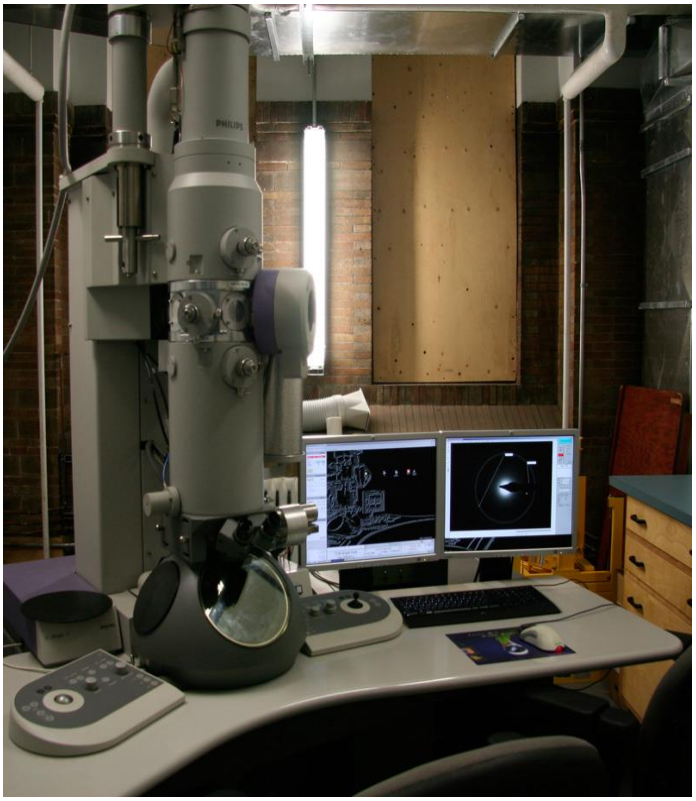

Fig-2.13: TEM (*FEI Technai G2S- Twin 200 keV*) instrument at CNF, UoH [21].

2.6.4 UV-Vis-NIR spectrometer:

It is a branch of spectroscopy that deals with the study of light matter interactions. The electromagnetic radiation ranging from UV region to IR reason falls on the sample. Some of the light is absorbed by the sample and some of the light is reflected from the surface. If the films and substrates are transparent, most of the light transmits through the film and substrate. UV-Vis-NIR spectroscopy is a measurement technique that studies the light transmitted or reflected from the sample or a film. Films deposited on quartz substrates are used to study the optical properties like reflectance, absorbance, transmittance by using UV-Vis-NIR (model: JASCO V-570) double beam spectrophotometer as shown in Fig. 2.12 [22]. In the present study, we used wavelength range from 190 to 2500 nm and performed the transmission and absorption measurements. We kept the pure quartz as a reference for these measurements. A deuterium (D_2) lamp and halogen lamp are used as sources of light for ultraviolet region and Vis-NIR region respectively. The light from the two sources get reflected from the mirror, then reflected beam passes through the slit-1 and strikes the diffraction grating placed in the same path line. The grating can act as a monochromator to select the desired wavelength. The desired monochromatic beam is passed through the slit-2 and then through the filter. The filter (high

pass/low pass) is used to process the high order diffracted beams. The processed light beam strikes the second mirror before it gets split by the half-wave plate.

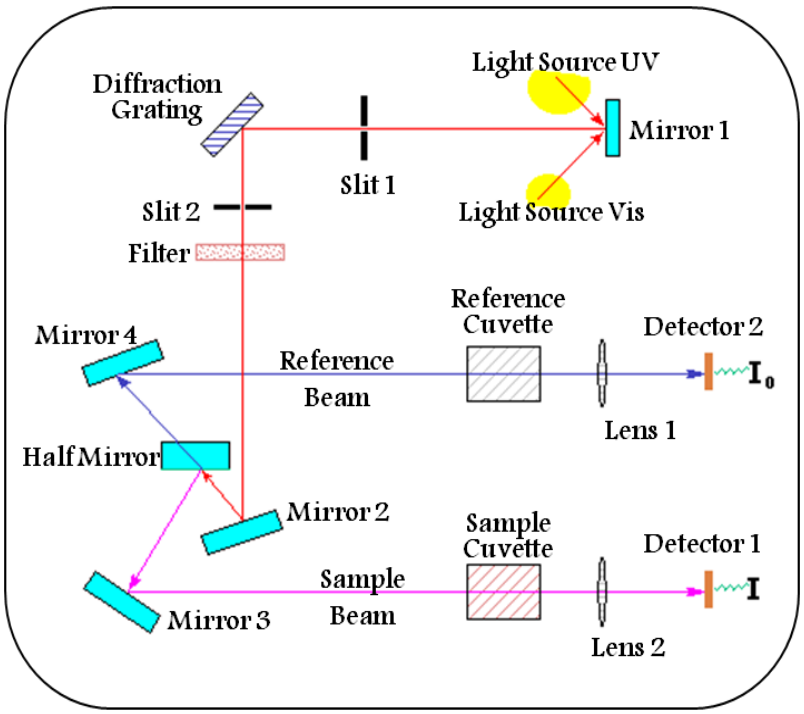

Fig-2.14: Schematic diagram of UV-Vis-NIR spectrophotometer [22].

One beam acts as a reference light with light intensity (I) and passes through the reference sample. Another beam passes through the sample (either film or cuvette) and give the intensity (I_o). the ratio between two light beam intensities (I/I_o) gives the information about the sample. Transmittance is defined as the intensity ratio between the two transmitted beams from the sample and reference, usually referred as (%T). The absorbance of a sample is defined as logarithm of ratio of two transmitted beams. the reflectance is defined as the intensity ratio between the two reflected beams from the sample and reference, usually referred as (%R).

2.6.5 Micro-Raman spectroscopy:

Micro Raman spectroscopy is a non-destructive technique that can be used to analyze the samples either for quantitative or qualitative information. Raman effect was fist observed by Prof. C. V. Raman in 1923 [23]. The basic principle of Raman effect: when light interacts with the molecule or atom, most of the light is scattered through elastic scattering process known as "Rayleigh scattering". A small portion of light scatters inelastically by excitation process. The inelastically scattered photons have signature of molecule or atom. The first micro-Raman system was introduced by Horiba scientific in 1970. This technique works on the principle of the vibrational agitations within the molecule. Each molecule has fingerprint region on wave

number which conforms the presence of that particular molecule in the prepared sample. The schematic ray diagram of micro Raman spectroscope shown in Fig-2.15.

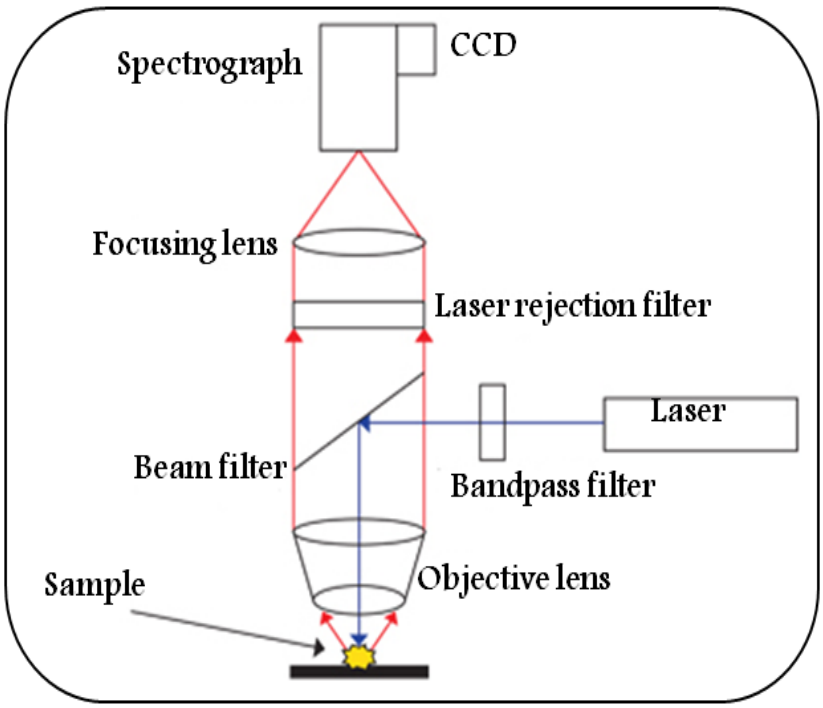

Fig. 2.15: Schematic of WITech Alpha 300 confocal micro-Raman spectrometer [24].

In this present thesis work, we have used micro Raman instrument to study the vibrational and phase of the laser ablated HfO2 NPs. This model consists of three different excitation wavelength laser sources; 1) Nd-YAG laser (*40 mW power*) having wavelength 514 nm covered in UV region and 2) a diode laser (*7 mW power*) with 785 nm wavelength covered in visible region and 3) a diode laser (*7 mW power*) with and 632 nm wavelength covered in near IR region respectively. These Raman signals are detected by the CCD (charge couple devices) detectors. A notch filter is placed before the detector to avoid the direct signal from the incident light. To position the sample under illumination spot, joystick is used which can move the sample in XY directions. The instrument is calibrated using standard single crystal Si sample before measurements.

2.6.6 Photo Luminescence (PL) Spectroscopy:

Photoluminescence is a nondestructive, non-contact method to study the electronic states and defect states of a material. When a material is excited with an electromagnetic radiation, some of the photons are absorbed by the material. The absorbed photons excite the inner electrons to the excited states and this process is called photo-excitation. The excited electrons come back

to the ground state by losing their energy via photons, this process is called photo-luminescence. Fig-2.16 shows the block diagram of a typical photoluminescence spectroscope.

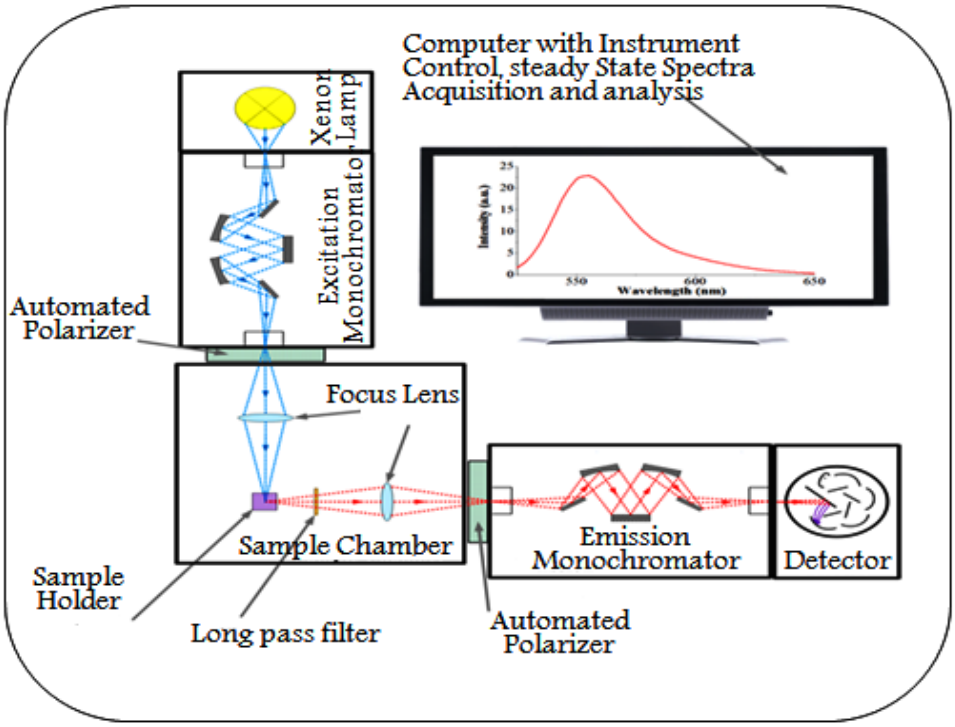

Fig. 2.16: Schematic diagram of a typical fluorescence spectrometer [25].

From this instrument we can measure the photoluminescence, phosphorescence, emission, excitation and life-time measurements. Continuous lamp used for PL measurements, pulsed lamp is used for phosphorescence measurement, diodes and spark source are used for pulsed lifetime measurements, and photodiodes are used for correction of excitation wavelength ranging from 240 to 1000nm.The excitation wavelength should be higher than the bandgap energy of the sample so that the ground state electrons are excited to higher energy states. In emission phenomenon excited electron recombine with hole at ground state or with a defect states within the bandgap. The emitted photons are collected at an angle of 45^{o} with respect to excitation light. One of the objectives of this thesis is to find out and recognize the SHI induced defect modification in HfO_2 films and to study the luminescence from Si NPs that are embedded in HfO_2 matrix. In this thesis work, the luminescence properties have been studied by using the in-house fluorescence spectrometer (model: *Flourolog1427C-AU*). For counting of the emitted photons, the standard R928P based photo multiplier was used. The light from the xenon lamp source is passed through the filter/monochromator to select desired wavelength for excitation of the sample. The collected photons are passed through the filter/monochromator before being detected by photomultiplier tube. The signal is further

processed, and output is given in either digital or analogue signal. The present equipment consists of a continuous wave Xenon lamp (450 W) as an excitation source. Using this instrument, liquid, pellet, thin film sample can be analyzed for the above-mentioned measurements.

2.7 References

1. *Selvakumar, N.; Barshilia, Harish C, Solar Energy Materials and Solar Cells.* **98**, 1–23 (2012).
2. Ohring, Milton. Materials Science of Thin Films (2nd ed.). *Academic Press*. p. 215.
3. George, J., "Preparation of thin films", Marcel Dekker, Inc., New York, 13–19 (1992).
4. R. D. Mathis Company Evaporation Sources Catalog, by R. D. Mathis Company, pages 1 through 7 and page 12, (1992).
5. http://www.iuac.res.in/accel/paras.
6. http://www.iuac.res.in/accel/pell/index.html.
7. E. *Rutherford*, Philosophical Magazine. *Series 6.* **21**, 669–688 (1911).
8. S. Rubin, T.O. Passell, and E. Bailey, Analytical Chemistry **29**, 736 (1957).
9. http://www.iuac.res.in/accel/paras/index.html.
10. M. Mayer, SIMNRA: Simulation of RBS, ERD and NRA spectra, http://www.rzg. mpg. de/~mam/
11. *Grove, Allen W, Literature and Medicine.* **16** (2), 141–173 (1997).
12. Bragg, W.H., Bragg, W.L. *Proc. R. Soc. Lond. A.* ***88****, 428–38 (1913).*
13. P. Scherrer, Göttinger Nachrichten Gesell., **2**, 98 (1918).
14. JCPDS
15. "Intro to Field Emission". *Field Emission / Ion Microscopy Laboratory, Purdue University, Dept. of Physics. Archived from* the original *on (2007).*
16. https://fas.dsi.a-star.edu.sg/equipments/auger.aspx.
17. Rudenberg, Reinhold, Patent DE906737 (1931).
18. "A Brief History of the Microscopy Society of America". *microscopy.org.*
19. L. Reimer, H. Kohl, "Transmission Electron Microscopy Physics of Image Formation", 5th Ed, Springer, New York, 10013 (2008).
20. Z.L. Wang, "Transmission Electron Microscopy of Shape-Controlled Nanocrystals and Their Assemblies", J. Phys. Chem. B **104**, 1153 (2000).
21. http://microscopy.tamu.edu/instruments/transmission-electron-microscopy/fei-technai-fe-tem.html.

22. O. Stenzel, "The Physics of thin film Optical Spectra: Introduction", Springer, Germany (1996).
23. Misra, Prabhakar*; Dubinskii, Mark, eds. (2002). Ultraviolet Spectroscopy and UV Lasers. New York:* Marcel Dekker. ISBN 0-8247-0668-4.
24. Banerjee, Somaditya, Physics in Perspective, **16** (2): 146–178 (2014).
25. Stephen M. Cohen, "Modular Spectro fluorometer-the Fluorolog-3".

Effects of Growth Parameters on HfO_2 Thin-Films Deposited by RF Magnetron Sputtering

The main objective of the work presented in this chapter is to optimize the growth parameters for preparing good quality and reproducible films of HfO_2 by RF magnetron sputtering method. A newly installed RF magnetron sputtering system is employed to accomplish this work. The effects of various growth parameters and thermal annealing are presented. Films optimized in this study were used for further studies presented in this thesis.

3.1. Introduction

Thin film is nothing but a film having the thickness ranging from few atomic layers to several nanometers or micrometers [1]. Thin films have diverse applications in the modern world like microelectronics [2], optoelectronics [3], solar cells [4] and magnetism [5]. Researchers choose their material and substrates according to their application interests. Some of the applications depend on the surface of the thin films while some other applications depend on the interface properties. As we know, when the material transforms from bulk to thin film, the material characteristics and properties will change. The increased surface to volume ratio causes the variation in their properties.

Now a days Researchers are using various methods to deposit the thin films. Researchers choose two distinct methods known as Physical Vapor Deposition (PVD) and chemical synthesis depending on material transport and film nucleation properties. In chemical synthesis method, material can be used either in solution or as gas form. Among few chemical synthesis deposition methods are, Atomic Layer Deposition (ALD) [6], Chemical Vapor Deposition (CVD) [7], sol-gel method [8], dip coating method [9] and spin coating methods [10]. Usually in these processes, material in a gas form or liquid form react with the substrate and forms the film, sometimes heating is necessary. Whereas in the case of physical deposition, material is in solid form. In this process, solid material transforms to atomic spices when subjected to the external power source. These atomic species travel through a distance from the source to substrate and get deposited by nucleation process. As the deposition time increases the nucleation process increases and leads to formation of continuous films of desired thickness. Thermal evaporation [11], and Direct Current (DC) sputtering methods are appropriate for depositing metals whereas Radio Frequency (RF) sputtering [12], e-beam evaporation [13] and Pulsed Laser Deposition (PLD) [14, 15] are useful for both insulator and metals.

Among the several deposition techniques, RF/DC magnetron sputtering is the most commonly used technique to deposit thin films in laboratory. When an external RF/DC power is applied to the depositing material in low pressure gas atmosphere, then the plasma generated ions collide with the target material. Sputtering is generally performed in inert gas (like Ar) atmosphere. Reactive gases (like O) are also introduced when needed. Present work has been performed only in Ar atmosphere. The forceful collisions between the Ar ions and target material cause the ejection of the target atoms. The ejected atomic species travel through a distance randomly and get deposited on the substrate. More and more atoms condense and form

a uniform film on the substrate. The strong magnetic field confines the plasma and electrons to ensure more ionizations within the region of interest. RF Magnetron sputtering process is more frequently used to coat the HfO_2 films for laboratory purposes, because of its good uniformity in the films, control in the film deposition, and more importantly ease of cost when compared to other systems for laboratory purposes. The Hafnium Oxide (HfO_2) is a high-k dielectric material currently under consideration in microelectronics, storage devices, solar cell and optoelectronic applications [16-19]. Each of the applications of HfO_2 films has been elaborately discussed in previous chapter.

3.2. Experimental details

HfO_2 films were fabricated by using RF Magnetron sputtering method. These HfO_2 films were deposited using a 2-inch diameter, 5 mm thickness, and 99.99 % pure commercially purchased HfO_2 target. Silicon (Si) and Quartz substrates were used to deposit the HfO_2 films to measure both structural and optical properties. All the substrates were cleaned ultrasonically in acetone, ethanol and deionized water for 5 minutes before deposition. Si substrates were pre-cleaned with a diluted HF (1:10) solution for 30 seconds to remove the native oxide on the surface. In the cleaning process, all the substrates were rinsed several times in Deionized Water (DIW) and dried with pure Ar gas to remove the water residuals. The pre-cleaned substrates were clamped to the substrate holder and immediately loaded into the sputtering chamber. Initially, the sputtering chamber was evacuated to a base pressure of 8×10^{-6} mbar. The deposition was performed using 99.99 % pure Argon (Ar) gas by allowing it into the deposition chamber.

To establish the suitable deposition conditions and to get the good HfO_2 films, a set of depositions were carried out by varying the deposition conditions like RF power, Ar pressure, annealing of the deposited films. Initially, a set of films were deposited by varying the RF power from 40 to 120 W with 20 W increment. Another set of samples deposited by varying the Ar pressure from 10 to 40 mtorr with 10 mtorr increment. Each of the deposition was carried for 90 minutes. The deposited films were studied by different characterization techniques. The thickness of deposited films were estimated by using profilometer, optical characterization (transmission spectra), Rutherford Backscattering spectroscopy (RBS) and cross-sectional Field Emission Scanning Electron Microscopy (FESEM) measurements. The deposition rate for each deposition was calculated by dividing the thickness (nm) with deposition time (minutes).

RBS measurements were performed using 2 MeV He^{2+} ions at a scattering angle of 165º. Calibration offset and energy per channel were estimated to be 96 keV and 0.961 keV/ch respectively, using a calibration sample (Au/SiO_2), to simulate the RBS spectra. These RBS measurements were carried out at Inter University Accelerator Center (IUAC), New Delhi. SIMNRA-7.1 software [20] was used to analyze the RBS data.

Bruker D8 Discover diffractometer equipped with Cu K**α** (**λ**= 1.5405Å) was used to perform the Grazing Incident X-Ray Diffraction (GIXRD) measurement. GIXRD measurement are useful to estimate the phase and grain size of the film. The scan ranges were from 20º to 80º of 2θ and glancing angle was 4º. The grain size of the films was calculated by using the well-known Scherrer's formula as given by [21].

$$d = \frac{0.9\lambda}{\beta cos\theta} \tag{3.1}$$

where λ is the wavelength of X-rays (Cu Kα radiation, λ = 1.5405 Å), β is the full width at half-maximum of the XRD peak and θ is the Bragg diffraction angle.

The optical characterization of the films deposited on quartz substrates were carried out by using UV-Vis-NIR spectroscopy. Transmittance measurements were performed in the wavelength range of 190–2000 nm using JASCO V-570 Photo Spectrometer. The optical properties of the films were calculated by using envelope method [22]. The same formulas used in envelope method scripted in MATLAB program used to fit the spectra. The refractive index of the films is derived from the equations given below [23].

$$N = 2s\frac{T_M - T_m}{T_M . T_m} + \frac{s^2+1}{2} \tag{3.2}$$

$$n = \sqrt{(N + \sqrt{(N^2 + S^2)})} \tag{3.3}$$

where n is the refractive index of the material, s is the substrate refractive index, T_M, $T_m$are the two adjacent maxima's Thickness of the films is calculated from the transmittance spectra by following equation

$$t = \frac{\lambda_1 . \lambda_2}{2(\lambda_2 n_1 - \lambda_1 n_2)} \tag{3.4}$$

where t is the thickness of the film, λ_1, λ_2 are the wavelengths of the two-adjacent consecutive maxima or minima. n_1, n_2 are the refractive indices at adjacent maxima/ minima wavelets. The

bandgap of the films was calculated by using Tauc's law [24], which is derived from the transmittance spectra. The relevant equation is as follows:

$$(\alpha h\nu) = B^*(h\nu - E_g)^p \quad (3.5)$$

where, α is the absorbance, which is derived from the transmittance spectra, hν is the photon energy, E_g is the bandgap of the material, B is the parameter of the absorption edge width. The exponent p can be determined by the type of the electronic transition. Here the superscript p value varies from 1/2 and 2 depending on the type of indirect allowed, and direct allowed transition respectively. HfO_2 is an indirect bandgap material, hence 'n' value is equal to 0.5.

FE-SEM: Carl ZEISS, FEG, ultra-55 was used to scan the surface morphology evolved grains and to measure the film thickness from the cross-sectional image. The deposited HfO_2 films have been studied using 5 kV Extra High Tension (EHT) electron gun at different magnification levels. PL measurements were performed using Fluorolog, Xenon lamp, 450 W, having a resolution of 0.3 nm. PL measurement is very useful to estimate the defects states formed in the films. Each of the films was excited with 300 nm wavelength and the emission was measured in the range of 315 to 700 nm.

3.3. Results and discussion

3.3.1. Variation of deposition power

As discussed in the above experimental section: initially, HfO_2 films were deposited on Si and quartz substrates at various deposition powers. The properties of the film, such as film thickness, morphology and quality have been studied in detail. The RF power was varied from 40 to 120 W in the interval of 20 W. We have chosen the 10 mtorr of deposition pressure to deposit these films. The thickness of the HfO_2 films has been estimated using various suitable methods as discussed in the experimental section. The values of the estimated thickness of the films from various methods have been tabulated in Table-3.1. The power density (W/cm^2) was calculated by dividing the RF power with the HfO_2 target area which is 19.6 cm^2. The growth rate has been calculated for the individual deposition powers by dividing the estimated thickness (Profilometer) with deposition time in minutes. From the observation, at lower RF power densities such as 2 W/cm^2, the coated film thickness was less, and growth rate was very low (0.4 nm/min). While increasing the power density, the film thickness and deposition rates increased linearly. This could be due to the increase in Ar ion flux which is proportional to the RF power density. The increase of Ar ion flux can increase the sputter rate and generate more

species. Hence the deposition rate or film thickness increase with RF power density. Higher deposition rates may not ensure the proper density of films, grin size, shape and stoichiometry of the films.

Table-3.1: HfO_2 films with deposition power, film thickness, and growth rates.

Deposition Power (Watt)	Power Density (W/cm^2)	Profilometer Thickness (nm)	Optical Thickness (nm)	RBS (nm)	Growth Rate (nm/min)
40	2	35	35*	--	0.4
60	3	79	79*	86	0.9
80	4	134	151	106	1.5
100	5	196	230	191	2.2
120	6	287	310	276	3.1

*- Profilometer values are used for bandgap calculations.

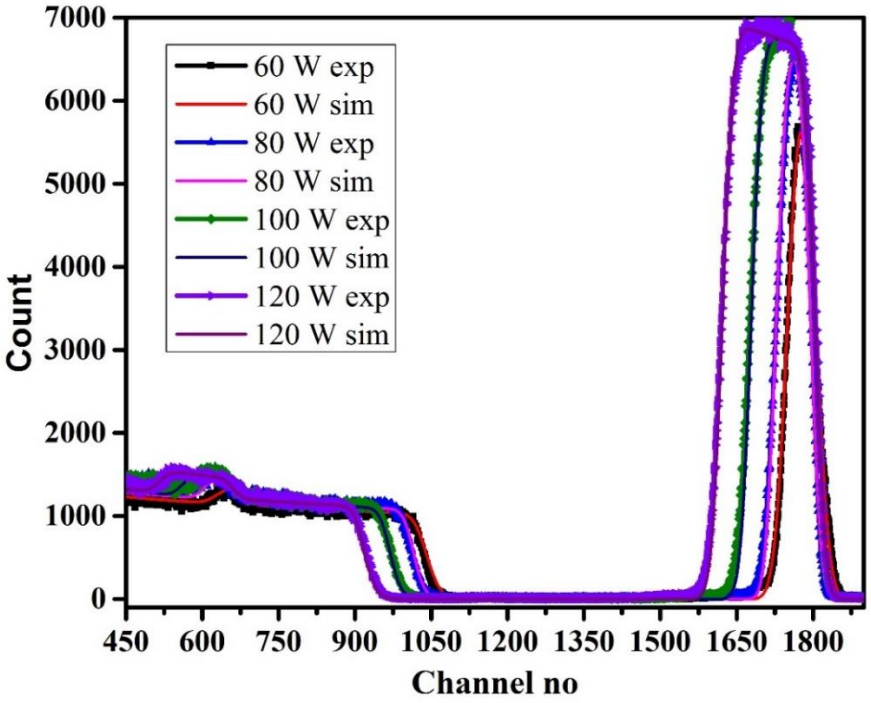

Fig-3.1: The RBS spectra and simulation spectra of the films deposited at different powers of HfO_2 (exp stands for experimental curve and sim stands for simulated curve).

The RBS spectra and their individual simulations of films deposited at various RF powers shown in Fig-3.1. Calibration offset, energy per channel were estimated to be 96.47 keV and 0.96 keV/ch respectively by using a calibration (Au/Glass) sample. These values were used to simulate the spectra. The peak showing at 1800 channel number represents the Hf peak and a small hump at 650 channel number showing 'O' peak. The areal densities of the films are calculated by simulating the spectra using SIMNRA program [20]. The physical thickness of the film is calculated by dividing it with the areal density of bulk HfO_2 which is 8.4 atoms/cm^3. Estimated areal densities from the simulations are 713, 879, 1585 and 2290×10^{15} atoms/cm^2 with respect to the deposition power densities 2, 3, 4, 5, and 6 W/cm^2 respectively. The physical thickness of the film for the above mentioned areal densities is tabulated in Table-3.1. The stoichiometry of the film $Hf_{0.27}O_{0.73}$ was obtained from the RBS measurement after simulation. The chemically active oxygen reacts with the Si substrate and can form $HfSiO_x$ interface layer while depositing the films. The interface layer thickness is increased with increase in thickness of the film noticed from the RBS measurement. The interface layer thickness was varied from 4 to 10 nm with increasing power density. The interface layer thickness depends on the interdiffusion of 'O' atoms from the grain boundaries [25].

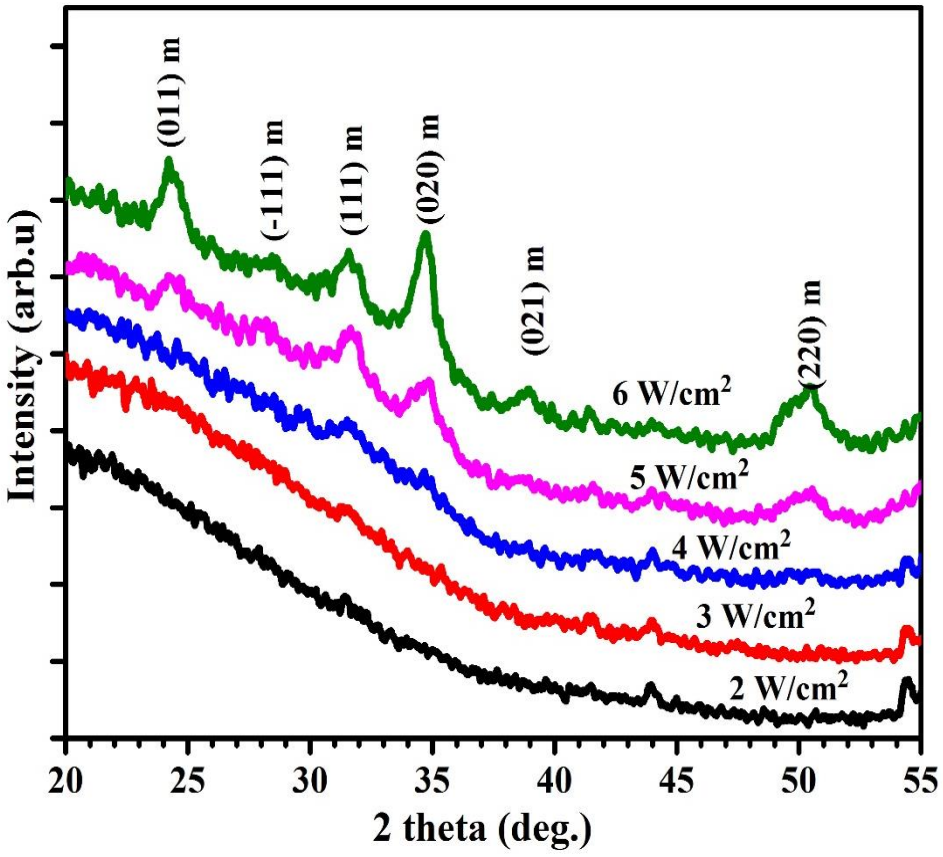

Fig-3.2: GIXRD spectra for various deposition powers HfO_2 films.

The GIXRD diffraction patterns of the HfO_2 films deposited with different RF power densities are shown in Fig-3.2. It is observed that the films deposited at lower RF power densities are of amorphous nature leaving no observable diffraction peaks. Whereas the films deposited at higher RF power densities show polycrystallinity nature. The RF power densities 2, 3 W/cm^2 almost shown amorphous nature. The small humps in diffraction patterns started at 4 W/cm^2 power density and for 5, 6 W/cm^2 clearly showed sharp and intense diffraction peaks. All the diffraction patterns of the film belong to the monoclinic phase of the HfO_2, which are well matching with the standard JCPDS file [PDF# 06-0318]. The evolved diffraction peaks at 2θ of 24.16º, 31.34º, and 34.30º corresponding to the HfO_2 (011), (111), (020) crystal plans respectively. The grain size was calculated from the Eq-3.1 as mentioned in the experimental section. The calculated grain size was around 47 nm for the highest power density of 6 W/cm^2. The exhibiting polycrystalline nature at higher RF power density leads to inference that the highly energized inert Ar ions provide translational kinetic energy to the adatoms, that can change the film density, and crystallinity [26]. The agglomeration of smaller grains coalesces together resulting in the larger grains formation with better crystallinity [27].

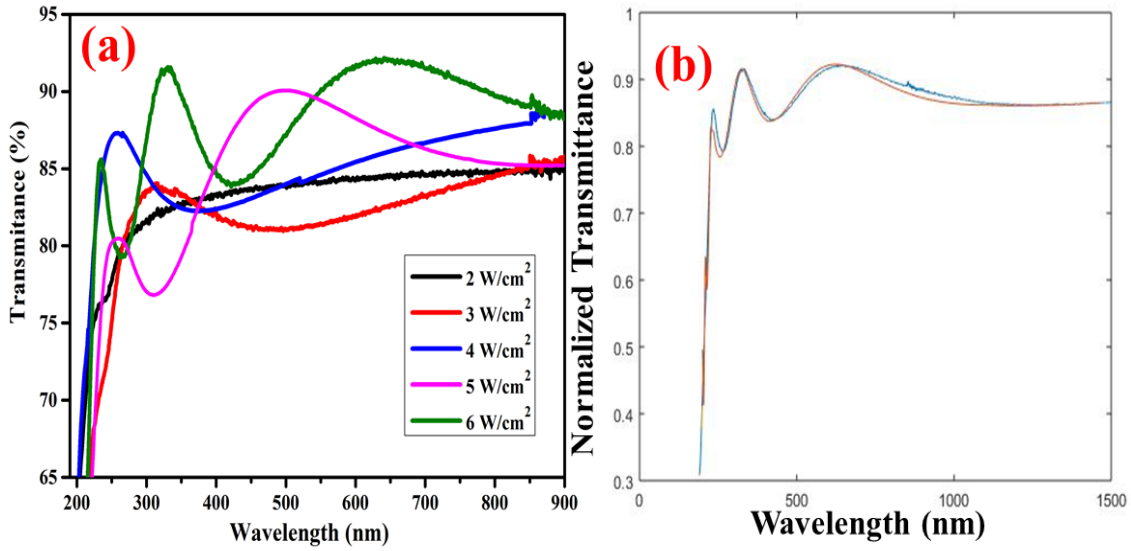

Fig-3.3: The optical properties of RF power density varied HfO_2 films: a) transmittance spectra, b) fitting of transmittance spectra for 6 W/cm^2 power.

HfO_2 films deposited on quartz substrates were characterized by UV-Vis-NIR spectroscopy. HfO_2 is a wide bandgap material of about 5.7 eV and almost transparent from near UV to far IR region. The transmission spectra of HfO_2 films deposited with various RF powers is shown in Fig-3.3(a). The preliminary observation is that the transmittance exhibits overall 80 to 90 % of transparency. Lower RF power density deposited film shows the lower transparency about

80 to 82 % in the overall wavelength range and films deposited at higher RF power density show increased transparency about 90 %. The oscillations in the spectra are due to interference and these fringes increase with the increase in thickness. Each of the transmission spectra is simulated using envelope method formulas scripted in MATLAB program as discussed in the experimental section. The simulated 6 W/cm^2 spectra is shown in Fig-3.3(b). The estimated optical thickness from the simulations have been tabulated in Table-3.1.

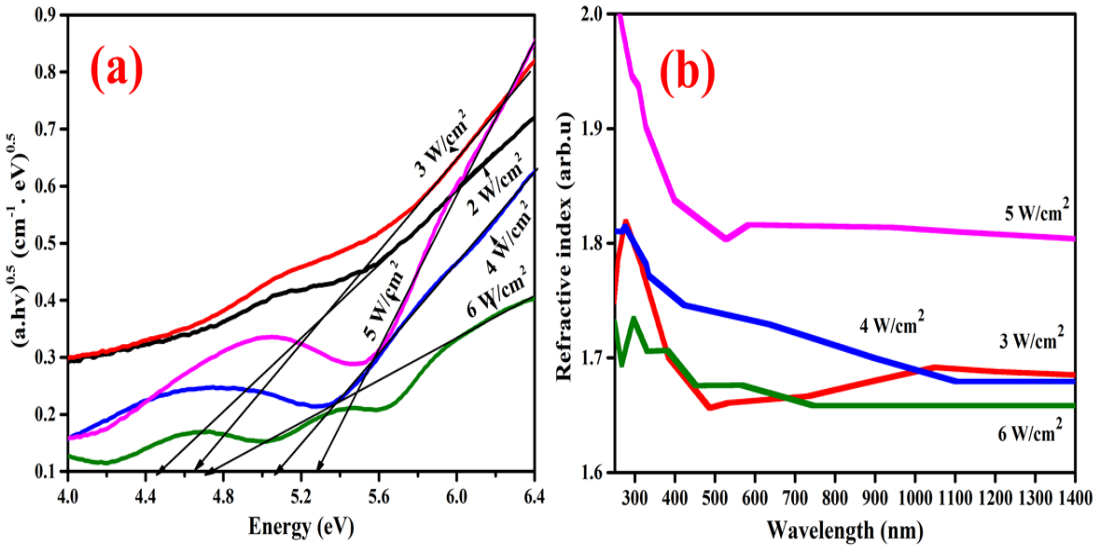

Fig-3.4: The optical properties of RF power density varied HfO_2 films: a) bandgap calculations and b) refractive index calculations.

The bandgap and Refractive Index (RI) estimated from the simulations are shown in Fig-3.4 (a-b). HfO_2 is an indirect bandgap material, hence 'n' value equal to 0.5. The plots between $(\alpha.h\nu)^{0.5}$ vs $(h\nu)$ are shown in Fig-3.4(a). The extrapolated linear portion gives the bandgap value of the HfO_2 film. The RI, n, is a graded function of the material, that depends on the incident wavelength [28, 29]. The bandgap of the HfO_2 films are estimated to be 4.4 eV, 4.5 eV, 5.1 eV, 5.3 eV, and 4.7 eV respectively for 2, 3, 4, 5, and 6 W/cm^2 power densities. The RI of the films is shown in Fig-3.4(b). On an average the RI of the films varied between 1.7 to 1.8. It is well known that the RI depends on the density of the material [30]. The loosely packed grains and density variations might cause the observed change in RI values. The variation of bandgap values and RI values with the RF power might be due to variation of film properties like defects creation, density variations in the films [31]. Here it is important to know that the nucleation and growth kinetics critically depend on the morphology and other properties of substrates. Hence the quantitative comparisons between film deposited on Si and quartz may not be appropriate. However, this study gives rough idea about the possible bandgap and other

optical properties. These values are not actually used for any other calculations in this thesis. Films deposited on Si and TEM grids are used for further studies.

FESEM images for HfO_2 films grown with varying RF power density are shown in Fig-3.5. FESEM technique is very useful to understand the surface morphology, grain size and quality of the film. With increase in RF power density, the overall grain size increases from 15 nm to 50 nm. Films deposited at 3 W/cm^2 shows uniform film distribution and having a grain size around 15-18 nm as shown in Fig-3.5(a). At 4 W/cm^2, the grain size was around 22-25 nm and smaller grain agglomeration is evident as shown in Fig-3.5 (b). Further increase of power density to 5 W/cm^2 led to flak-like grains formation, and the grain size increases further to 30 nm as shown in Fig-3.5 (c). At this stage each of the bigger grain is a combination of smaller crystallites as evident from the SEM images and grains are in irregular shape. At highest power density of 6 W/cm^2, these irregular grain growth and flake-like structures were evident as shown in Fig-3.5 (d). At this stage, the grain size was around 45-50 nm (along axis), The flake-like structure is possible at higher deposition rates and tends to localize surface free energy leading to higher nucleation rates [32]. Some reports suggest that, film structure with fibrous grains appear at high sputtering powers as the highly energized inert Ar ions can provide translational kinetic energy to the adatoms [33].

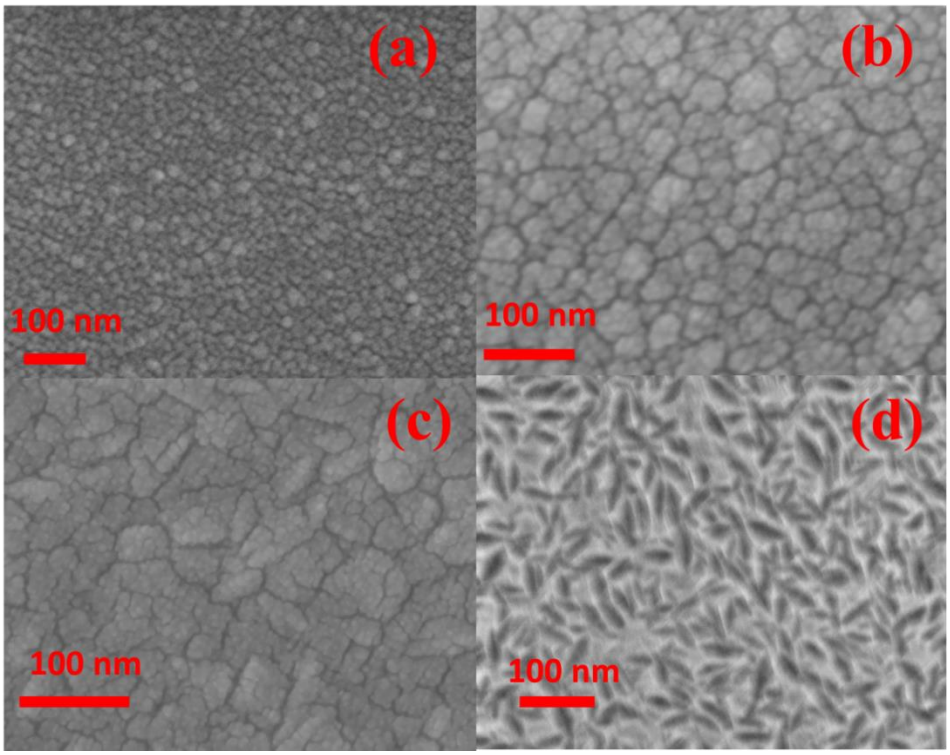

Fig-3.5: FESEM images of HfO_2 films deposited at various RF power densities: a) 3 W/cm^2, b) 4 W/cm^2, c) 5 W/cm^2, and d) 6 W/cm^2.

The PL spectra of the HfO_2 films deposited at various RF power densities are shown in Fig-3.6 (a-d). The excitation energy was 3.5 eV which is less than the bandgap of the HfO_2 (5.7 eV). Hence the observed emission can be attributed to defect induced mid-bandgap states. A preliminary observation suggests that, the intensity of the PL peak increases with deposition power density which might be due to increase of film thickness. The PL spectra are relatively broad emission from 2.4 eV to 3.8 eV. The films deposited at 2, 3, and 4 W/cm^2 show almost similar kind of spectra except a minor change in intensity. For 6 W/cm^2 RF power density, emission spectrum shows peaks at 2.9 eV and 3.3 eV. After deconvolution using peak fitting program, each of the broad peak yielded new peaks at 2.4, 2.5, 2.9, 3.4 and 3.5 eV. Previous reports suggest that the observed PL is due to shallow and deep level oxygen related defect states or F-centers [33, 34].

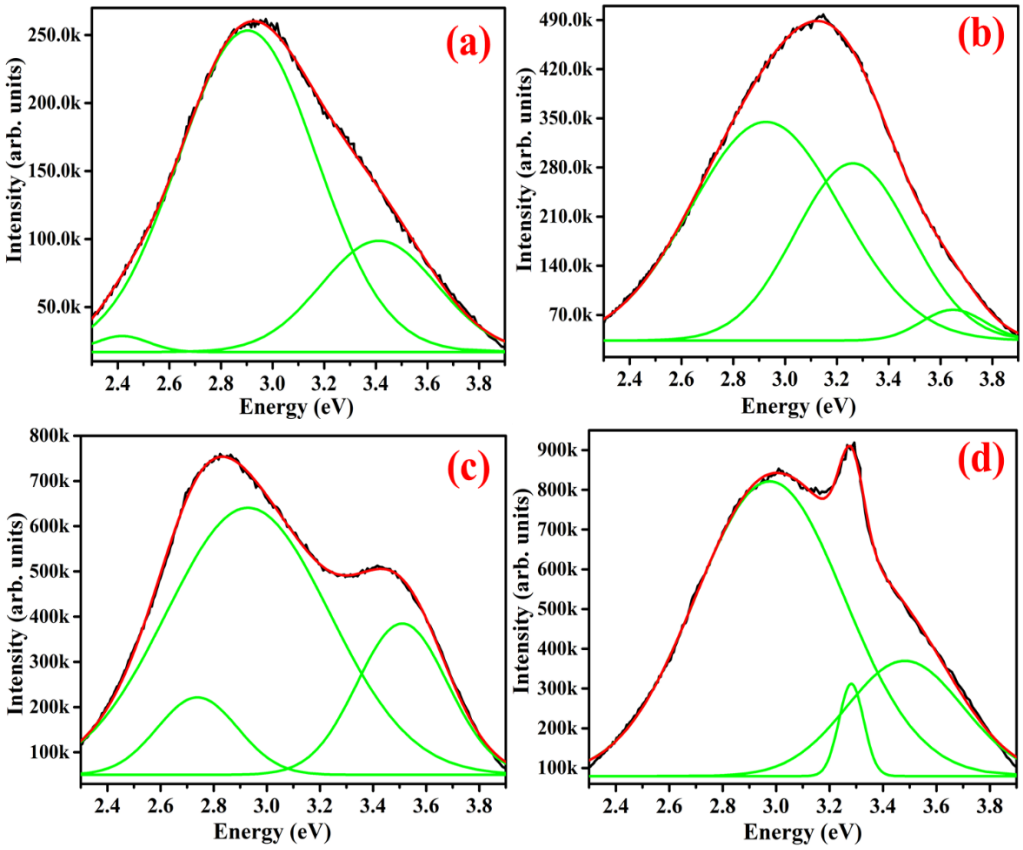

Fig-3.6: The Photoluminescence spectra HfO_2 films deposited at various RF power densities: a) 3 W/cm^2, b) 4 W/cm^2, c) 5 W/cm^2, and d) 6 W/cm^2.

3.3.2. Dependence on deposition pressure:

In this section, we have deposited the HfO_2 films on Si and Quartz substrates by varying the deposition pressure. During these depositions, the sputtering power was maintained at 60 W which is optimized from the above conditions. The deposition pressure was varied from 10 to

40 mtorr individually for each deposition. Each of the deposition was carried out for 90 minutes at room temperature. The estimated and calculated film thickness from various measurements have been tabulated in Table-3.2. The quality of the film, grain size, porosity, thickness and optical properties of the films strongly depend on the stoichiometry of the films which indirectly depend on the deposition pressure [35, 36]. According to preliminary investigations, the deposition rate is highest for 10 mtorr which is 0.9 which decreases drastically with increase of deposition pressure. This could be due to an increase of collision frequency between the sputtered species and Ar ions. This decrease of deposition rate with the increase of deposition pressure is due to the decrease in the mean free path of sputter species [37].

Table-2: Thickness of the HfO_2 film deposited at different Ar pressure.

Deposition Pressure (mtorr)	**Profilometer Thickness (nm)**	**RBS (nm)**	**Growth Rate (nm/min)**
10	89	85	0.9
20	61	--	0.7
30	46	43	0.6
40	27	21	0.3

The RBS spectra of thin films for varying deposition pressure and their simulations are shown in Fig-3.7. The intense peak at 1800 channel number belongs to the 'Hf' peak and small hump at channel number 620 belongs to the 'O' peak. The intensity of the Hf peak decrease with increase of the deposition pressure was noticed. The stoichiometry of Hf varies from 27% to 29% with the variation of deposition pressure, which are more are less equal within the experimental limits. The calculated areal densities are 721, 361 and 175×10^{15} atoms/cm^2 for the deposition pressures of 10, 30 and 40 mtorr respectively. The physical thickness of the films is calculated by dividing it with the areal density of bulk HfO_2 which is 8.4 atoms/cm^3. The calculated physical thickness from the areal densities have been tabulated in Table-3.2.

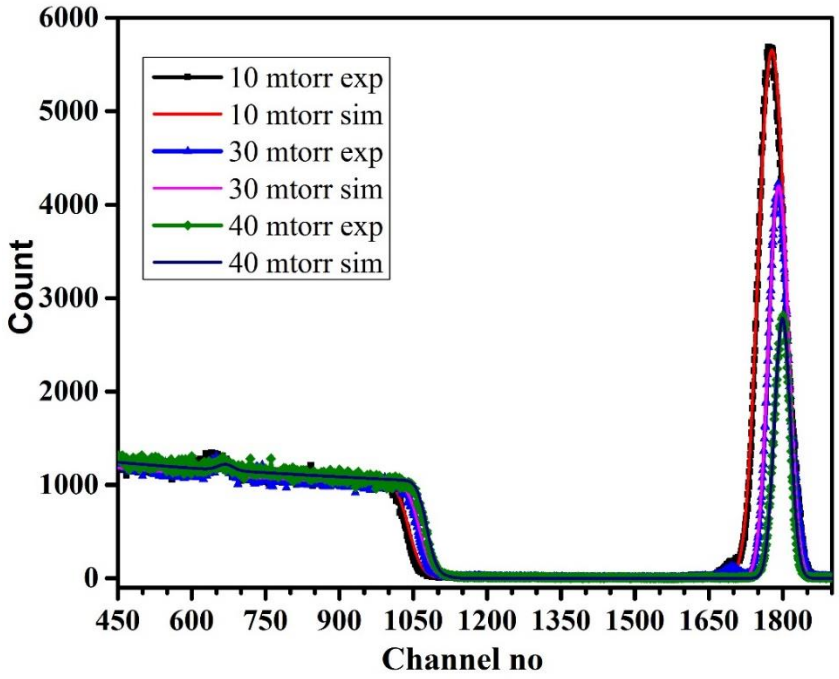

Fig-3.7: The RBS spectra and their simulation spectra of the deposition pressure varied HfO_2 thin films (exp stands for experimental curve and sim stands for simulated curve).

The surface morphology of the films is studied by FESEM images shown in Fig-3.8 (a-d). At lowest deposition pressure of 10 mtorr, the average grain size was around 16 nm as shown in Fig-3.8(a). At this pressure morphology of the film shows closely packed continuous grain structure and uniformity in the film. Further increase of the deposition pressure to 20 mtorr, leads to uniform and smaller grains (around 14 nm). In this case, the grain to grain separation increases when compared to 10 mtorr sample. Whereas in the case of 30 mtorr, the grain size dicreases further to around 10 nm and grain to grain saparation is large. At highest deposition pressure of 40 mtorr, the voids between the grains increases further and grain size was same as above. Collision between the sputter species and Ar ions reduces the sputter species mobility and deposition rate [38]. While grain formation is in progress, if the diffusion length is larger than the grain size, adatoms diffuse through the grains and form continuous and void free films which is found to be inversely proportional to the deposition pressure [39]. This might be due to the decrease of adatoms diffusion length, which is also inversely propotional to the Ar pressure [40, 41].

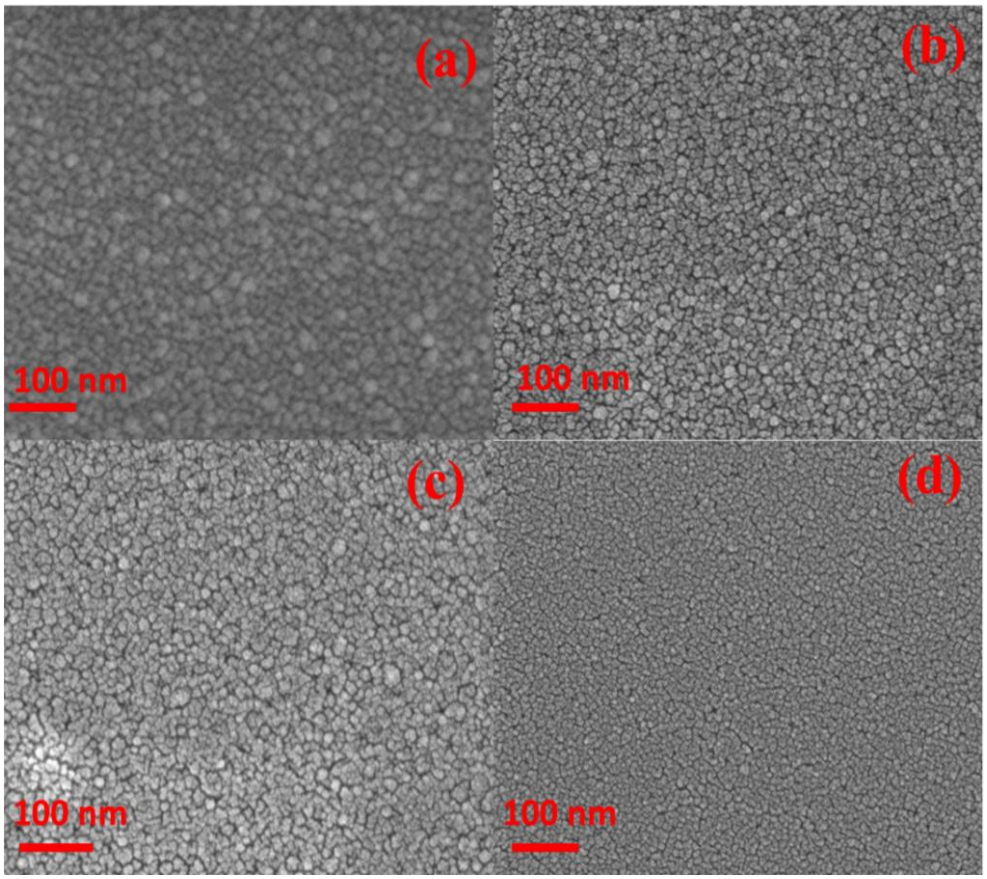

Fig-3.8: FESEM images of HfO_2 films deposited at various deposition pressure: a) 10 mtorr, b) 20 mtorr, c) 30 mtorr, and d) 40 mtorr respectively.

UV-Vis-NIR spectroscopy was performed on HfO_2 films deposited on quartz substrates to investigate the optical properties. The transmission spectra is shown in Fig-3.9(a) and simulation of transmittance spectra for 10 mtorr is shown in Fig-3.9(b). The bandgap of the HfO_2 films is extracted from the well-known Tauc's relation as discussed in the experimental section. The extracted bandgap of the HfO_2 films for varying pressures is shown in Fig-3.10. The bandgap of the films varies between 5.3 eV to 4.9 eV. This variation might be due to the change in porosity in the films. The increase in voids and variation in film density affects the bandgap as well as RI of the films. Once again it is important to note that the films deposited on quartz are used for qualitative information for optimization only. These samples are not used for further studies in this thesis.

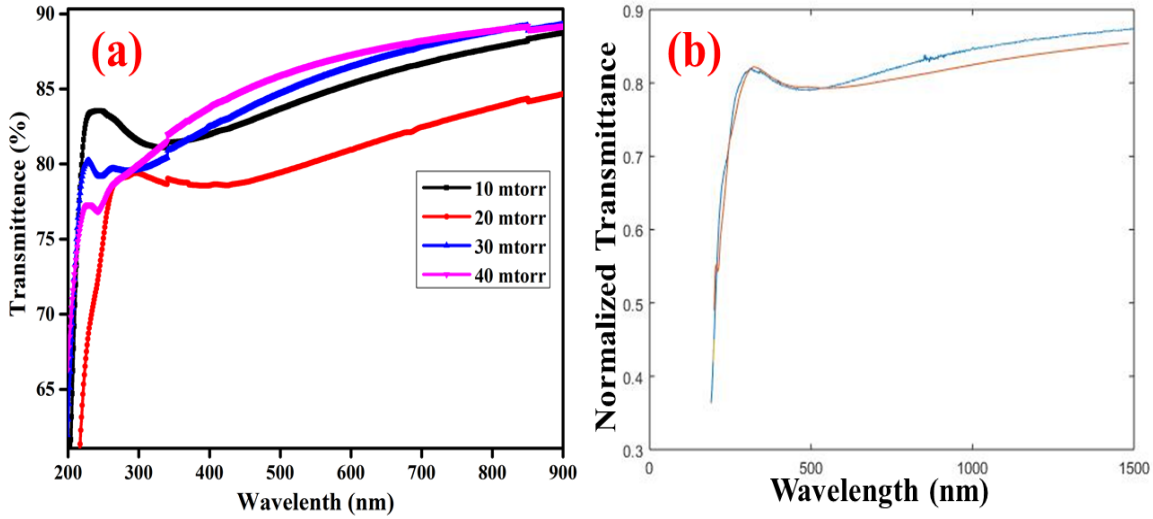

Fig-3.9: The optical properties of Ar pressure varied HfO_2 films: a) transmittance spectra, b) fitting of transmittance spectra for 10 mtorr.

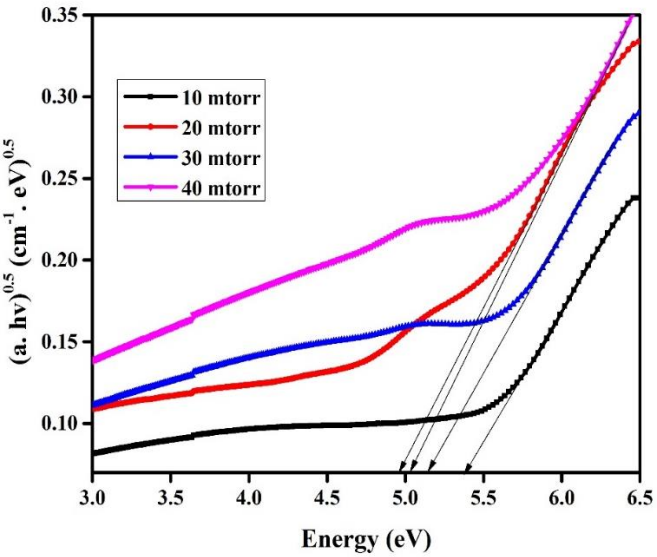

Fig-3.10: The optical bandgap spectra of pressured varied HfO_2 thin films.

3.3.1. Oxidization of the HfO_2 films

From the above-optimized deposition conditions of RF magnetron sputtering system, the HfO_2 films were deposited at 60 W RF power (3 W/cm^2) and 10 mtorr deposition pressure. The deposition was carried out for 90 minutes. These films were deposited on both Si and quartz substrates to investigate the structural and optical properties. The estimated thickness of the deposited film for similar deposition parameters employed previously was around 100 nm. The thickness of the deposited films was cross-checked by using the profilometer and cross sectional-FESEM measurements, which agree with the estimated one (nominal value).

HfO_2 films on Si and quartz substrates were annealed from 100 ºC to 600 ºC with an interval of 100 ºC for 1 hour in O_2 atmosphere. These films were annealed in the furnace shown in Fig-3.11. As-deposited films are non-stoichiometric with suboxide films at the interface. After annealing, the "O" atoms diffuse into the film and fill the oxygen defected states.

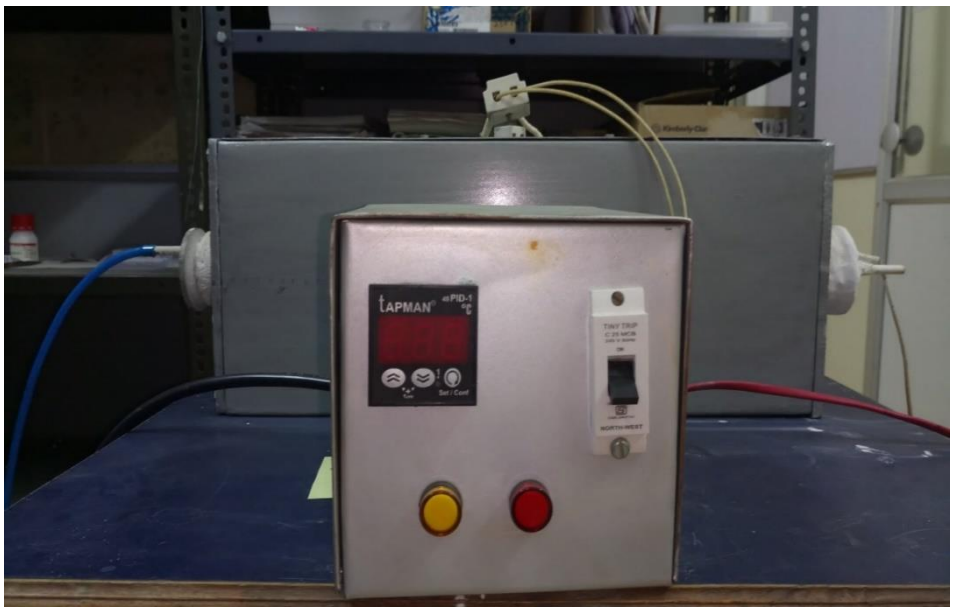

Fig-3.11: Furnace used for annealing of the films.

GIXRD spectra of annealed HfO_2 films is shown in Fig-3.12. Pristine and annealed up to 300 ºC films show amorphous nature. Nucleation of crystallization can be seen for the films annealed at 400 ºC. Subsequent annealing (500 ºC and 600 ºC) clearly shows grain growth. The diffraction pattern matches with the standard JCPDS file [PDF# 06-0318] having monoclinic phase of $P2_1/c$ space group. The peaks at 2θ=24.4º, 28.5º, 31.71º and 34.7º belong to the diffraction planes (011), (-111), (111) and (020) respectively. The intensity of the (-111) diffraction peak increases with the increase in annealing temperature. When the films got transformed from amorphous to crystalline, the plane (-111) exhibit lowest surface free energy. With increasing temperature, the dominant peak (-111) shifts slightly to lower angles. This indicates the strain relaxation and lattice expansion in the films due to annealing. The decrease of FWHM indicates the increase in grain size. The average grain size slightly increases from 18 to 21 nm, when annealing temperature increases from 500 to 600 ºC.

The FE-SEM images of the annealed HfO_2 films at different oxidization temperatures are shown in Fig-3.13. In general, films deposited at room temperature exhibit the amorphous nature. The surface morphology of annealed films show a uniform distribution of spherical grains and these results are consistent with those presented in previous sections. With the

increase of annealing temperature from 100 ºC to 600 ºC, the film quality improves. It is evident that the grain size increases with increase in annealing temperature. Initially, grain size was around 16 nm in as-grown films and with further increase of temperature, the grain size increases to 21 nm. This could be due to the diffusion of surrounding HfO_2 molecules into one another resulting in the increase of grain size.

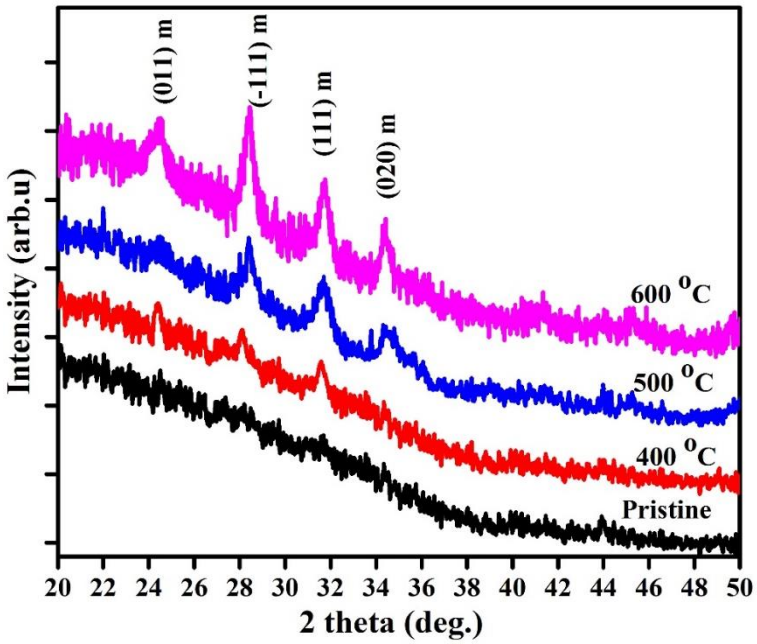

Fig-3.12: GIXRD spectra of annealed HfO_2 thin films.

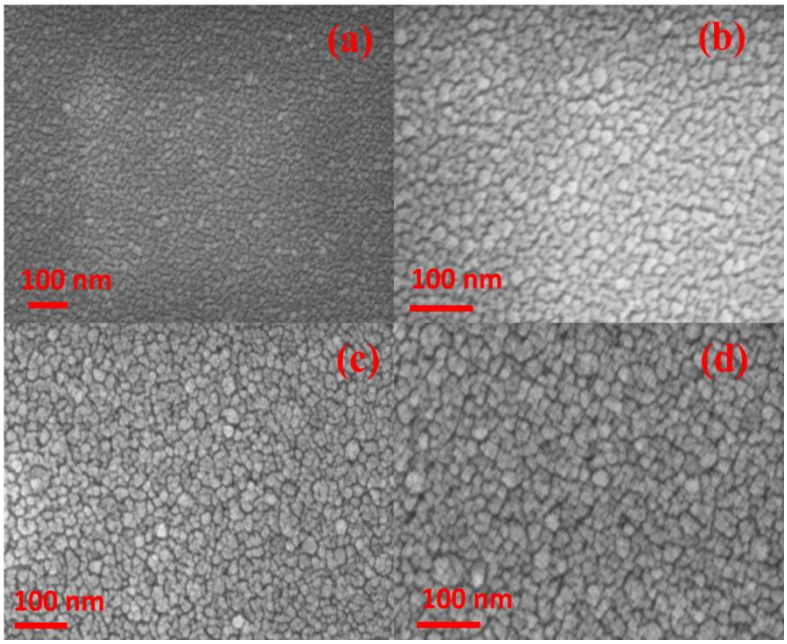

Fig-3.13: The FESEM images of annealed films a) pristine, b) 400 ºC, c) 500 ºC, and d) 600 ºC.

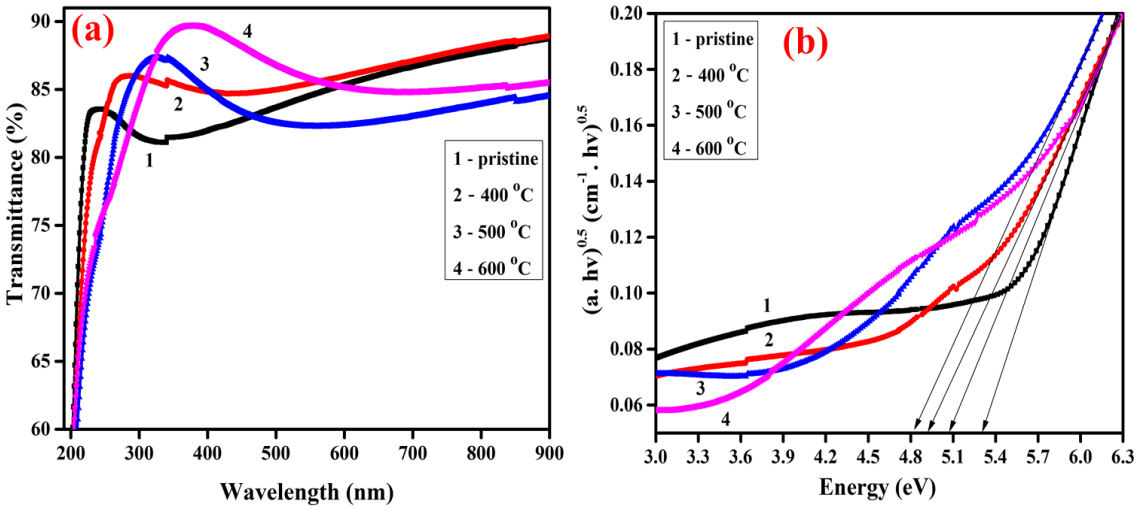

Fig-3.14: a) the transmission spectra of annealed HfO_2 films and b) bandgap calculations from the transmission spectra of various annealed films.

The transmittance spectra and bandgap calculations of the annealed HfO_2 deposited on quartz are shown in Fig-3.14. With increase in the annealing temperature, the transmittance of the films increases from 84 to 88%. The plotted bandgap of the annealed films was calculated using Taulc's relation equation 3.5 [20]. The pristine film shows the bandgap of 5.3 eV and it agrees with the amorphous HfO_2 film, which exhibits highest bandgap 5.7 eV. After annealing, the bandgap of the films slightly decreases from 5.3 eV to 5.0 eV for 400 ºC and 500 ºC, but for films annealed at 600 ºC shows 5.2 eV. The continuous amorphous grain network turning to polycrystals causes the initial observed bandgap reduction, but further annealing improves the monoclinic structure which causes subsequent bandgap increase. However, compared to amorphous films bandgap value, the monoclinic bandgap is less. This is because naturally amorphous films are of highest band gap values.

3.4 Conclusions

In summary, HfO_2 films were prepared by RF magnetron sputtering method at various deposition conditions like deposition power, pressure and of different annealing temperatures. All the samples were characterized and investigated by several techniques. The thickness of the films increases linearly with RF power. Films deposited at low RF power show regular grain growth and films deposited at high RF power show irregular grain growth. From these observations, moderate RF powers like 60, and 80 W are suitable for practical applications. The HfO_2 film thickness decreases with increase in deposition pressure. The grain size decreases and porosity of the film increases with the increase in the deposition pressure. From the above conditions, 10 mtorr deposition pressure and 60 W of RF is found to be suitable for

growing good HfO_2 films. Annealed HfO_2 films show amorphous phase at room temperature and 400 ºC, and further annealing leads to the monoclinic phase transformation. In the monoclinic phase stabilized films, the transition grain growth and improved film quality were observed. HfO_2 films deposited at room temperature on Si and TEM grids were used for further studies in this thesis.

3.4 References

1. G. Korotchenkov, "Thin metal films". *Handbook of Gas Sensor Materials*. Integrated Analytical Systems. Springer. pp. 153–166 (2013).
2. M. Birkholz; K.-E. Ehwald; D. Wolansky; I. Costina; C. Baristyran-Kaynak; M. Fröhlich; H. Beyer; A. Kapp; F. Lisdat *Surf. Coat. Technol*. **204**, 2055–2059 (2010).
3. van der Kooi, C.J.; Elzenga, J.T.M.; Dijksterhuis, J.; Stavenga, D.G, *Journal of the Royal Society Interface*. **14**, 0933 (2016).
4. MacLeod, H. Angus (2010). Thin-Film Optical Filters (4th ed.). Taylor Francis. ISBN 978-1-4200-7302-7.
5. Sturgeon, W, Trans. Royal Society of Arts, Manufactures, & Commerce. London. *cited in* Miller, T.J.E **43,** 37–52. (2001).
6. Puurunen, Riikka L, *J. Appl. Phys.* **97**, 121301 (2005).
7. Tavares, Janson Swanson, E.J Coulombe, *Plasma Processes and Polymers*. **5**, 759 (2008).
8. Klein, L.C. and Garvey, G.J, Journal of Non-Crystalline Solids, **38**, 45 (1980).
9. Rahaman, M.N, and Boca Raton, *Ceramic Processing*, *CRC Press.* **15**, 242–244, (2007).
10. Hanaor, DAH; Triani, *Surface and coatings technology*. **205**, 3658–3664 (2011).
11. Selvakumar, N.; Barshilia, Harish C, *Solar Energy Materials and Solar Cells*. **98**, 1–23 (2012).
12. Fortunato, E.; Barquinha, P.; Martins, R *Advanced Materials*. **24**, 2945–2986 (2012).
13. K. Ishii, *Journal of Vacuum Science and Technology A*. **7**, 256–258 (1989).
14. He, Zhenping; Kretzschmar, Ilona, *Langmuir*. **28**, 9915–9919 (2012).
15. I. Adesida, A. Mahajan, E. Andideh, M. Asif Khan, D. T. Olsen, *and* J. N. Kuznia, *Appl. Phys. Lett.* **63**, 2777 (1993).
16. Subodh K. Gautam, Abdelhak Chettah, R.G. Singh, Sunil Ojha, Fouran Singh, *Nucl. Instr. Meth. Phys. Res. B* **379,** 224–229 (2016).

17. J. Larkin, R. Henley, D. C. Bell, T. Cohen-Karni, J. K. Rosenstein, and M. Wanunu, *ACS Nano* **7,** 10121 **(**2013).
18. E. P. Simonenko, D. V. Sevast'yanov, N. P. Simonenko, V. G. Sevast'yanov and N. T. Kuznetsov, *Russ. J. Inorg. Chem.* **58,** 1669–93 (2013).
19. M. Lee, N. Zine, A. Baraket, M. Zabala, F. Campabadal, R. Caruso, M. G. Trivella, N. J. Renaulta, and A. Errachid, *Sens. Actuator B-Chem.* **175**, 201-207 (2012).
20. M. Mayer, SIMNRA: Simulation of RBS, ERD and NRA Spectra. <http://www.rzg. mpg.de/mam/>.
21. P. Scherrer, *Göttinger Nachrichten Gesell.*, **2**, 98 (1918).
22. R Swanepoel, *J. Phps. E: Sci. Instrum.* **16**, (1983).
23. J. Tauc, R. Grigorovici, and A. Vancu, *Phys. Status Solidi* **15**, 627 (1966).
24. Yi-Lung Cheng and Tian-Cih Bo, *Surface and Coatings Technology* **260,** 198–204 (2014).
25. B. Deng, G. He, J.G. Lv, X.F. Chen, J.W. Zhang, M. Zhang, and Z.Q. Sun, *Optical Materials* **37**, 245–250 (2014).
26. Xinyi Dai, Aijun Zhou, Lidong Feng, Ying Wang, Jin Xu, Jingze Li, *Thin Solid Films* **567**, 64–71 (2014).
27. Chen, L., Graham, M. E., Li, G., Ray, K. A, *Thin solid films* **515**, 1176 (2006).
28. Martin Jerman, Zhaohui Qiao, and Dieter Mergel, *Appl. Opt.* **44**, 15-20 (2005).
29. K. S. Wanjala, W. K. Njoroge, N. E. Makori, J. M. Ngaruiya, *A. J. Cond. Matt. Phys.* **6,** 1-6 (2016).
30. Michal Mazur, Danuta Kaczmarek, Jaroslaw Domaradzki, Damian Wojcieszak and Agata Poniedzialek, *Coatings* **6**, 13 (2016).
31. N. Manikanthababu, M. Dhanunjaya, S.V.S. Nageswara Rao, A.P. Pathak, *Nucl. Instr. Meth. Phys. Res. B*, **379**, 230–234 (2016).
32. M Dhanunjaya, S A Khan, A P Pathak, D K Avasthi and S V S Nageswara Rao, *J. Phys. D: Appl. Phys.* **50**, 505301 (2017).
33. T.V. Perevalov, V.Sh. Aliev, V. A. Gritsenko, A. A. Saraev, V.V. Kaichev, *Micr. Eng.* **109,** 21–23 (2013).
34. D. R. Islamov, V. A. Gritsenko, T. V. Perevalov, *ECS Trans.* **69**, 197-203, (2015).
35. Vladimir A. Gritsenko 1, Timofey V. Perevalov 1, Damir R. Islamov, *Phys. Rep.* **613,** 1–20 (2016).
36. Tingting Tan, Zhengtang Liu, Hongcheng Lu, Wenting Liu, Hao Tian, *Optical Materials,* **32**, 432–435 (2010).

37. Shen Yan-Ming, et.al, Chen. *Phys. Lett.* **24**, 2963 (2007).
38. T. Minami, S. Ida and T. Miyata, *Thin solid films*, **93**, 416 (2002).
39. T. K. Subramanyam, B. Srinivasulu naidu and S. Uthanna, cryst. *Res. Technol.* **35**, 1195 (2000).
40. V. Assuncao, E. F Ortunato, A. Marque, H. Aguas, I. Ferreira, M. E. V. Costa and R. Martins, *thin solid films* 427 (2003) 402.
41. J. L. Andujar, F. J. Pino, m. C. Polo, A. Pinyol, C. Corbella and E. Bertran, *diam. Related mater.* 11, 1008 (2002).
42. R Swanepoel, J. Phps. E: *Sci. Instrum*. **16**, (1983).

SHI Induced Crystallization and Phase Transformation in HfO_2 Thin-films Deposited by RF Magnetron Sputtering

This chapter presents a study on Swift Heavy Ion (SHI) irradiation induced crystallization and grain growth of HfO_2 nanoparticles within the HfO_2 thin-films deposited by Radio Frequency magnetron sputtering method. Various characterization techniques have been employed to study ion irradiation induced structural modifications to the films. As grown films consisted of amorphous clusters of non-spherical HfO_2 NPs. After irradiation these nano-clusters were transformed to crystalline grains. These crystallites are found to be spherical in shape and are well dispersed within the films. The average size of these crystallites is found to increase with fluence. The photo luminescence data indicated the presence of oxygen related defects in pristine and irradiated samples and rearrangement of defects after irradiation. The SHI irradiation induced crystallization and grain growth are explained within the framework of thermal spike model.

4.1 Introduction

As discussed in the previous chapters, the replacement of SiO_2 by HfO_2 as gate dielectric in modern integrated circuit technology has stimulated significant interest in HfO_2 [1-3]. Many properties of HfO_2, including its stability on Si surface need thorough investigation [4, 5]. Further, it is important to study the sensitivity of this material to ion and other forms of irradiation. This information is critical for employing HfO_2 based electronic devices in space and other radiation harsh environments. Ion beams can be used to simulate radiation environment in laboratory at shorter time intervals in controlled manner [6, 7]. These experiments will also enable us to elucidate the basic physics governing ion-solid interactions as well as to tune material properties with spatial selectivity. The main objective of the experiments presented in this chapter is to investigate the effects of huge electronic excitations produced by swift heavy ions (SHI) in thin HfO_2 films on their structural properties. It is shown that the initial state of material plays a critical role in determining the effects of SHI irradiation [8].

Hafnium oxide finds several applications in various fields owing to its superior thermal, optical and electrical properties. High temperature sustainable and corrosion resistant materials like HfO_2, HfB_2 and HfN are essential for the development of advanced technologies required for hypersonic vehicles, hydrodynamic propellers and space shuttles etc. [9-11]. In recent years, with rapidly evolving complimentary MOS (CMOS) technology, there has been a detailed search for good alternate high dielectric constant (high-k) materials. HfO_2 has been identified as an appropriate gate dielectric to meet the demands required to uphold the Moore's law. Hence a great deal of attention has been devoted to HfO_2, in view of its high dielectric constant (~ 25), acceptable band-offsets with Si and reasonably good thermal stability on the surface of Si [12].

Moreover, the downscaling of HfO_2 films to nano-dimensions would further extend its applicability to nano-electronics, optoelectronic devices and sensors [13]. It is also important to note that HfO_2 is a bio-compatible material and finds many applications in bio-sensors. It was shown that the Si nanowires coupled with HfO_2 are highly sensitive to detect small nucleic acid oligomers [14]. Ultrathin self-standing membranes of porous HfO_2 have been employed to detect single and double stretched DNAs. Owing to the bio-inertness of HfO_2, the nanoparticles (NPs) of HfO_2 have been used as active materials for fabricating several

biosensors [15]. HfO_2 NPs based cancer therapy employs crystalline HfO_2 NPs to improve the targeted radiation dose within tumor tissues without much damage to healthy tissues [16].

As mentioned above, the main objective of the studies presented in this chapter is to investigate the growth and SHI irradiation induced modifications of thin-films consisting of HfO_2 nanoparticles. There are several reports on the fabrication of HfO_2 nanoparticles: Oil/Water interface approach [17], Microwave hydrothermal technique [18, 19], chemical synthesis methods [20] (including precipitation and sol-gel methods [21-22]) and ultra-fast Laser ablation [23] have been widely employed to fabricate nanoparticles and nanostructures of HfO_2. Here we prepare thin-films of HfO_2 by using Radio Frequency (RF) magnetron sputtering method in Ar atmosphere. The formation of NPs is expected to critically depend on growth parameters like RF power, Ar - pressure, target to substrate distance and post-growth treatments like thermal annealing and ion irradiation. Collisions between thermalized Hf and O atoms can lead to the formation of molecular phases in the process chamber during deposition. This process governs the formation of molecular phases and their transport through diffusion [24]. Toledano-Luque et. al. [25] and Znamenski *et al.* [26] reported similar dependency in NPs formation of other materials using RF magnetron sputtering technique. Our previous investigations suggested enhanced inter-diffusion of constituent elements across Hf/SiO_2 and Hf/Si interfaces under SHI irradiation [27-29].

In the present study, we investigate SHI irradiation induced crystallization and grain growth in HfO_2 thin-films as a function of ion fluence. The observed phase changes during SHI irradiation provide valuable information for the reliability and tunability of HfO_2 based Phase Change Resistive Random-Access Memory (PCRRAM) devices [30-32]. Further, the study is also focused at some important fundamental aspects of SHI irradiation induced modification of nano-particles in general and nano-particles of technologically important hafnium based high-k dielectric materials in particular. There are few reports in the literature on SHI-irradiation induced ordering and improvement in crystallinity of several nanostructures, some polymers and thin- films under [33-37]. However, to the best of our knowledge, there are no reports on the effects of SHI irradiation on HfO_2 thin films prepared by RF Magnetron sputtering method.

4.2 Experimental details

4.2.1 Sample preparation:

Hafnium Oxide thin films were deposited by using RF Magnetron sputtering method. These depositions have been carriedout by using a commercially available 2-inch diameter, 3 mm thick and 99.99 % pure HfO_2 sputter target. The films were grown on Boron doped p-type Si (100) wafers of 1 -10 Ω-cm resistivity and 200 mesh Carbon coated Copper TEM grids. The Si substrates were cleaned ultrasonically in acetone, isopropyl alcohol and DI water. TEM grids were placed on pre-cleaned glass slides. The edges of the TEM grids were covered with glass cover slips which were stuck on a glass slide using carbon tape without touching the TEM grids. The TEM grid containing glass slides and Si substrates were clamped to the substrate holder directly before loading them in the sputtering chamber as shown in schematic diagram of Fig-4.1. A standard RF frequency of 13.56 MHz was used in this deposition work. Initially, the sputtering chamber was evacuated to a base pressure of 8×10^{-6} mbar. Then Ar gas of purity 99.99 % was introduced into the chamber using a Mass Flow Controller (MFC). The depositions were carried out at a pressure of 2.4×10^{-3} mbar. The target to substrate distance and deposition power were maintained at 12.5 cm and 60 W respectively. While depositing the films, the substrate holder was set to rotation at a speed of 10 rpm for uniformity, and the depositions were carriedout for 10 minutes. The average thickness of deposited films was estimated to be around 10-15 nm by employing Ambios XP 200 Profilometer.

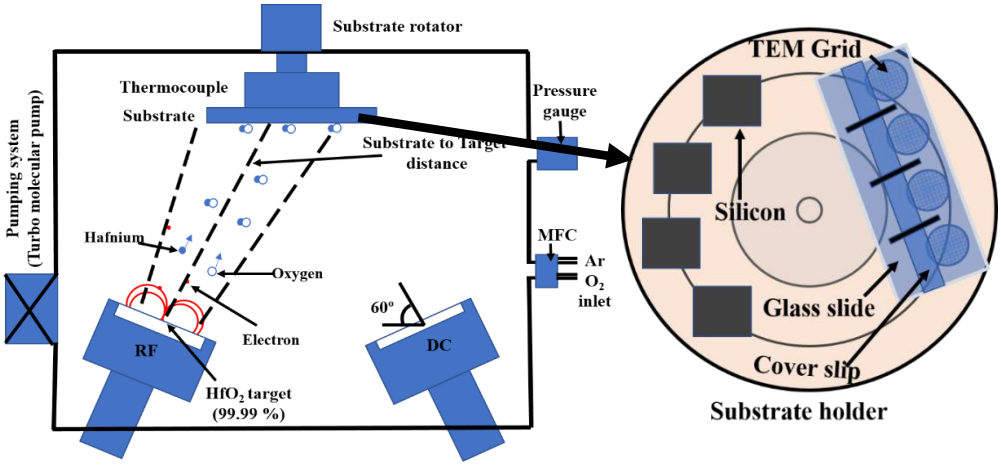

Fig-4.1: Block diagram showing i) the target and substrate configuration within the sputtering chamber (on left side) and ii) substrate holder with a map of loaded substrates (on right-side).

4.2.2 Swift Heavy Ion Irradiation Details

HfO_2 thin-films grown on both Si substrates and TEM grids have been irradiated by 100 MeV Ag ions to different fluences using a 15 MV Tandom Pelletron accelerator at IUAC, New Delhi. Glass slides containing the TEM grids were loaded as such in the irradiation chamber without disturbing the TEM grids. Silver paste was used to electrically connect both TEM grids and Si substrates to target ladder for measuring beam current. This connection is also essential to remove excess charges produced during irradiation. The ion range (R), electronic energy loss (S_e) and nuclear energy loss (S_n) of incident 100 MeV Ag ions in HfO_2 were estimated to be 7.74 µm, 23.2 keV/nm and 0.15 keV/nm respectively. A standard and well-known simulation software: Stopping and Range of Ions in Matter (SRIM-2013) [38] has been employed to estimate above parameters. The ion beam was scanned over 1 cm x 1 cm of the sample area at a constant beam current of 1 particle nano-Ampere (pnA). Low beam current helps avoiding beam heating effects and constant current ensures uniform irradiation over the sample surface. Hence, the irradiation fluence is directly proportional to the scanning time and the relation between the fluence and time is given by Eq-4.1. The two sets of samples were irradiated at three different fluences by varying the irradiation time and the details are given in Table-4.1. The schematics of irradiation is shown in Fig4.2. The irradiation area and beam current were constant, so the irradiation fluence was directly proportional to scanning time of irradiation.

$$time\ (sec) = \frac{Fluence \times Area}{6.25\times10^{12} \times Ion\ current\ (pnA)} \tag{4.1}$$

where time is in seconds, fluence is in ions/cm^2 and current is in Nano Amperes (nA) or particle Nano Amperes (pnA). The pre-calculated time was used to irradiate the films with different fluence. Fig-4.3 shows the depth dependence of Electronic energy loss (S_e) and Nuclear energy

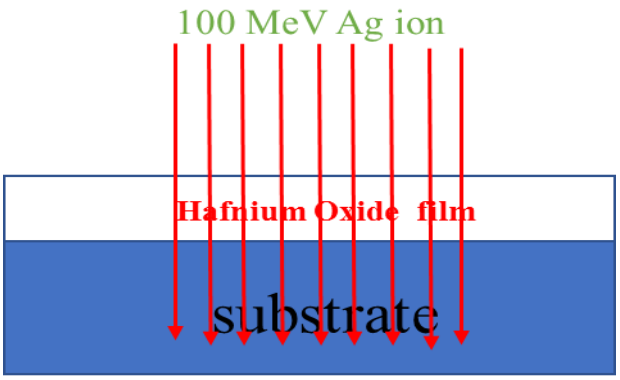

Fig-4.2: The schematics of the ion irradiation of HfO_2 films.

Table 4.1: Sample details, ion energy, irradiation and SRIM Calculation details**.**

Sample Type	**Irradiation Fluence (ions/cm^2)**	**Ion Energy (MeV)**	**Average stopping power (within the HfO_2 film (~20 nm))**	
Set-A (~10-15 nm)			**Electronic (S_e) (keV/nm)**	**Nuclear (S_n) (keV/nm)**
HfO_2/Si-1	Pristine	Ag^{7+} 100 MeV	23.2	0.15
HfO_2/Si-2	3 x 10^{12}			
HfO_2/Si-3	1 x 10^{13}			
HfO_2/Si-4	3 x 10^{13}			

loss (S_n), as estimated by SRIM, in HfO_2. S_e is very much large compare to S_n within the film (shown in Fig-4.3 by shaded region). Hence the effects of electronic excitations induced by SHI irradiation are more significant when compared to the nuclear displacements due to elastic collisions. It is also important to note that the S_e is more or less uniform with in the region of interest (thin-films). Hence the value of S_e obtained at surface can be used in the analysis.

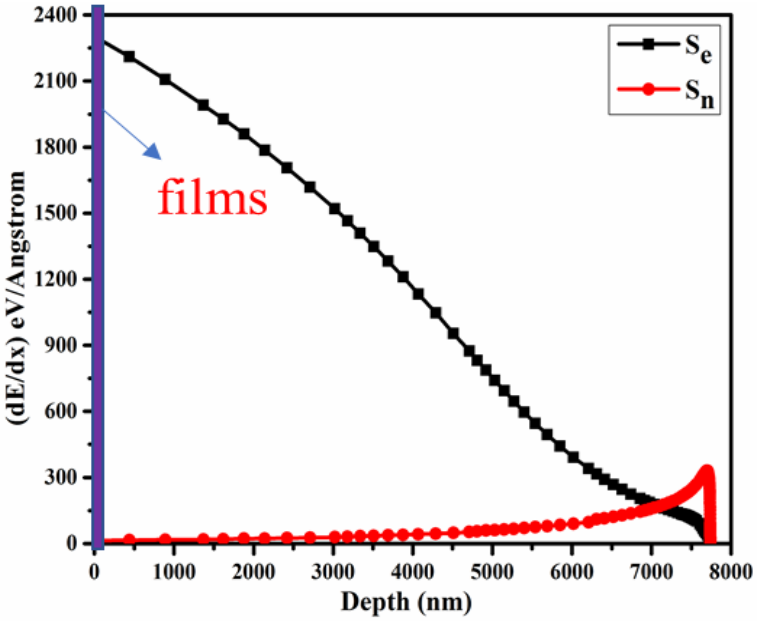

Fig-4.3: The depth dependence of electronic and nuclear energy loss of 100 MeV Ag in HfO_2 as estimated by SRIM (Shaded area shows the region of interest, i.e the thickness of thin-film under study).

The films deposited on TEM grids were investigated by High Resolution Transmission Electron Microscopy (HRTEM) and Selected Area Electron Diffraction (SAED) using a TEM – FEI Tecnai, equipped with a thermo-ionic electron gun working at 200 kV. The pristine and irradiated samples were characterized by Grazing Incident X-Ray Diffraction (GIXRD) measurements using Bruker D8 Advance diffractometer with Cu K_α source ($\lambda = 0.154$ nm) at an incident angle of 4°. Photo Luminescence (PL) measurements were performed using Fluorolog, Xenon lamp, 450 W, having resolution: 0.3 nm. Field Emission Scanning Electron Microscope measurement performed using FE-SEM: Carl ZEISS, FEG, ultra-55 instrument.

4.3 Results and discussions

4.3.1 Synthesis and characterization of as deposited samples

This section describes the preparation and characterization of samples that are used in this study. The grain size, shape, composition and crystal structure of the samples have been investigated by employing structural characterization techniques like FESEM, TEM, SAED and GIXRD. Fig-4.4(a) shows the TEM micrograph of pristine HfO_2 films that are deposited on TEM grids. It is evident from this image that the films are made of nano-size grains with poorly defined boundaries. The average grain size is estimated to be about 20 nm. The surface of the HfO_2 films deposited in Si substrates (in same run) is examined by the FESEM analysis.

FESEM image show in Fig-4.4(b) also confirms the formation of grains of size about 20 nm. Nano-cluster formation is observed on both TEM grinds and Si substrates, although the nucleation and growth kinetics are expected to be different on different surfaces. Only qualitative analysis is presented as far as the comparison between films deposited on different substrates is concerned. Further magnification revealed the fact that each grain is again an agglomeration of nano clusters of size about 2-3 nm. We focus our attention on these nano grains. The clusters are fund to be amorphous in nature and are of non-spherical in shape as shown in HRTEM image presented in Fig-4.5(a). The size distribution can be analyzed by the histogram shown in Fig-4.5(b). As mentioned above the average size is estimated to be about 2.6 nm. The same pristine HfO_2 thin-films deposited on Si substrates, were characterized by GIXRD measurements. The diffraction pattern shown in Fig-4.5(c) confirms that the as grown HfO_2 films are amorphous and these results are consistent with the TEM results. The PL measurements were performed on HfO_2 films deposited on Si substrates and the luminescence spectra are shown in Fig-4.5(d).

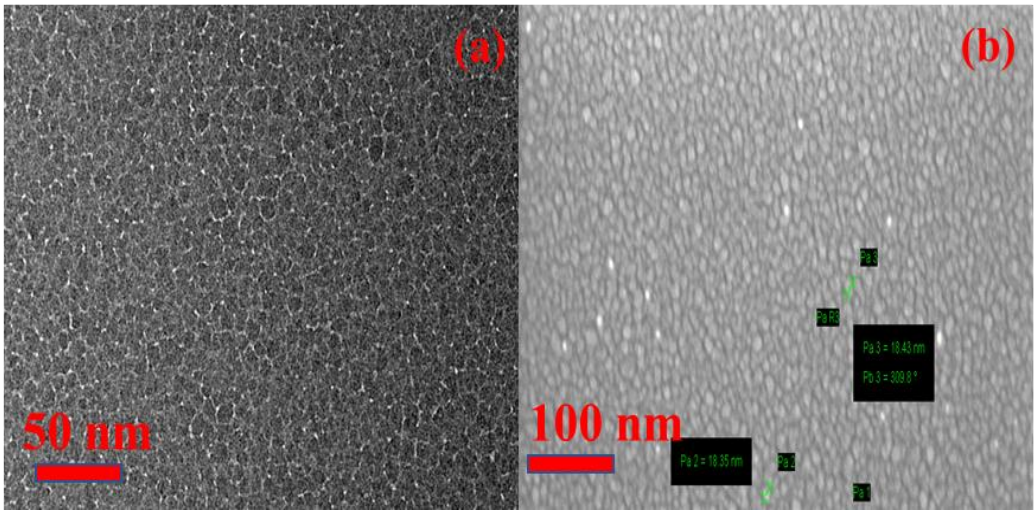

Fig-4.4: a) TEM image on TEM grids and b) FE-SEM image on Si substrate of HfO_2 thin films.

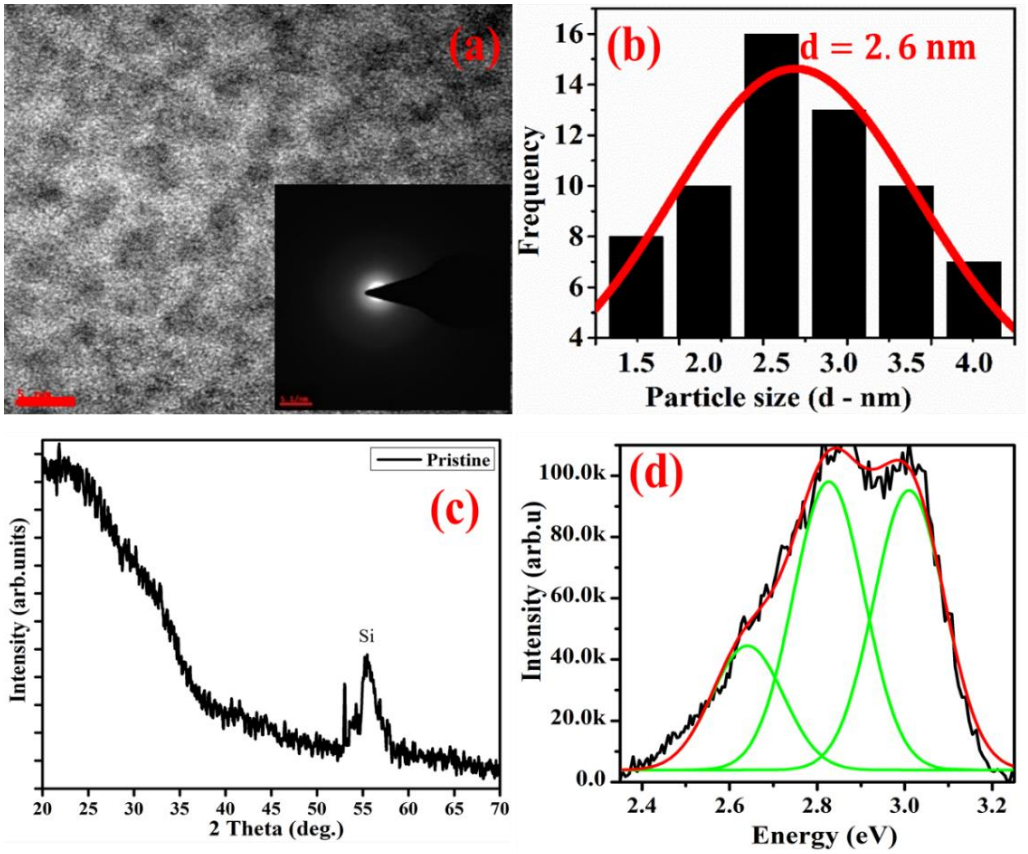

Fig-4.5: Characterization of pure HfO_2 films a) HR-TEM image on HfO_2 film (inset shows the SAED pattern), b) histogram image shows the average NPs size distribution, c) GIXRD spectra of as deposited film on Si substrate and d) photoluminescence spectra of HfO_2 thin films on Si substrate.

The excitation energy is chosen to be 3.8 eV, which is less than the band-gap of HfO_2, to monitor the midgap / defect states in these films. The peaks in the luminescence spectrum of as grown films are de-convoluted using Peak fit program to identify the defects in these films. Pristine samples exhibit three peaks at 2.6, 2.8 eV and 3.0 eV as shown in Fig. 4.5(d). It is well-known from the previous reports that the PL originates in HfO_2 from deep level defects due to Oxygen vacancies and interstitial states [39].

Some of the HfO_2 films deposited on Si substrates were annealed from 100 ºC to 500 ºC in the intervals of 100 ºC in the O_2. The annealing of all the films was carried out for 45 minutes. The GIXRD measurements were performed on all these pristine and annealed films and patterns shown in Fig-4.6. The pristine and annealed HfO_2 films (upto 400 ºC) show amorphous nature while the HfO_2 films annealed at 500 ºC show polycrystalline phase. This will give the basic information of annealing effect on HfO_2 thin films. All the observed peaks after annealing correspond to the monoclinic phase of HfO_2 and matching with the JCPDS file [PDF# 06-0318]. In Fig-4.9 the peaks at 2θ of 24.3º, 28.2º, 31.5º, 34.6º, and 35.5º belongs to the planes of (110), (-111), (111), (020) and (200) respectively. The grain size was calculated from the above mentioned Scherrer's formula in equation 4.1. The observed grain size for the film annealed at 500 C was around 7 nm.

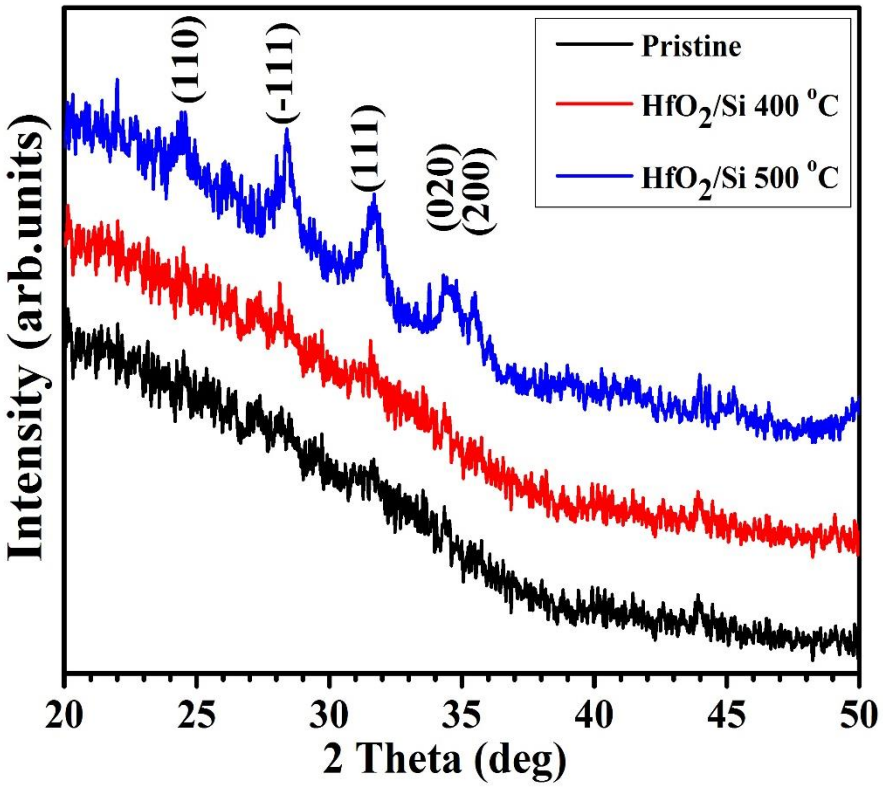

Fig- 4.6: GIXRD patterns of the annealed and un-annealed HfO_2 thin films.

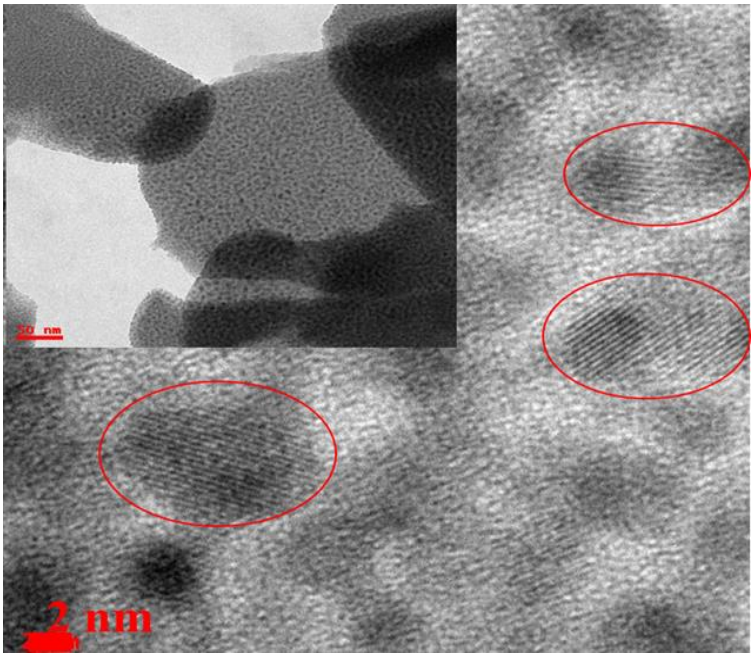

Fig- 4.7: HRTEM images of the HfO_2 film on Si substrate annealed at 500 º (inset shows the scratched HfO_2 thin flakes on TEM grid).

HfO_2 films on Si substrates annealed at 500 ºC were scratched and dropped on TEM grids for TEM measurements. The HR-TEM image is shown in Fig-4.7. TEM images revealed the formation of crystalline HfO_2 nano grains/ particles. The size of each of the nano grain was around 3-5 nm. This result is in good agreement with the GIXRD data.

4.3.2 SHI induced phase transformations

a) Electron microscopy and diffraction

Films deposited on TEM grids and Si substrates were subjected to 100 MeV Ag ion irradiation under same conditions in same run. After SHI irradiation, the nanoparticles tend to acquire spherical shape. The average particle size is found to increase with fluence as shown in Table-4.2. Initially, the average size of HfO_2 nano clusters was around 2.6 nm. After irradiation the HfO_2 NPs sizes were estimated to be 2.8 nm, 3.6 nm and 4.4 nm for fluences of 3×10^{12} ions/cm^2, 1×10^{13} ions/cm^2, and 3×10^{13} ions/cm^2 respectively. More significantly, the SAED patterns and HRTEM images show in in Fig-4.8 (b-d) confirm the formation of monoclinic phase of HfO_2 nano-crystals in irradiated samples. The measured inter-planar spacings of observed sets of planes in these crystallites (d = 0.31, 0.28 nm) correspond to (-111) and (111) planes of monoclinic HfO_2. Here it is important to note that these films were deposited on TEM grids and not on a smooth Si surface. Films are reasonably continuous even after highest fluence, as evidenced by the TEM and SEM images shown in Fig-4.4. The electron diffraction

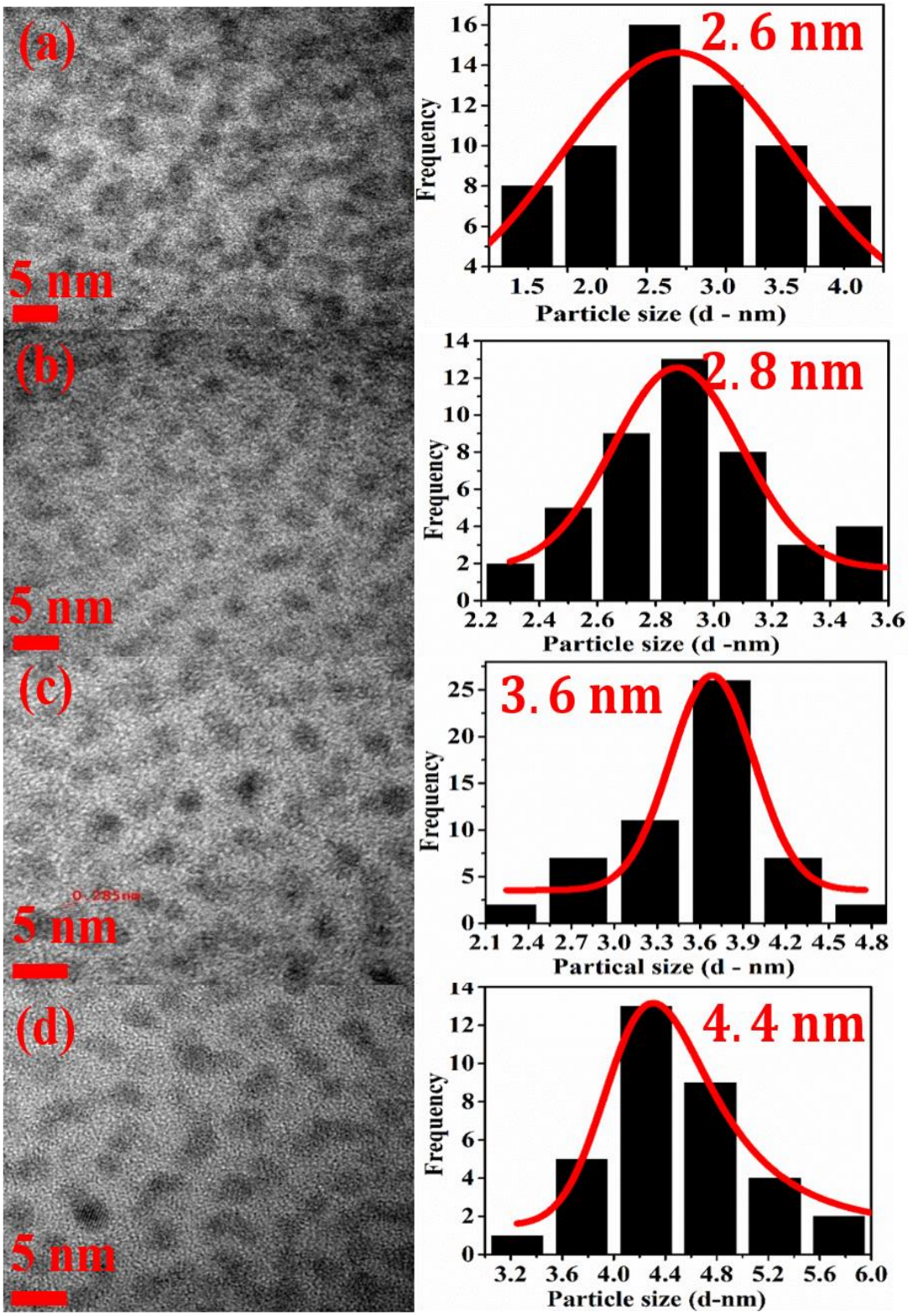

Fig-4.8: HRTEM images of HfO_2 thin films deposited on TEM grids: a) as deposited sample b) with fluence 3×10^{12} ions/cm^2 c) with fluence 1×10^{13} ions/cm^2 d) with fluence 3×10^{13} ions/cm^2 (The histograms on RHS show corresponding size distribution of nanoparticles, estimated average size is also shown in corresponding histogram).

pattern shown in Fig 4-9(a) confirms the amorphous nature of as deposited HfO_2 nanoclusters. Hence this study enables us to investigate the effects of SHI irradiation on amorphous nano-clusters of HfO_2. The HRTEM image shown in Fig 4-9(b) corresponds to a sample subjected to a fluence of 1×10^{13} ions/cm^2. This image clearly shows the crystalline planes within the nanoparticle, further confirming the ion-induced crystallization of nano-grains. The measured inter-planar spacing (d = 0.28 nm) corresponds to that of (111) planes of monoclinic HfO_2. Inverse Fast Fourier Transforms (I-FFT) have been calculated fur further and most accurate analysis. The IFFT and the SAED patterns are shown in Fig 4-9(c) and 4-9(d) to further confirm the existence of monoclinic phase in irradiated samples corresponding to a fluence of 3×10^{13} ions/cm^2. Hence the TEM results of the pristine and irradiated samples indicate that the SHI irradiation can induce amorphous to crystalline phase transformation in HfO_2. The observed ion induced crystallization of HfO_2 NPs is consistent with the previous reports of ion-induced crystallization of NPs in general [40-43]. However, to the best of our knowledge, there are no reports on swift heavy ion induced crystallization of HfO_2 NPs.

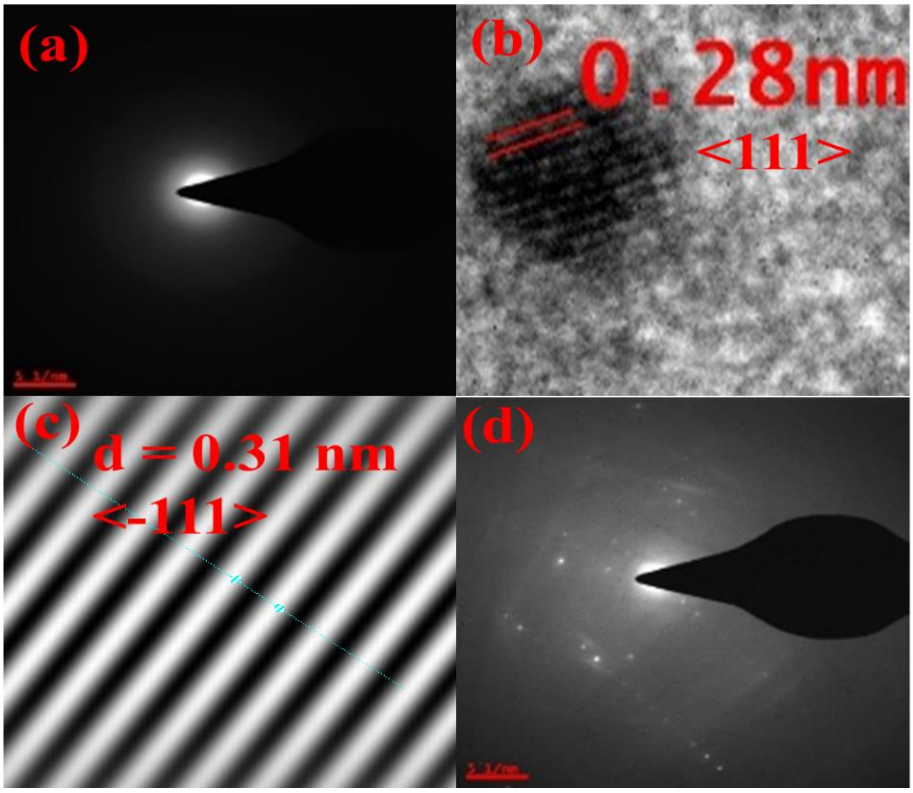

Fig-4.9: a) SAED pattern of the pristine sample b) HRTEM image of a sample subjected to a fluence of 1×10^{13} ions/cm^2. c) and d) are IFFT and SAED patterns a sample subjected to a fluence of 3×10^{13} ions/cm^2.

b) X-Ray diffraction analysis:

SHI irradiation of HfO_2 thin-films deposited on Si substrates were characterized by GIXRD measurements. Grazing incidence is an appropriate technique for analyzing thin films by X-Ray diffraction. The diffraction patterns of pristine and irradiated samples are shown in Fig-4.10. A diffraction peak at about 55^o, corresponding to Si-substrate appears in all pristine and irradiated samples. Multiple peaks are not expected, in the present experimental configuration, from Si substrates as they are single crystal (100) wafers. Only one peak is observed in pristine sample.

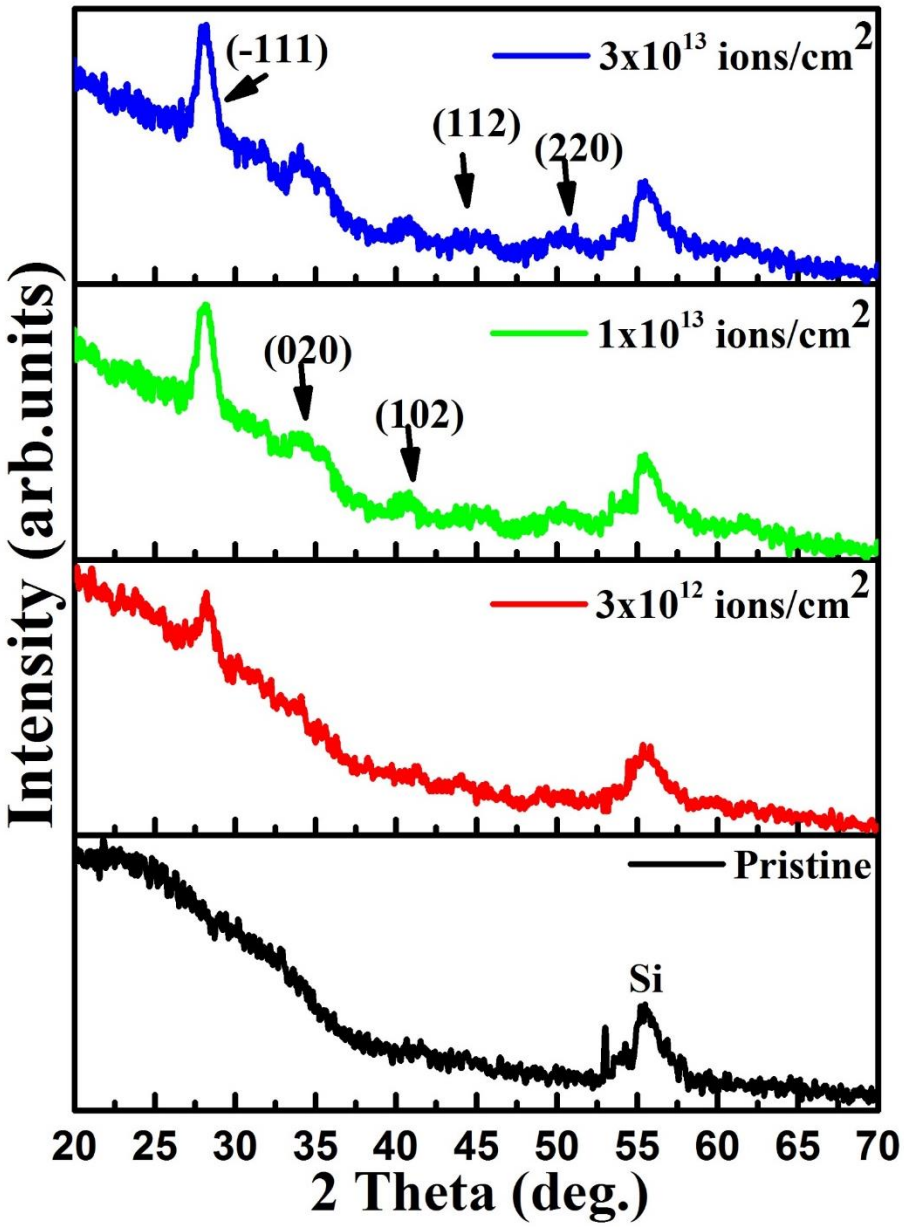

Fig-4.10: GIXRD patterns of pristine and irradiated HfO_2 thin-films deposited on Si substrates (fluence is mentioned within the figure).

Hence the films in as deposited samples showed amorphous nature whereas the irradiated samples consisted of Nano-crystallites, confirming the ion induced crystallization effects. The lowest dose sample exhibits only one peak (i.e (-111)) of monoclinic HfO_2. However, the evolution of other peaks with increase in dose is evident in corresponding XRD patterns. Here it is important to note that the film thickness is almost same for all pristine and irradiated samples. Hence similar diffraction pattern with same peak intensities are expected in the absence of irradiation. The observed evolution of peaks as a function fluence unambiguously confirms the improved crystallization during SHI irradiation.

The systematic increase in the intensity of various peaks that correspond to monoclinic phase of HfO_2, shows direct dependence of phase formation on ion fluence. It is important to note that all the observed peaks correspond only to the monoclinic phase of HfO_2 confirming a single crystalline phase at all doses. These results are consistent at least qualitatively with TEM analysis, presented in previous section, of nanostructured HfO_2 thin-films deposited on TEM grids in same run. All irradiated samples show diffraction peaks at 28º of 2θ corresponding to the (-111) planes of monoclinic HfO_2 crystallites as per JCPDS file [PDF# 06-0318]. The average size of particles was calculated using this peak by employing the Scherrer's formula as given by [44].

$$d = \frac{0.94\lambda}{\beta cos\theta} \tag{4.1}$$

where λ is the wavelength of X-rays (Cu Kα radiation, λ = 1.5405 Å), β is the full width at half-maximum of the XRD peak and θ is the Bragg diffraction angle. The estimated particle sizes are given in Table-4.2.

Table 4.2: HfO_2 particle size from HRTEM and GIXRD.

Sample Name	**Fluence** (ions/nm^2)	**Particle Size (nm)**	
		HRTEM	**GIXRD**
HfO_2/Si-1	Pristine	2.6	--
HfO_2/Si-2	3 x 10^{12}	2.8	5.1
HfO_2/Si-3	1 x 10^{13}	3.6	7.3
HfO_2/Si-4	3 x 10^{13}	4.4	7.3

The estimated average sizes of particles, with the help of TEM and GIXRD analysis, are shown in Fig-4.11 as a function of ion fluence. The difference in the particle size estimated by TEM and GIXRD may be attributed to the difference in substrate on which the films were deposited. As mentioned earlier, the growth kinetics and irradiation induced changes depend on the nature and morphology of substrates. However, it was observed that the average particle size increases with irradiation fluence in both cases. The results on the films deposited on two different substrates are in qualitative agreement. XRD results further establish the formation of nano-crystalline monoclinic HfO_2 films when amorphous HfO_2 films were subjected to 100 MeV Ag ion irradiation. The average grain / particle size is found to increase with increase in fluence. The growth of particles during SHI irradiation may be attributed to the possible agglomeration of NPs within the effective region, by SHI induced diffusion processes.

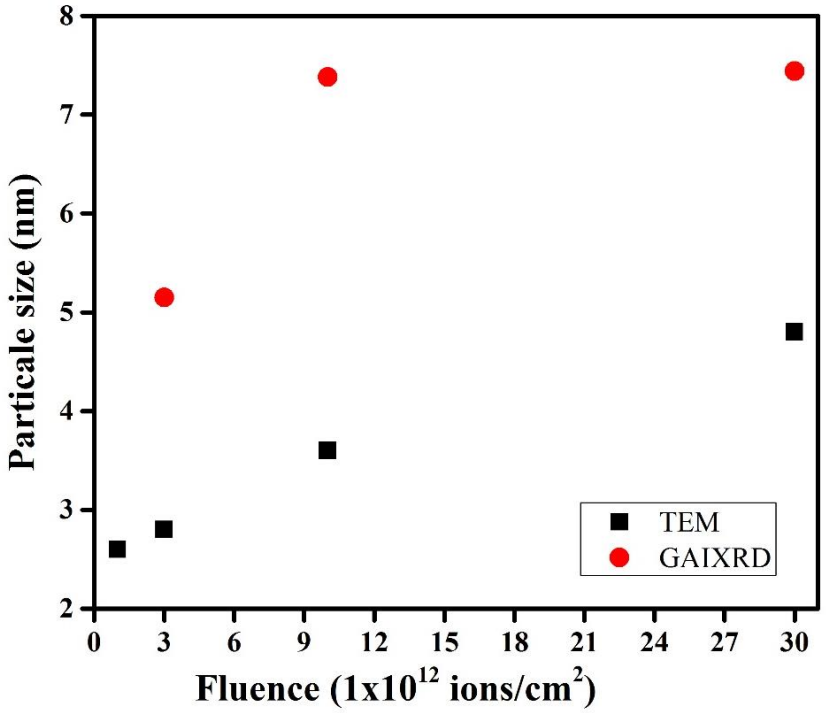

Fig- 4.11: Particle size as a function of fluence, obtained from HRTEM and GIXRD measurements.

c) Kinematics of the SHI induced defects:

The PL measurements were performed on both pristine and SHI irradiated HfO_2 NPs which were deposited on Si substrates using RF magnetron sputtering. PL spectra of as deposited samples have already been discussed in the above section and the luminescence spectra of SHI irradiated samples are shown in Fig-4.11. The excitation energy is chosen to be 3.8 eV, which is less than the band-gap of HfO_2, which is 5.7 eV, to monitor the defect states in these films.

Usually, the luminescence of the material is either due to quantum confinement effect or due to mid-bandgap defect states. To monitor this, we have calculated the Bohr exciton radius of HfO_2 NPs. The effective masses of electron and hole in monoclinic HfO_2 are 1.1 and 1.6 in Oxygen defected m-HfO_2 [45]. Bohr exciton radius for HfO_2 NPs is calculated by using the well-known formula

$$a_{ex} = a_H \,.\, \varepsilon_r \,.\, \frac{m_0}{\mu} \tag{4.2}$$

were a_{ex} is Bohr exciton radius, a_H is the Bohr radius of Hydrogen (0.53 A^o), ε_r is the relative dielectric constant, m_0 is the free electron mass and μ is the effective electron and hole reduced mass. The calculated Bohr exciton radius for monoclinic HfO_2 NPs is estimated to be around 2.1 nm by following the procedure in ref. [46, 47]. In all the above cases the HfO_2 NPs size is larger than the calculated Bohr exciton radius, hence we don't expect the quantum confinement effects. It is proved that the observed PL luminescence is due to intra band transitions or defect-states in HfO_2. As deposited HfO_2 NPs showed a broad emission spectrum (from 2.4 to 3.0 eV) in visible region. Further, de-convolution of the pristine peak exhibits three peaks at 2.6 eV, 2.8 eV and 3.0 eV (see Fig. 4.12(a)).

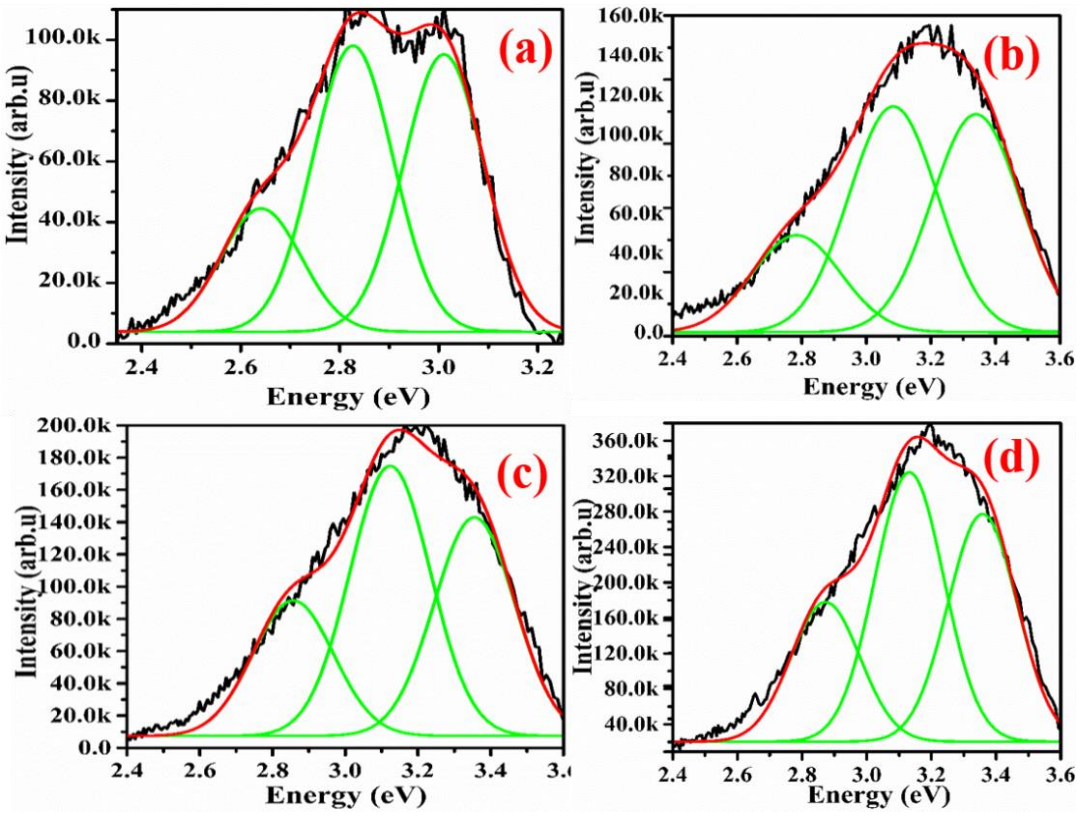

Fig-4.12: PL spectra of HfO_2 thin films: a) as deposited sample b) with fluence 3×10^{12} ions/cm^2 c) with fluence 1×10^{13} ions/cm^2 d) with fluence 3×10^{13} ions/cm^2.

As a result of SHI irradiation, the emission peak is shifted to 3.2 eV and the intensity at this wavelength increases with increase in fluence. The luminescence peaks are de-convoluted using Peak fit program to identify the defects in these films. The deconvulated peaks in irradiated samples correspond to 2.8, 3.1 eV and 3.3 eV as shown in Fig-4.12(b), 12(c), and 12(d). It is known from the earlier reports that the PL originates in HfO_2 from deep level defects due to Oxygen vacancies and interstitial states [28, 48]. These O vacancies are electron traps below the conduction band edge (E_c) [49]. It was reported that the PL peaks can be attributed to the presence of different types of poly O vacancies and F-centers in HfO_2 [50]. J.G. Mendoza et al. [51] reported on the increase in emission intensity from HfO_2 films when the annealing temperature is increased from 300 °C to 600 °C.

Here we observe a small blue shift together with increase in intensity upon SHI irradiation suggesting that the electronic excitation induced by SHI caused annealing and rearrangement of defects. This is further supported by the direct observation of crystalline grains in SHI irradiated HfO_2 films by TEM/SAED and GIXRD. The change in defect configuration might play an important role in the observed "amorphous" to "crystalline" transformation in these samples upon SHI irradiation. The defect reconfiguration is essential to take care of the expected changes in strains within the films during SHI induced phase transitions.

4.3.3 Thermal Spike Analysis and Discussion:

The observed swift heavy ion irradiation induced modifications may be examined in the light of thermal-spike model [52, 53]. Following two equations (eq. 4.3 and 4.4) are well-known and well-accepted coupled differential equations to study the evolution of electronic and lattice temperature in Thermal Spike model,

$$C_e \frac{\partial T_e}{\partial t} = \frac{1}{r}\frac{\partial}{\partial r}\left[rK_e \frac{\partial T_e}{\partial r}\right] - g(T_e - T_\alpha) + A(\mathrm{r,t}) \tag{4.3}$$

$$C_a \frac{\partial T_a}{\partial t} = \frac{1}{r}\frac{\partial}{\partial r}\left[rK_a \frac{\partial T_a}{\partial r}\right] \mp g(T_e - T_\alpha) \tag{4.4}$$

where C_e *and* C_a are specific heats of electronic and atomic subsystems, respectively, K_e, K_a are thermal conductivities. T_e, T_a are electronic and atomic temperatures. g is electron phonon coupling parameter and r is the radial distance from ion path. It was previously shown that the SHI irradiation can lead to crystalline to crystalline phase transitions in HfO_2 driven by the electronic energy loss [54]. Presently there are two competing models, namely Thermal spike model [55] and Coulomb explosion model [56], to explain the ion induced phase transitions

and latent track formation in solids. Both these models are generally used to estimate track parameters. However it was shown that the effect of thermal spike is more significant in bulk HfO_2 [54]. The effective threshold electronic energy loss (S_{et}) for transformation of HfO_2 from amorphous to monoclinic phase can be calculated in the framework of thermal-spike model [57, 58] and is given by,

$$S_{et} = \pi a_0{}^2 C\rho \frac{[T_p - T_0]}{g} \tag{4.5}$$

where T_p and T_0 are the phase transition and irradiation temperatures, respectively. a_0 and g are the radial Gaussian distribution of temperature and conversion factor. ρ and C are the density and specific heat of HfO_2. The calculated threshold energy (20 keV/nm) is less than the electronic energy loss (23.2 keV/nm) of incident ion in this study. Hence, monoclinic NPs of HfO_2 may form due to 100 MeV Ag ion irradiation of amorphous HfO_2 thin films. Fig-4.13 shows the results of thermal spike calculations performed for HfO_2 by considering our experimental conditions and the standard physical properties of bulk HfO_2. Temperature profiles in cylindrical zones of different radii from the ion path are plotted as a function of lapsed time after the incidence of an energetic ion.

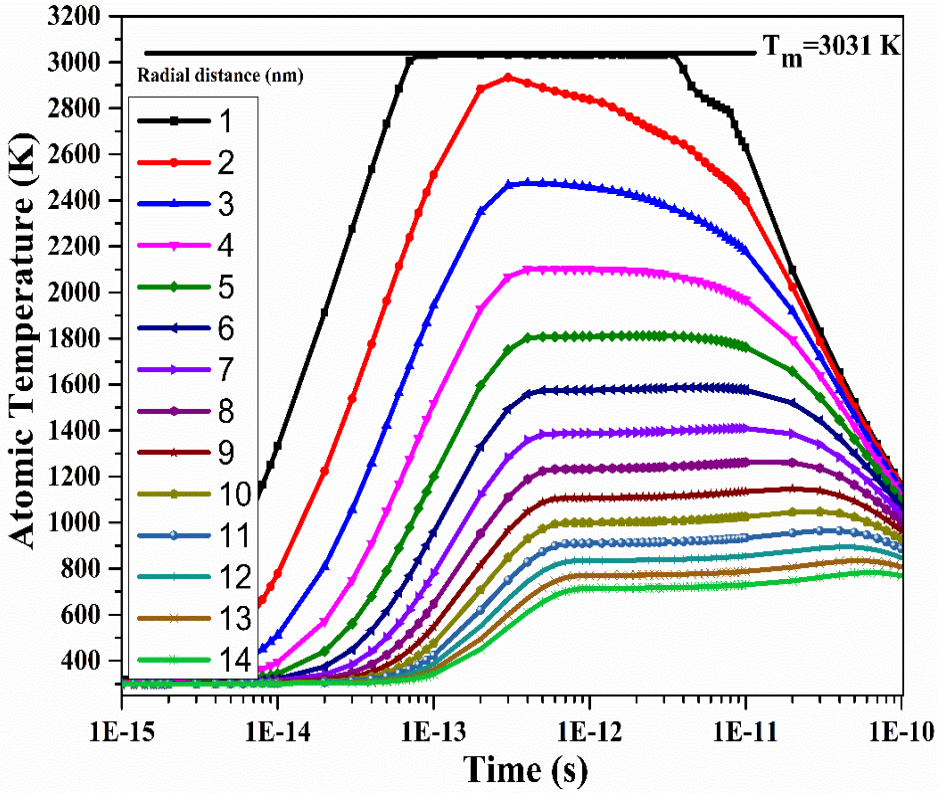

Fig-4.13: Results of Thermal-spike calculations of 100 MeV Ag ion effects in HfO_2.

Here it is important to note that HfO_2 is known to exist in three distinct phases, namely monoclinic (~500 to 1000 °C), tetragonal (1000 -1700 °C) and cubic (~ 1700 - 2500 °C) phases. The formation of monoclinic phase and the absence of any tetragonal peaks suggest that the average temperature is below 1000 °C in the region of interest. Thermal spike calculations shown in Fig-4.13 suggest that the temperature is below 1000 °C (1273 K) in a region of 10 nm from the ion path. Hence the effective region of interest is considered to be 10 nm around ion path to interpret these results. However, it is important to note that the S_e in this experiment is less than the value that is required for track formation in HfO_2. Further, there are no reports on the direct observation of tracks in HfO_2 under SHI irradiation. Hence our study suggests that the 100 MeV Ag ion irradiation induced effects are limited to and/or significant within a cylindrical region of about 10 nm from the path of ion. The radial Gaussian distribution of temperature is more or less equal within the effective region of interest (a ~ 10 nm).

4.3.4 SHI induced phase transitions in HfO_2:

Benyagoub et al. [59] have earlier reported a crystalline to crystalline transformation from monoclinic to tetragonal phase in bulk HfO_2 when S_e is greater than 18 keV/nm. It is generally believed that ion irradiation leads to the creation of damage. However, the present work is in support of the another important aspect of SHI irradiation that it can cause ordering of the material and can lead to the improvement in crystallinity and/or induce phase transformations. In the present work, the material is in thin-film form which consisted of amorphous clusters. These amorphous clusters are found to be transformed to the monoclinic state under SHI irradiation. However, in contrast, the thick films exhibited a monoclinic to tetragonal transition. Hence our study suggests that the initial state of the material plays a critical role in determining the effects of SHI irradiation. The films that were initially in the amorphous state got transformed to monoclinic state whereas those, in monoclinic phase got transformed to tetragonal phase under same irradiation conditions. When it comes to ion induced size and shape modifications of nano-particles, if the interparticle separation is small, there is an increase of particle size [59]. In our case, the initial particle is 2.6 nm, and interparticle size is around 2-3 nm which is within the effected region (or ion track) as estimated in previous section. Most importantly, the average size and separation of NPs are very less when compared to ion induced thermal Gaussian distribution (~ 10 nm). The diffusion of the nearby HfO_2 small NPs together can cause the formation of bigger NPs. Even though the temperature increase at NP sized track radius is expected to be almost 1800-2000 K, the thermal conductivity is very small in thin films (0.27 - 0.49 W. m^{-1}. K^{-1}) when compared to thicker films (1.2 – 1.5 W. m^{-1}.

K^{-1}) [60]. This is in agreement in the evolution of monoclinic phase and the grain growth in HfO_2 thin-films during SHI irradiation.

4.4 Conclusions

HfO_2 NPs were synthesized by using RF Magnetron sputtering method. As deposited HfO_2 NPs were found to be amorphous in nature and are non-spherical in shape. HRTEM analysis estimates that the average particle size is of the order of 2.6 nm. After SHI irradiation, the same particles got transformed into crystalline, non-agglomerated and well dispersed nano-clusters. The HRTEM, SAED, and GIXRD measurements confirm the monoclinic phase of NPs in SHI irradiated films. The crystallite size is found to increase from 2.6 to 4.4 nm with increase in irradiation fluence. This growth of nano-particles is attributed to the possible agglomeration of NPs by SHI induced diffusion process. SAED, HRTEM, I-FFT and GIXRD analysis suggest that the nanoparticles are of stoichiometric HfO_2 at all fluences because the estimated inter-planar distances exactly match with (111) and (-111) planes of HfO_2. Hence there are no compositional changes within the clusters that are of our interest, although the stoichiometric changes are expected in other regions of films under SHI irradiation. PL emission band confirms the existence of Oxygen vacancy defects in these films. Annealing and reconfiguration of these defects due to SHI irradiation were also evidenced by PL. Observed results are explained within the framework of thermal spike model. Finally, it is important to note that the amorphous clusters in thin-films got transformed to monoclinic phase after irradiation. The major conclusion is that the initial state of the material (like phase, size and inter particle separation of nanoparticle) determine the consequent effects induced by SHI irradiation. The sensitivity of the initial phase of HfO_2 to SHI irradiation is an important observation and is within in the framework of thermal spike model. The effect is observed in films deposited on both TEM grinds and Si substrates. The trend of SHI irradiation induced modifications is fund to be same, at least qualitatively, in these two sets of samples. These results give useful information for understanding the ion induced crystallization of NPs in general and HfO_2 NPs in particular. This technique may be employed to fabricate HfO_2 thin-films containing nano-crystallites with spatial selectivity.

4.5 References

1. Yu-Hsien Lin, Hsin-Chiang You, Jin-Shi Hong, Jay-Chi Chou, Jyun-Hong Shih, *Advances in Information Sciences and Service Sciences*, **4**, 18-26 (2012).

2. Souvik Mahapatra, S. Shukuri, and Jeff Bude, *IEEE Trans. Electron Devices*, **49,** 1302-1307 (2002).
3. H. Zhu, C. Tang, L. R. C. Fonseca, R. Ramprasad, *J. Mater. Sci.* 47, 7399–7416 (2012).
4. A. Callegari, E. Cartier, M. Gribelyuk, H.F. Okorn-Schmidt and T. Zabel, *J. Appl. Phys*. **90**, 6466 (2001).
5. W. J. Zhu, Tso-Ping Ma, *IEEE Electr. Device. Lett.* **23**, 2 (2002).
6. Buhro W.E. and Colvin V.L., *Semiconductor nanocrystals: Shape matters, Nat. Mater* **2**, 138-139 (2003).
7. Jermey N, A. Matthews, *Physics Today* **61**, 25 (2008).
8. M.L. Green, E.P. Gusev, R. Degraeve, E.L. Garfunkel, *J. Appl. Phys*. **90**, 2057 (2001).
9. T.D. Dongale, K.V. Khot, S.V. Mohite, S.S. Khandagale, S.S. Shinde, V.L. Patil, S.A. Vanalkar, A.V. Moholkar, K.Y. Rajpure, P.N. Bhosale, P.S. Patil, P.K. Gaikwad, R.K. Kamat, *J. Nano- Electron. Phys,* **8**, 04030 (2016).
10. J.F. Justin, A. Jankowiak, *Journal of Aerospace Lab*, Issue-3 (2011).
11. E. P. Simonenko, D. V. Sevast'yanov, N. P. Simonenko, V. G. Sevast'yanov and N. T. Kuznetsov, *Russian Journal of Inorganic Chemistry,* **58**, 1669–1693 (2013).
12. U. Schroeder, S. Mueller, J. Mueller, E. Yurchuk, D. Martin, C. Adelmann, T. Schloesser, R. van Bentum, and T. Mikolajicka, *ECS Journal of Solid State Science and Technology*, 2 (4) N69-N72 (2013).
13. Suveen Kumar, Saurabh Kumar, Sachchidanand Tiwari, Shine Augustine, Saurabh Srivastava, Birendra Kumar Yadav, Bansi Dhar Malhotra, *Sensors and Actuators* B **235**, 1–10, (2016).
14. Brian R. Dorvel, Bobby Reddy Jr, Jonghyun Go, Carlos Duarte Guevara, Eric Salm, Muhammad Ashraful Alam, and Rashid Bashir, *ACS Nano* **6**, 6150-6164 (2012).
15. J. Larkin, R. Henley, D. C. Bell, T. Cohen-Karni, J. K. Rosenstein, and M. Wanunu, *ACS Nano* **7**, 10121 **(**2013).
16. M. Lee, N. Zine, A. Baraket, M. Zabala, F. Campabadal, R. Caruso, M. G. Trivella, N. J. Renaulta, and A. Errachid, *Sens. Actuator B-Chem.* **175**, 201 (2012).
17. L. Maggiorella, G. Barouch, C. Devaux, A. Pottier, E. Deutsch, J. Bourhis, E. Borghi, and L. Levy, *Future Oncol.* **8**, 1167 (2012).
18. Jiajie Qi, Xingping Zhou, Colloids and Surfaces A: Physicochem. *Eng. Aspects*, **487**, 26–34 (2015).
19. S. A. Eliziario, L. S. Cavalcante, J. C. Sczancoski, P. S. Pizani, J. A. Varela, J. W. M. Espinosa, E. Longo, *Nanoscale Res. Lett.* **4**, 1371–1379 (2009).

20. Jonathan De Roo, Katrien De Keukeleere, Jonas Feys, Petra Lommens, Zeger Hens, Isabel Van Driessche, *J Nanopart. Res.* **15**,1778 (2013).
21. P. Rauwel, E. Rauwel, C. Persson, M. F. Sunding and A. Galeckas, *J. Appl. Phys.* **112**, 104107 (2012).
22. Ananthakumar Ramadoss, Karthikeyan Krishnamoorthy, Sang Jae Kim, *Materials Research Bulletin* **47**, 2680–2684 (2012).
23. Jelena Buha, Denis Arcon, Markus Niederberger and Igor Djerdj, *Phys. Chem. Chem. Phys.*, **12**, 15537–15543 (2010).
24. M. A. Pugachevskii and V. I. Panfilov, *J. Appl. Spe.* **81**, 4 (2014).
25. W. Umrath, Fundamentals of Vacuum Technology. Leybold vacuum products and reference book 2001/2002 Leybold, Cologne, (2001).
26. M. Toledano-Luque, E. San Andrés, A. del Prado, I. Mártil, M. L. Lucía, G. González Díaz, F. L. Martínez, W. Bohne, J. Röhrich, and E. Strub, *J. Appl. Phys*. **102**, 044106 (2007).
27. A. G. Znamenski and V. A. Marchenko, *Tech. Phys*. **43**, 766 (1998).
28. N. Manikanthababu, M. Dhanunjaya, S.V.S. Nageswara Rao, A.P. Pathak, *Nucl. Instr. Meth. Phys. Res. B* **379**, 230–234 (2016).
29. N. Manikanthababu, N. Arun, M. Dhanunjaya, S.V.S. Nageswara Rao & A. P. Pathak, *Radiation Effects & Defects in Solids*, **171**, 77–86 (2016).
30. M. Dhanunjaya, N. Manikanthababu, A. P. Pathak, and S. V. S. Nageswara Rao, AIP Conference Proceedings **1731**, 080071 (2016).
31. S. Raoux, G. W. Burr, M. J. Breitwisch, C. T. Rettner, Y. C. Chen, R. M. Shelby, M. Salinga, D. Krebs, S. H. Chen, H. L. Lung and C. H. Lam, *IBM J. RES. & DEV.* **52**, 465-479 (2008).
32. S Aldana, P García-Fernández, Alberto Rodríguez-Fernández, R Romero-Zaliz, M B González, F Jiménez-Molinos, F Campabadal, F Gómez-Campos and J B Roldán, *J. Phys.* D: *Appl. Phys.* **50**, 33 (2017).
33. Irini Michelakaki, Panagiotis Bousoulas, Spyros Stathopoulos, Nikos Boukos and Dimitris Tsoukalas, *J. Phys.* D: *Appl. Phys.* **50**, 4 (2016).
34. Kiran Jeet, V. K. Jindal, L. M. Bharadwaj, D. K. Avasthi, and Keya Dharamvir, J. Appl. Phys. **108**, 034302 (2010).
35. Sunil Kumar Samji, Brajesh Tiwari, M. Krishna Surendra, and M. S. Ramachandra Rao, Appl. Phys. Lett. **104**, 152106 (2014)

36. H.S. Lokesha, K.R. Nagabhushana, Fouran Singh, *Nucl. Instr. Meth. B* **379**, 131–135 (2016).
37. Limin Zhang, Weilin Jiang, Amila Dissanayake, Tamas Varga, Jiandong Zhang, Zihua Zhu, Dehong Hu, Haiyan Wang, Charles H Henager Jr and Tieshan Wang, *J. Phys.* D: *Appl. Phys.* **49**, 3 (2015).
38. J. F. Ziegler, "SRIM-2003". *Nucl. Instr. Meth. B*. 219-220: 1027 (2004).
39. N Mehta, K Singh and N S Saxena, Journal of Physics *J. Phys.* D: *Appl. Phys* **41**, 13 (2008).
40. Navdeep Bajwa, Alka Ingale, D. K. Avasthi, Ravi Kumar, A. Tripathi, Keya Dharamvir, and V. K. Jindal, *J. Appl. Phys.* **104**, 054306 (2008).
41. A. Biswas, R. Gupta, N. Kumar, D. K. Avasthi, J. P. Singh, S. Lotha, D. Fink, S. N. Paul, S. K. Bose, *Appl. Phys. Lett.* **78**, 4136 (2001).
42. P. Jegadeesan, S. Amirthapandian, Kitheri Joseph, C. David, B.K. Panigrahi, K.V. G Kutty, *Adv. Mater. Lett.*, **6**, 224-227 (2015).
43. Zs. Baji, A. Szanyo, Gy. Molnár, A. L. Tóth, G. Peto, K. Frey, E. Kotai, and G. Kaptay, *J. Nanosci. Nanotechnol*, **12**, 1–7, (2012).
44. P. Scherrer, *Göttinger Nachrichten Gesell.*, **2**, 98 (1918).
45. T. V. Perevalov and V. A. Gritsenko, S. B. Erenburg and A. M. Badalyan, Hei Wong, and C. W. Kim, *J. Appl. Phys.* **101**, 053704 (2007).
46. R. S. Knox, Theory of excitons, Solid state physics (Ed. by Seitz and Turnbul, Academic, NY), 5, 1963.
47. D. R. Islamov, V. A. Gritsenko, T. V. Perevalov, *ECS Transactions*, **69**, 197-203, (2015).
48. Sachin Kumar, Animesh K. Ojha, *Journal of Alloys and Compounds* **644**, 654–662 (2015).
49. S. A. Elizia´rio, L. S. Cavalcante, J. C. Sczancoski, P. S. Pizani, J. A. Varela, J. W. M. Espinosa, E. Longo, *Nanoscale Res Lett* **4**, 1371–1379 (2009).
50. D. Muñoz Ramo, J. L. Gavartin, and A. L. Shluger, *Phys. Rev. B* **75**, 205336 (2007).
51. J. Guzma´n Mendoza, M.A. Aguilar Frutis, G. Alarco´n Flores, M. Garcı, Hipo´lito, A. Maciel Cerda, J. Azorı´n Nieto, T. Rivera Montalvo, C. Falcony, *Applied Radiation and Isotopes* **68**, 696–699 (2010).
52. A. Meftah, F. Brisard, J. M. Costantini, E. Dooryhee, M. Hage-Ali, M. Hervieu, J. P. Stoquert, F. Studer, and M. Toulemonde, *Phys. Rev. B* **49**, 12457 (1994).

53. Saif A. Khan, Ambuj Tripathi, Marcel Toulemonde, Christina Trautmann, Walter Assmann *Nucl. Instr. Meth. Phys. Res. B* **314**, 34–38 (2013).
54. A. Benyagoub, *Phys. Rev. B* **72**, 094114 (2005).
55. F. Seitz and J. S. Koehler, *Solid State Phys.* **2**, 305 (1956).
56. R. Fleicher, P. B. Price, and R. M. Walker, *Nuclear Tracks in Solids, Principles and Applications* University of California Press, Berkeley, (1975).
57. A. Benyagoub, *Eur. Phys. J.* B **34**, 395 (2003).
58. D.K. Avasthi, Y.K. Mishra, F. Singh, J.P. Stoquert, *Nucl. Instrum. Methods Phys. Res. B* **268**, 3027–3034 (2010).
59. Fouran Singh, S. Mohapatra, J.P. Stoquert, D.K. Avasthi, J.C. Pivin, *Nucl. Instrum. Methods Phys. Res.* B **267**, 936–940 (2009).
60. Matthew A. Panzer, Michael Shandalov, Jeremy A. Rowlette, Yasuhiro Oshima, Yi Wei Chen, Paul C. McIntyre, and Kenneth E. Goodson, *Ieee Ele. Dev. Lett.* **30,** 1269-1271, (2009).

Grain Fragmentation and Phase Transformations in Hafnium Oxide Films Induced by SHI Irradiation

This chapter provides the brief report on 100 MeV Ag ion irradiation induced modifications in Hafnium oxide (HfO_2) films deposited by Radio Frequency (RF) magnetron sputtering method. The phase transformations, grain fragmentation and defect reconfiguration have been observed within the film after SHI irradiation. These changes were observed by employing the Grazing Incident X-Ray Diffraction (GIXRD), Field Emission Scanning Electron Microscope (FESEM), and Photo Luminescence (PL) measurements. Ion induced damage cross section and track diameters have been calculated from the GIXRD peak integrals. The ion induced changes in the photoluminescence spectra are attributed to the shallow oxygen defects and F-centers present in hafnium oxide films. Particularly the anisotropic thermal expansion in the nano-grains can cause grain fragmentation. Ion-induced defect annihilation, strain relaxation, phase transformation and grain fragmentation are interdependent processes and their mutual dependency is responsble for the observed changes in the films.

5.1 Introduction

As discussed in the previous chapters Swift Heavy Ion (SHI) irradiation is a well-known and versatile technique to synthesize, characterize and modify the materials [1]. Ion beam irradiation is a very precise tool to create the interdiffusion in films, fabrication of the embedded Nanoparticles (NPs) and to induce phase transformations [2-7]. During the passage of swift ions into the material or films, these ions deposit a huge amount of energy in the form of electronic and nuclear energy losses. This deposited high energy initially absorbed by the electrons in the material, eventually gets transferred to lattice and leads to the ion track formation, ion beam annealing, material modifications etc. [8, 9]. There are several reports on material modifications like amorphization, crystallization, amorphous to crystalline transformations and crystalline to amorphous transformations etc. [10-15].

As mentioned earlier Hafnium Oxide (HfO_2) is a contemporary gate material having a wide range of research activity in the fields of both electronics and optoelectronics. The variety of properties like high thermal stability on Si surface, wide bandgap (~5.7 eV), high dielectric constant (~ 25) and high refractive index (~2) lead this material to replace the conventional gate dielectric material (SiO_2) in Metal Oxide Semiconductor (MOS) devices[16]. High melting (2900 ºC) and boiling (3500 ºC) points make it a suitable refractory material in high temperature applications [17, 18]. The better cytocompatibility eventually put this material in the center stage in its applications for biosensors [16] and drug delivery in cancer therapy [19, 20]. The transperancy of HfO_2 films is 80 to 90 % for Ultra-Violet (UV) to the Infra-Red (IR) region, so that they can be used in bandpass filters, UV mirrors, astronomical charge coupled devices (CCDs), anti-reflective multilayer coatings for night-vision devices and IR optical devices [21-25].

It is well-known that the above-mentioned properties strongly depend on the phase, stoichiometry and surface morphology of the films. More importantly, the morphology is critical for sensing applications. Recent reports suggest that the phase and morphology can be engineered by employing SHI irradiation [26, 27]. However, the underlying mechanisms responsible for the observed phase and/or morphology change are still to be investigated in detail, which forms the basis for present work. Researchers have used various deposition techniques to synthesize the HfO_2 thin films. However, RF Magnetron sputtering method is more frequently used for thin film depositions, because it is easy to fabricate the thin films, effectively at low cost compared to the other deposition techniques. The quality of the film,

morphology, thickness of the deposited films can be tailored with deposition parameters like deposition power, deposition pressure and deposition time. Experimental results presented in previous chapter suggest that the SHI irradiation can induce grain growth and amorphous to crystalline (monoclinic) transformation in thin HfO_2 films (~10 nm) deposited by RF sputtering at low RF powers [28]. In another study, Benyagoub [29] suggested crystalline to crystalline (monoclinic to tetragonal) transformation in bulk HfO_2 under SHI irradiation. Here we present a study on the effects of SHI irradiation on the structural and surface properties of appropriately thick hafnium oxide film (~ 500 nm).

5.2 Experimental details

5.2.1 Sample preparation:

Hafnium Oxide films were deposited on Boron doped p-type Silicon (100) wafer with 1 -10 Ω-cm resistivity substrates using RF magnetron sputtering method at room temperature. The substrates are cut into 1×1 cm^2 dimensions to get the uniformity while depositing the films. A commercially purchased 2-inch diameter and 3 mm thick HfO_2 target having purity 99.99% was used for film deposition. Silicon substrates were cleaned ultrasonically in deionized water (DIW), acetone and isopropyl alcohol successively, each for 5 min and finally, these substrates were rinsed with DIW thoroughly. After completing the cleaning process, the substrates were immediately clamped to the substrate holder and substrate holder was loaded in the sputtering chamber. Initially, the sputtering chamber was evacuated to a base pressure of 9×10^{-6} mbar with the help of turbo molecular pump backed by a roughing pump. After reaching certain base pressure, a 20 Standard Cubic Centimeters per Minute (SCCM) of 99.99 % pure Argon (Ar) gas was introduced into the sputtering chamber using Mass Flow controller (MFC). The prior depositions were carried out at a pressure of 2.4×10^{-3} mbar. The target to substrate distance was maintained at 12.5 cm. A 120-W RF Power was used to deposit the films and deposition was carried out for 4 hours of time to get the thicker films. While depositing films, the substrate rotation (10 rpm) was used throughout the deposition. The pre-estimated thickness was 500 nm. Ambios XP 200 Profilometer was used to measure the film thickness, and it was estimated to be around 475 nm.

5.2.2 SHI Irradiation details:

The deposited thick HfO_2 films on Si substrates were subjected to 100 MeV Ag^{7+} SHI irradiation using a 15 UD tandem Pelletron accelerator at Inter University Accelerator Center (IUAC), New Delhi. The range and energy loss of ions in HfO_2 were estimated using Stopping

and Range of Ions in Matter (SRIM-2013) simulation code [30]. The calculated ion range (R), electronic energy loss (S_e) and nuclear energy loss (S_n) for 100 MeV Ag ions in HfO_2 were estimated to be 7.7 µm, 23.2 keV/nm and 0.15 keV/nm, respectively. The Hafnium Oxide film thickness was around 500 nm which is small compared to projected ion range 7.7 µm. The ion beam was scanned over 1×1 cm^2 of the sample area at a constant beam current of 1 particle nano-Ampere (pnA) to avoid the heating up of substrates. The ion fluence was varied from 3×10^{12} to 1×10^{14} ions/cm^2 by varying the irradiation time. The sample details and irradiation details are mentioned in Table-5.1.

Table 5.1: Sample details, ion energy, irradiation and SRIM Calculation details**.**

Sample Type	**Irradiation Fluence (ions/cm^2)**	**Ion Energy (MeV)**	**Average stopping power (within the HfO_2 film (~500 nm))**	
Set-B (~500 nm)			**Electronic (S_e) (keV/nm)**	**Nuclear (S_n) (keV/nm)**
HfO_2/Si-1	Pristine	Ag^{7+} 100 MeV	23.2	0.15
HfO_2/Si-2	3 x 10^{12}			
HfO_2/Si-3	1 x 10^{13}			
HfO_2/Si-4	3 x 10^{13}			
HfO_2/Si-5	1 x 10^{14}			

The pristine and SHI-irradiated films were characterized using different techniques. Field Emission Scanning Electron Microscope (FE-SEM: Carl ZEISS, FEG, ultra-55) was used to scan the surface morphology, evolved grains and to measure the film thickness from the cross-sectional image. Bruker D8 Advance diffractometer with Cu K_α source (λ = 0.154 nm) was used to estimate the possible phase changes in films. Photo Luminescence (PL) measurements were performed using Fluorolog, Xenon lamp, 450 W, having a resolution of 0.3 nm. Rutherford Backscattering Spectroscopy (RBS) measurements have been performed on the sample to estimate the composition and thickness of films. These measurements were performed using 2 MeV He^{2+} ions at a scattering angle of 165º at IUAC, New Delhi. The SIMNRA-7.01 [31] was used to simulate the acquired RBS spectra.

5.3 Results and discussion

5.3.1 Synthesis and characterization of as-deposited samples:

Thick HfO_2 films deposited by RF magnetron sputtering were studied before and after irradiation by various characterization techniques. Initially the film thickness was measured with Ambios XP 200 Profilometer, and it was estimated to be around 475 nm. Similarly, the RBS measurement was also performed to estimate the thickness and composition of films. Calibration offset and energy per channel were estimated to be 96 keV and 0.961 keV/ch respectively using a calibration sample (Au/SiO_2) to simulate the RBS spectrum shown in Fig-5.1. The estimated areal density is 2550×10^{15} atoms/cm^3 which is equal to 430 nm of film thickness assuming the standard density of HfO_2 and film composition was found to be around $HfO_{2.7}$. Inset of Fig-5.1 depicts the cross-sectional FESEM image of the pristine sample and it indicates a film thickness of 460 nm which is in agreement with the nominal value of 500 nm and with measured values form Profilometer and RBS measurements.

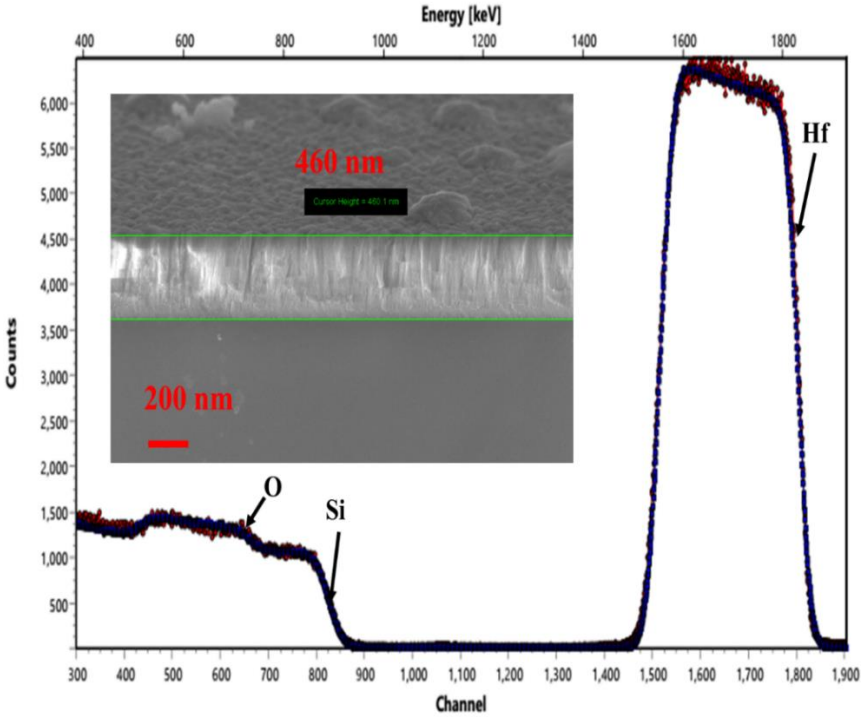

Fig-5.1: RBS spectrum of as deposited HfO_2 thick film. Solid line indicates the fit obtained by SIMNRA simulation. (inset shows the cross sectional FESEM image. Measured film thickness is 460 nm as shown in the inset).

The microstructure, surface morphology and the development of grain sizes of the films are studied by using the FESEM measurements. The pristine and SHI-irradiated HfO_2 films have

been studied using 5 kV Extra High Tension (EHT) electron gun at different magnification levels. The FESEM image of the pristine sample is shown in Fig-5.2. The surface image of the pristine sample shows the elongated nano-flake like structures, and the average nano-flake size is around 70 nm along its long axis and width of the nano flake varied from 20 nm to 30 nm. The first analysis confirmed that the film morphology and the grain (nano-flake) size depends on the RF magnetron sputtering deposition parameters, like deposition power and deposition pressure, when compared to previous reports [28, 32-34]. On closer observation, we notice non-uniform, inhomogeneous and irregular grains at higher deposition rates, which is consistent with irregular columnar grain growths of other materials [35]. Each of the large grain looks like a combination of smaller grains each with size around 15 nm. In general, this type of morphology is less dense, loosely packed and corresponds to highly strained structures [36]. The adhesion between the grains in the film is very poor.

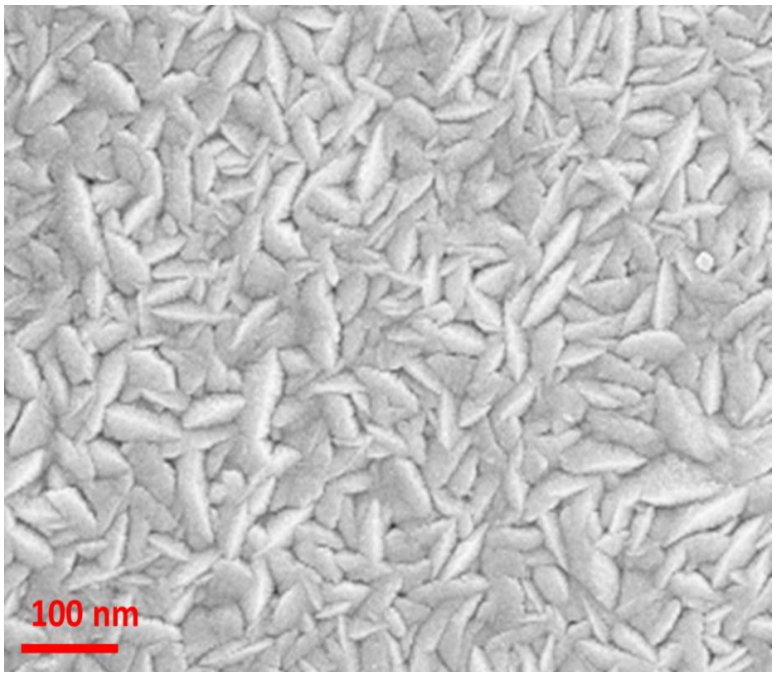

Fig-5.2: FESEM image of the surface of pristine HfO_2 films deposited by RF magnetron sputtering at 120W deposition power.

The as deposited HfO_2 films on Si sample were studied by the GIXRD measurements and the results are shown in Fig-5.3. The films deposited on Si substrate were scanned over 20º to 80º of 2θ and grazing angle was kept at 4º. The peaks in the diffraction patterns of pristine samples centered at 2θ values of 24.16º, 24.66º, 28.32º and 34.30º which correspond to the (011), (011), (111) and (020) crystal planes, respectively. These crystal planes were assigned to the monoclinic phase of HfO_2 by matching with the standard JCPDS file [PDF# 00-006-0318]

having space group of $P2_1/c$. The crystallite size has been calculated by using Scherrer's formula [37] as given below.

$$d = \frac{0.9\lambda}{\beta\cos\theta} \tag{5.1}$$

where 'λ' is the wavelength of X-rays (1.54 Å), 'β' is full width at half maximum, 'θ' is Bragg angle. From the above Scherrer's formula the calculated grain size was around 62 nm.

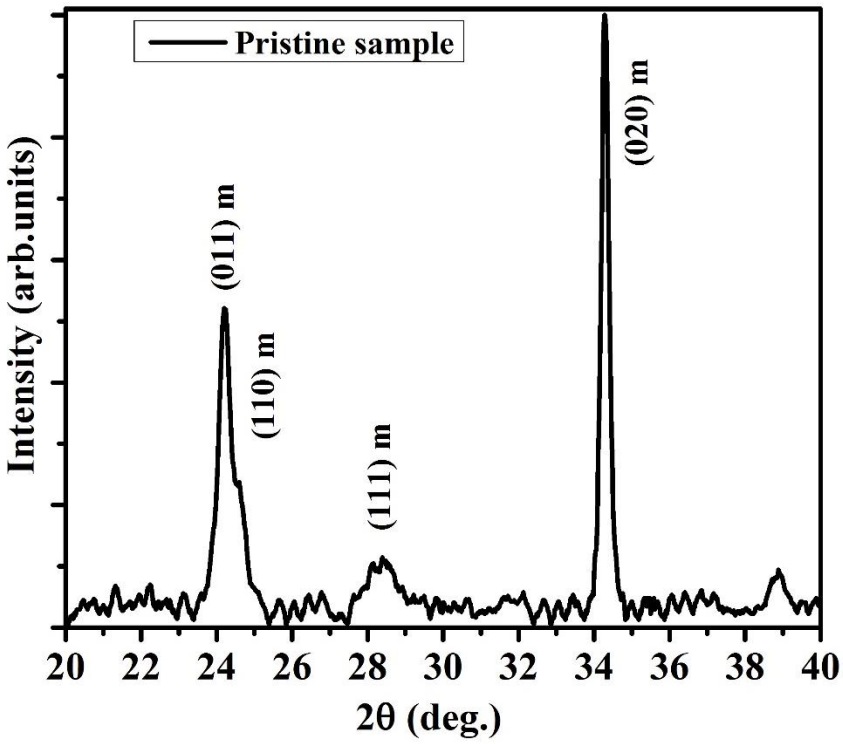

Fig-5.3: GIXRD pattern of pristine HfO_2 film deposited on Si substrates.

The PL measurements were performed on pristine and irradiated samples to monitor the dynamics of defect states as a function of fluence. The excitation wavelength was 350 nm. The HfO_2 bandgap is around 5.7 eV, which is much higher than the excitation energy 3.55 eV. Hence the observed PL from the HfO_2 is attributed to the transition from mid-bandgap states or defect states within the excitation energy range. The PL spectra of pristine sample is shown in Fig-5.4. The pristine sample has shown a dominant peak at 377 nm (3.3 eV), and a broad peak from 400 nm to 550 nm in visible region. After deconvolution using peak fitting program, the broad peak yields the new peaks at 2.93 eV and 2.5 eV. Most of the literature suggests that PL originates from the Oxygen-related interstitial and/or vacancy defects in HfO_2 [38].

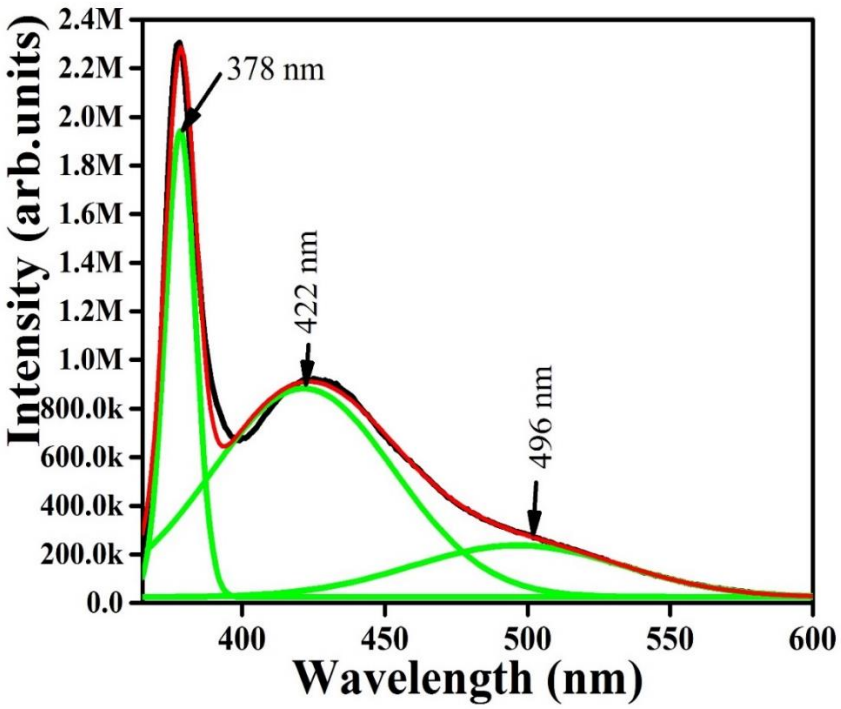

Fig-5.4: PL spectra of pristine HfO_2 film (curves obtained by deconvolution).

5.3.2 SHI induced phase transformation and grain fragmentation:

a) Surface morphology and grain fragmentation

After SHI irradiation at different ion fluences, the film surface morphology and grain size change completely as shown in Fig-5.5 (a-d). Upon irradiation with a fluence of 3×10^{12} ions/cm^2, the large flake structured grains started destabilizing without any change in flake structure and average flake size was around 60 nm along its long axis. Further, an increase of fluence to 1×10^{13} ions/cm^2, the evolution of new grains started within the flack structure. The destabilization of grains was slightly higher compared to the previous fluence. At this fluence, the grain size was around 35 nm. On further increasing the fluence to 3×10^{13} ions/cm ^{2}, the flake structure was destroyed completely and the formation of individual sphere like grains of size 25-30 nm started. At highest fluence of 1×10^{14} ions/cm^2, the surface is further smoothened with uniform average grain size of 15 nm. The grain size variation with ion fluence is summarized in Table-5.1 and Fig-5.5. The main reason behind the change of grain size and morphology can be understood in terms of the phenomena of ion induced grain fragmentation within the film. There are some reports in the literature on ion induced grain fragmentation in fluoride thin films [39, 40]. The strained nano-grains or nano-flakes are expected to be relaxed during SHI irradiation to promote grain fragmentation process and phase transitions in films.

Hence the ion-induced electronic energy loss within the film plays a major role in observed grain fragmentation and morphological changes.

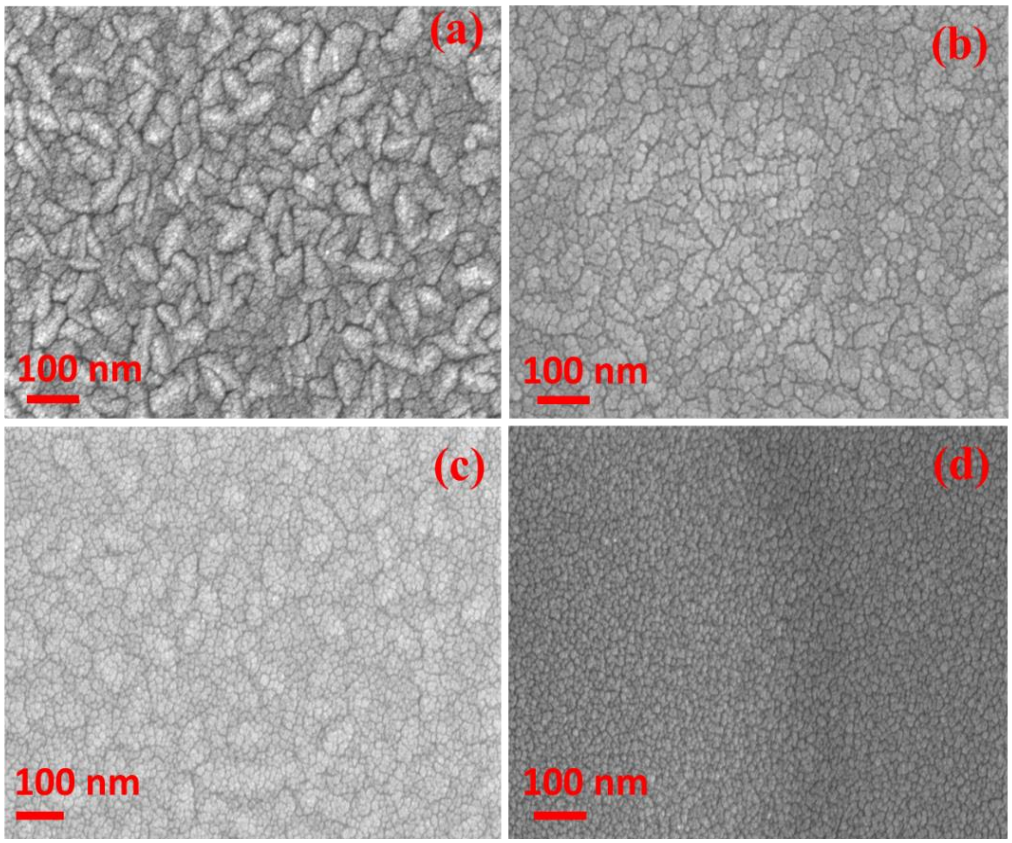

Fig-5.5: FESEM images of HfO_2 films as a function of fluence: a) 3×10^{12} ions/cm^2, b) 1×10^{13} ions/cm^2, c) 3×10^{13} ions/cm^2 and d) 1×10^{14} ions/cm^2.

b) Phase transformations and crystallinity:

Pristine and 100 MeV Ag ion irradiated HfO_2 films were studied by GIXRD measurement and the results are shown in Fig-5.6. GIXRD measurement details are described in the above section. After SHI irradiation the evaluated grain sizes calculated using equation-5.1 and the grain sizes tabulated in the below Table-5.2 are plotted in Fig-5.7. Along with the decrease in grain size, a fractional phase change was observed after irradiation of these samples with 100 MeV Ag^{7+} ion. The new peak located at $2\theta=30.04^o$ in irradiated samples corresponds to the tetragonal phase of the crystal plane (101) as per the standard JCPDS file [PDF# 06-0318]. The intensity of this tetragonal peak is found to increase with increase in the ion fluence. The tetragonal phase was not observed for pristine or even for low dose samples (up to an ion fluence of 3×10^{12} ions/cm^2). This phase change was significant for the ion fluences 1×10^{13}, 3×10^{13} and 1×10^{14} ions/cm^2.

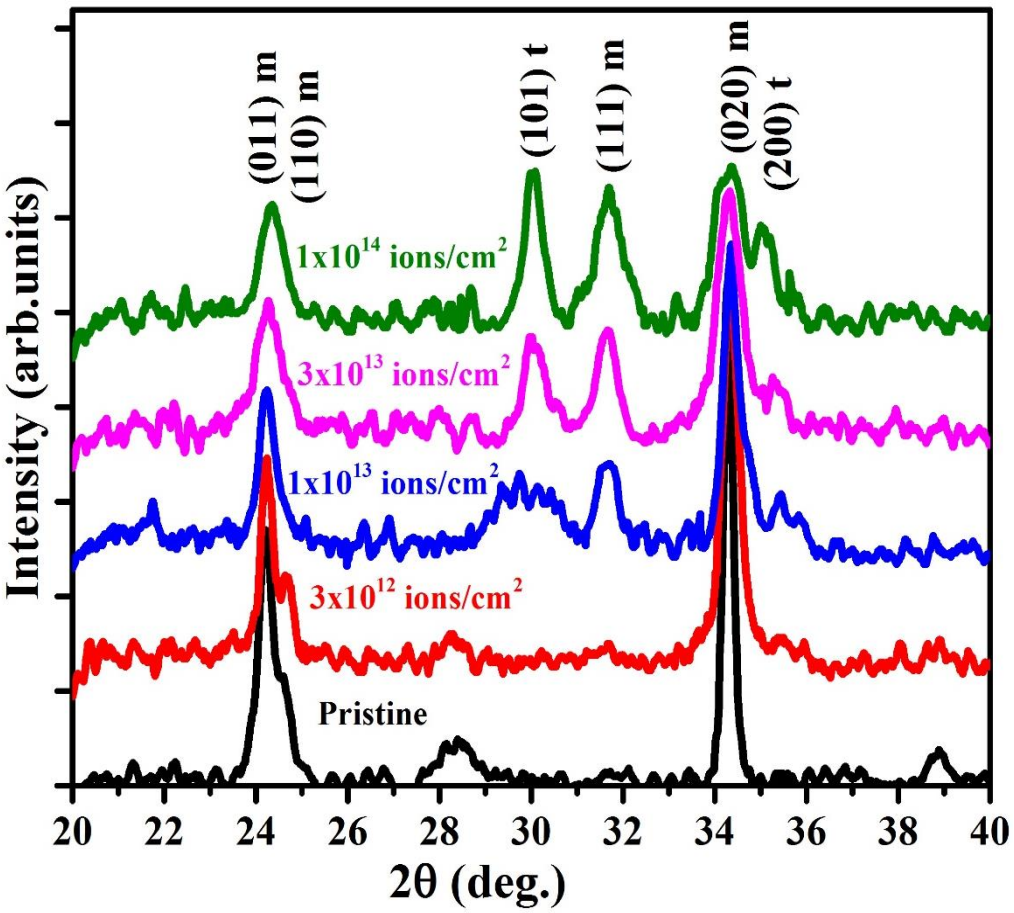

Fig-5.6: GIXRD patterns of both pristine and irradiated HfO_2 films deposited on Si substrates (Each graph is labeled with corresponding fluence).

Table-5.2: Sample name, ion fluence, grain sizes estimated by various methods.

Sample Name	**Irradiation Fluence (ions/cm^2)**	**Particle / Grain Size (nm) estimated by**	
		GIXRD	**FESEM**
HfO_2/Si-1	Pristine	62 nm	70 nm
HfO_2/Si-2	3 x 10^{12}	48 nm	60 nm
HfO_2/Si-3	1 x 10^{13}	32 nm	35 nm
HfO_2/Si-4	3 x 10^{13}	22 nm	26 nm
HfO_2/Si-5	3 x 10^{14}	14 nm	15 nm

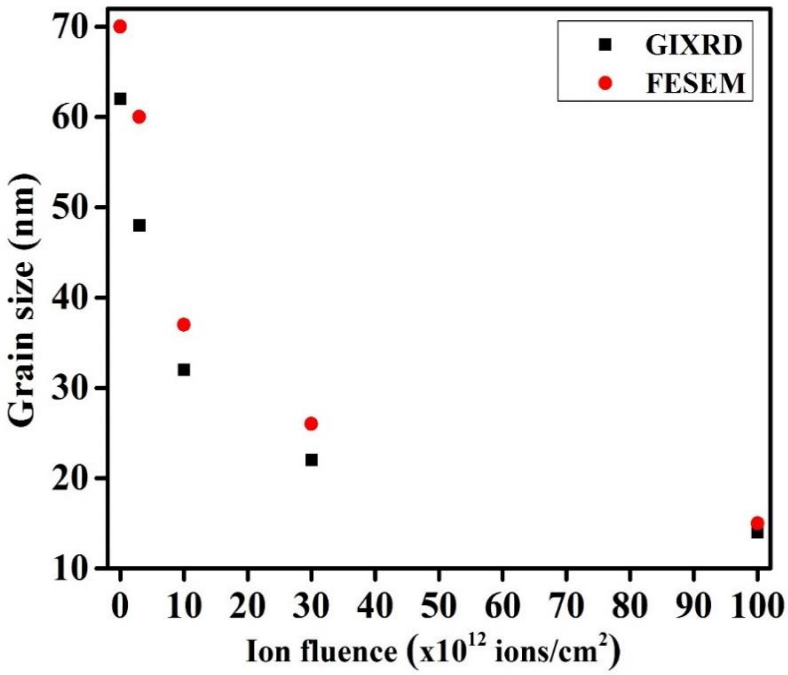

Fig-5.7: Grain size estimated by GIXRD and FESEM measurements.

A new tetragonal peak corresponding to (200) planes emerged at 2θ = 35.09º for highest fluence. The fraction of phase change is calculated using Garvie and Nichilson [41] equation given by

$$C_t = \frac{I_t(101)}{I_m(011) + I_t(101) + I_m(020)} \quad (5.2)$$

where 'C_t' is the compositional weight of tetragonal phase, 'I_m', 'I_t' are integral areas of the monoclinic and tetragonal phases (or intensities of corresponding peaks). C_m (= 1 - C_t) gives the monoclinic compositional weight. The calculated fractional tetragonal phase with ion fluence is shown in Fig-5.8. The maximum tetragonal phase of 35 % was attained for the ion fluence of 1×10^{14} ions/cm^2. SHI induced crystalline to crystalline phase transitions were earlier observed in bulk ZrO_2 and HfO_2 [29, 42-44]. Monoclinic to tetragonal transition was induced in ZrO_2 and HfO_2 by 595 MeV Xe and 295 MeV I ion irradiations, respectively. These results are consistent with the present 100 MeV Ag ion irradiation induced phase transitions in 500 nm HfO_2 films deposited by RF magnetron sputtering.

Along with the evolution of tetragonal phase, the intensity of dominant monoclinic phase peaks (for (011) and (020) in pristine sample) decreased with the increase in ion fluence. An increase in the width of these peaks is also observed. Initially, the grain size was 62 nm which further decreased to 15 nm with increase in ion fluence.

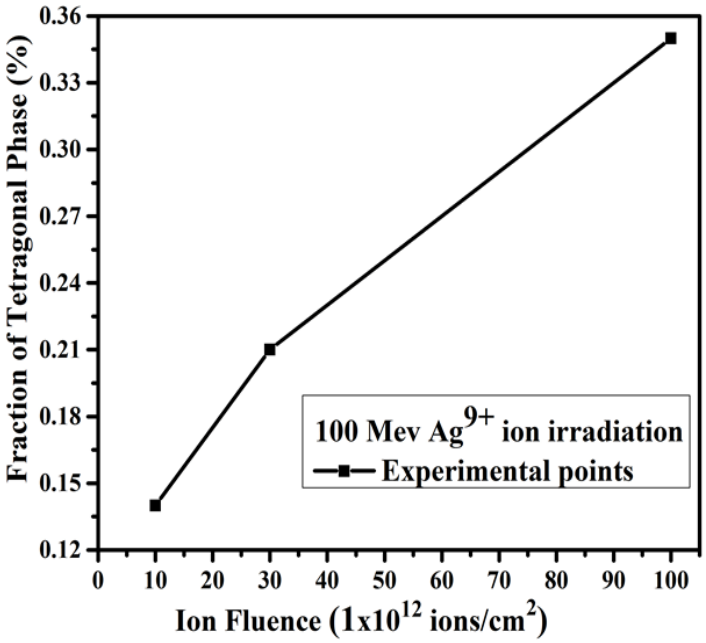

Fig-5.8: Fraction of tetragonal phase with respect to monoclinic phase as a function ion fluence in HfO_2 films.

The decrease in grain size, decrease in peak area and increase in peak width with ion fluence may be attributed to the ion induced grain fragmentation process. Similar results have been observed in other thin films by various groups [39, 40] and an appropriate method was proposed to estimate the corresponding track radius by GIXRD analysis. To determine the track radius from the GIXRD data, peaks were normalized and averaged with the dominant peak for the pristine sample. The obtained values were fitted using exponential Poisson's equation as given below [40] to determine the damage cross-sections along different crystallographic directions.

$$A(\text{ø}t) = (1-S_a) \times \exp(-\sigma_a \times \text{ø}t) + S_a \quad (5.3)$$

where $A(\text{ø}t)$ is normalized area of the concerned peak at given fluence, S_a is the saturated normalized area at highest fluence, σ_a is the damage cross-section along the corresponding crystallographic direction. The increase in intensity appears to be linear at lower fluences with slope I_a of the fitting being equal to $-\sigma_a \times (1-S_a)$. From this slope, we can deduce the information of track radius ($\sigma_a = \pi \times r^2$). The initial slopes of the corresponding peaks are -21.1 (020), and -36.27 (011), followed by damage cross sections as 43.7 (020) and 75 (011) nm^2. The corresponding track radii deduced from peak areas were 3.7 nm along (020) direction and 4.9 nm along (011) direction. The damage cross-section and track diameters are found to be different along different crystallographic directions which can result in and uneven thermal

expansion leading to the observed grain fragmentation. The fitted exponential Poisson's graph is shown in Fig-5.9.

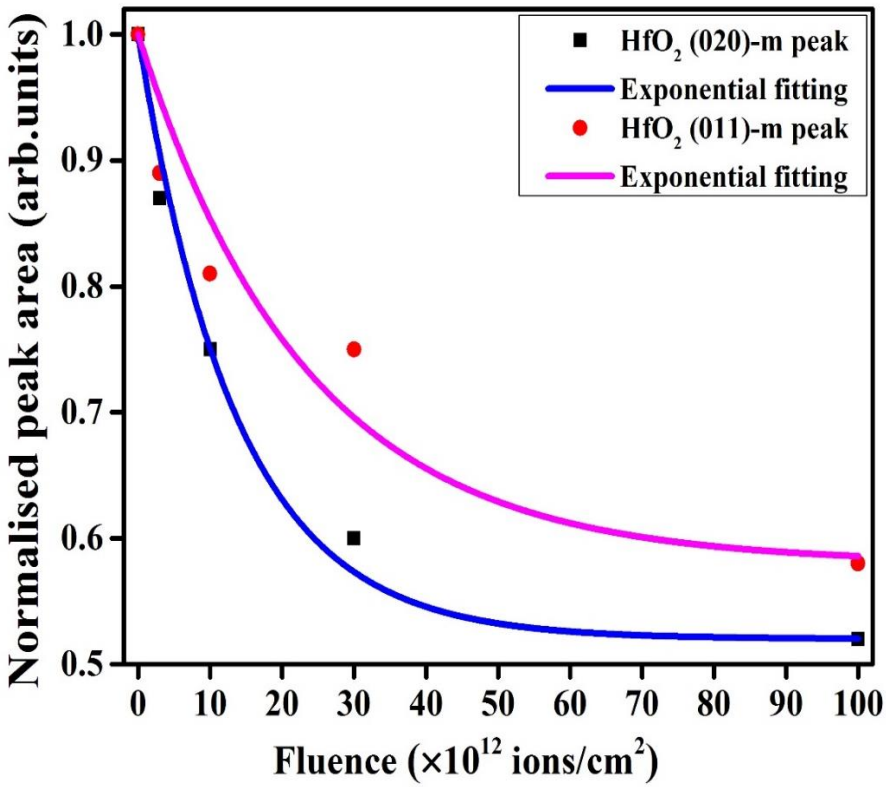

Fig-5.9: Normalized peak areas of dominant peaks with respect of pristine sample as a function of ion fluence.

Consequently, the width of the diffraction peak increases with the decrease of the peak area. The widths of the normalized peaks are averaged with the pristine sample and fitted with the Poisson's exponential fitting and are given by [40]

$$W(øt) = S_w (1\text{-}\exp(-\sigma_w \times øt)) + 1 \quad (5.4)$$

Where W(øt) is normalized peak width at a given fluence, S_w is the saturated normalized width at highest fluence and σ_w is the damage cross-section. The initial slope I_w of the fitting is equal to the $\sigma_w \times S_w$. From this slope, we can deduce the information about track radius ($\sigma_a = \pi \times r^2$). The initial slopes of the corresponding peaks are 30.5 (020), 33.5 (011) and followed by damage cross sections as 17.9 (020), 22.3 (011) nm^2. The corresponding track radii deduced from peak widths were 2.4 nm along (020) direction and 2.7 nm along (011) direction. The fitted exponential Poisson's graph is shown in Fig-5.10. From the two fittings, the extracted track radii by these two methods are in agreement with each other. Overall the estimated average track radii are in the range of 5-7 nm.

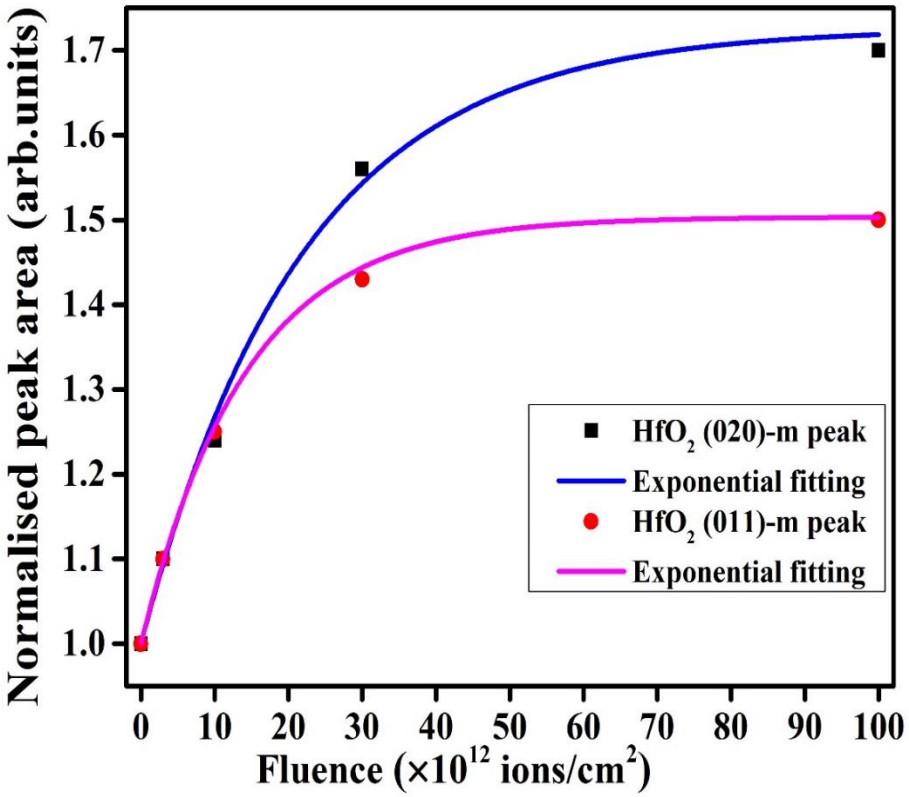

Fig-5.10: Normalized peak widths of dominant peaks with respect of pristine sample as a function of ion fluence.

c) Ion induced reconfiguration and annihilation of defects:

The PL spectra of SHI-irradiated samples are shown in Fig-5.11. Under the influence of SHI irradiation, the sharp dominant peak at 377 nm disappears completely for all the fluences, and only the broad peak remains intact. The single neutral oxygen vacancy can be distributed over the bandgap, but maxima are localized at 377 nm (3.3 eV) [38]. Rui Tao Wen et al. [45] reported that peaks at 2.71 eV and 2.94 eV belong to the positively charged Oxygen vacancy states of Vo^{2+} and Vo^{+}. Owing to ion irradiation, the neutral oxygen vacancies are suppressed completely. All of these defects depend on the deposition parameters. In general, the defects can be expected in suboxide formation (HfO_x, $x<2$) which is consistent with our RBS analysis. Approximately, the broad peak position is same for all irradiated samples except for minor increase in intensity. The shift in the PL emission band to the higher wavelength side believed to be due to change in the stress/ strain in the HfO_2 films, is generated from the change in the crystal phase from monoclinic to tetragonal [46, 47]. After deconvolution using peak fitting program, each peak is clearly seen to be a combination of 3.0 eV, 2.9 eV, and 2.6 eV as shown Fig-5.11 (a-d). In our recent reports, we noticed the similar kind of results in thin (~ 10 nm) HfO_2 films [28, 32]. Most of these shallow and deep level emissions in HfO_2 may be attributed to oxygen-related intrinsic defect states in between the conduction and valence band states or F-centers [48]. When the material transforms from one phase to another phase, some

of the defects may disappear while other types of defects remain intact due to inevitable changes in the strains during these phase transitions. 2.7 eV blue luminescence has been reported by various research groups in HfO_2 and this defect state slightly shifted to 2.6 to 2.8 eV upon irradiation [49]. The 3.1 eV defect peak might be associated with the charged Oxygen defect state [50]. The change in defect configurations indicates the changes in the strain due to SHI irradiation which is consistent with the observed grain fragmentation and phase transformations in these films. The schematic representation of the defect states and their tentative assignments are shown in Fig-5.12 and Table-5.3, where B1, B2, B3 and B4 are radiative transitions from the excited level to the defect states [51].

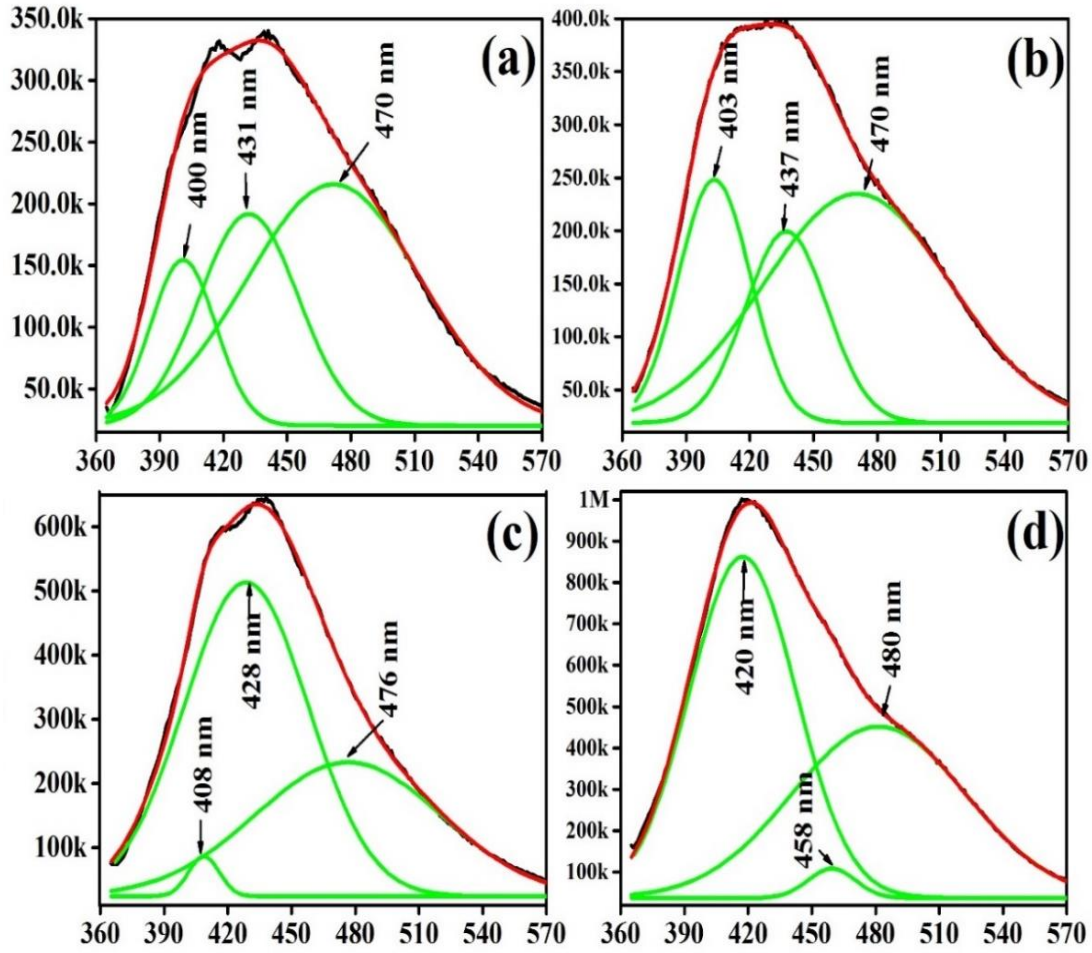

Fig-5.11: PL spectra of HfO_2 thick films: a) 3×10^{12} ions/cm^2, b) 1×10^{13} ions/cm^2, c) 3×10^{13} ions/cm^2, d) 1×10^{14} ions/cm^2. (X-Axis indicates the wavelength (nm), Y-Axis indicates the intensity (arb. Units)) (curves obtained by deconvolution are also shown).

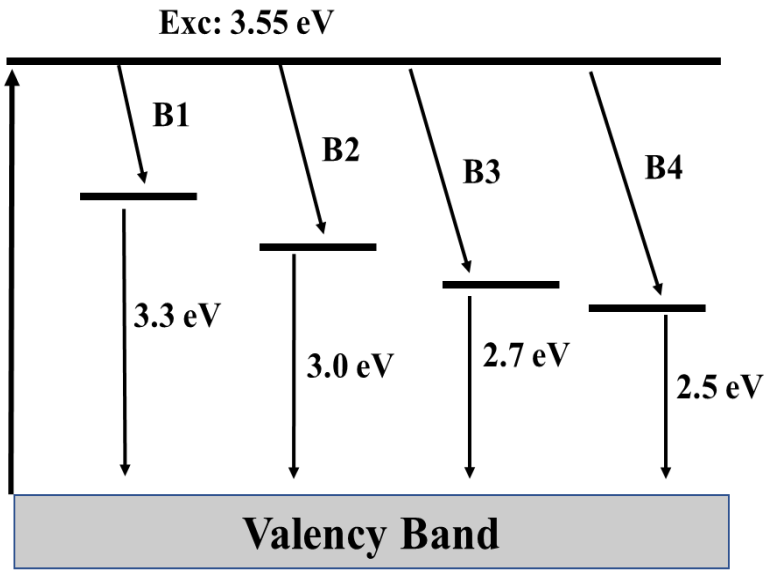

Fig-5.12: Schematic diagram of light emission form the defects states of the HfO_2 films.

Table-5.3: Observed emission wavelengths and tentative assignment of emission peaks.

S. No	Sample Name	Composition	Observed PL peak position (nm)	Tentative Defect Assignment	Reference used for assignments
1	HfO_2/Si-1	$Hf_{0.27}O_{0.73}$	378 (~ 3.3 eV) 422 (2.9 eV) 496 (2.5 eV)	Vo Vo^+ --	[45, 46, 47, 48]
2	HfO_2/Si-2	Un known	400 (3.1 eV) 431 (2.9 eV) 470 (2.6 eV)	-- Vo^+ --	
3	HfO_2/Si-3	Un known	403 (3.1 eV) 437 (2.8 eV) 470 (2.6 eV)	-- -- --	
4	HfO_2/Si-4	Un known	408 (3.0 eV) 428 (2.9 eV) 476 (2.6 eV)	-- Vo^+ --	
5	HfO_2/Si-5	Un known	420 (2.9 eV) 458 (2.7 eV) 480 (2.6 eV)	Vo^+ Vo^{2+} --	

5.3.3 Thermal spike model and discussions:

There are few reports on ion induced amorphous to crystalline, crystalline to amorphous and crystalline to crystalline transformations in ZrO_2 and HfO_2 [28, 29, 43, 44]. ZrO_2 and HfO_2 are twin oxides and both exhibit almost similar properties. The monoclinic phase of HfO_2 can exist from room temperature to 1700 ºC, whereas in the case of ZrO_2 it is from room temperature to 1100 ºC. The tetragonal phase of HfO_2 is stable from 1700 ºC to 2500 ºC whereas for ZrO_2 it is around 1100 ºC to 2200 ºC respectively. With further increase in temperature, both twin oxides transform to cubic phase. While transforming from monoclinic to tetragonal phase, there is a change in volume fraction of HfO_2 by 3.5 % [52]. However, compared to ZrO_2 (7.5 %) it is very small [52]. The volume expansion coefficient is different for different crystallographic directions for HfO_2 which can cause the observed grain fragmentation during SHI irradiation. Associated with uneven thermal expansion in HfO_2 nano-grains, one can expect the grain fragmentation. In another context, The rapid increase of temperature leads to the thermal shock wave in the film. The thermal shock wave creates enough pressure to cripple the nano-grains and leads to the grain fragmentation.

The newly formed grain size purely depends on the thermal contraction rate and strain relaxation in large grains. The rapid phase transformation is also responsible for the grain fragmentation. This anomaly can be observed in multiphase ceramics like HfO_2, ZrO_2, AlO_3 [53]. The grain fragmentation mainly depends on the initial grain size and strain generated within the grains [54, 55]. In this process, the grain size reduces to a critical size after strain relaxation. In the other context, the bulk free energy per unit volume (G_b) in m-HfO_2 is lowest and in the case of tetragonal-HfO_2 it is highest. The surface free energy per unit volume (γ) for t-HfO_2 is lowest and in the case of monoclinic-HfO_2, it is highest [56]. When the phase transition takes place between the two stable phases (m to t) the grain size decreases to a stabilized minimum grain size [56]. Along with that there are few models explaining the grain fragmentation [57, 58].

The electronic energy loss of 23.2 keV/nm is deposited within the HfO_2 film under 100 MeV Ag ion irradiation. This huge amount of deposited energy can bring the material to the melting temperatures within the fraction of picosecond timescales in a confined area. The calculated atomic temperature as a function of radial distance at a given time [37] is shown in Fig-5.13. The phase transformation of material happens when the temperature reaches the phase transition temperature. According to thermal spike calculations, the track radii is around 5-7

nm which indicates the rise of temperature is equal to the tetragonal phase transformation temperature. The rise of temperature in the damaged cross-section area and calculated track radius are compatible with each other. In the process, thermal gradient induced shock wave pressure cripples the strained nano-grains or nano-flakes. The observed phase changes, grain fragmentation, defects creation or annihilation are inter-dependent under certain critical conditions. Hence several manifestations of SHI irradiation are observed in this work.

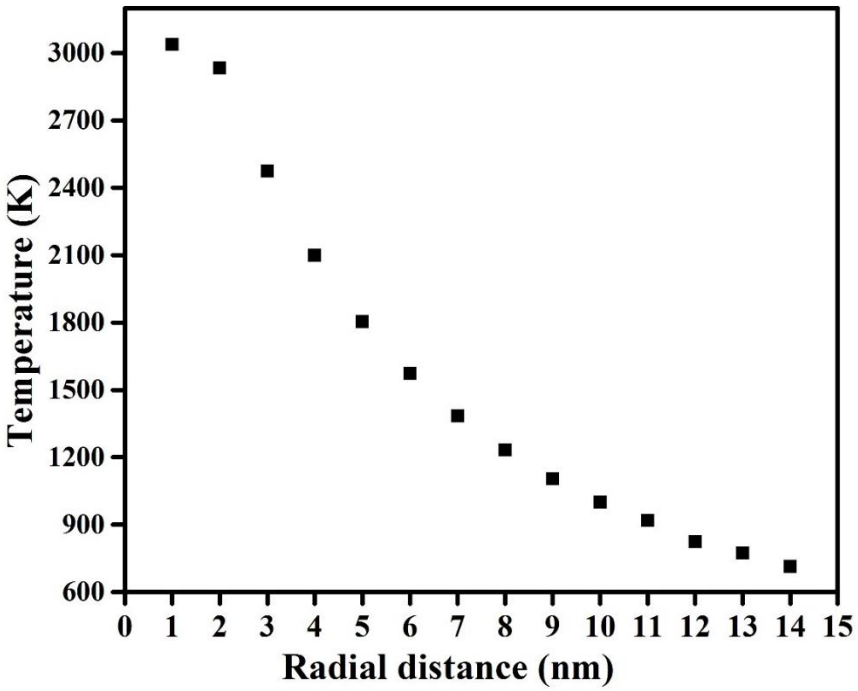

Fig-5.13: Evolution of lattice temperature with respect to radial distance from ion path in HfO_2 films estimated by thermal spike model.

5.4 Conclusions

Films of Hafnium oxide were deposited on Si substrates by RF magnetron sputtering method at high RF power (120 W). The thickness of the as-grown films was around 500 nm and they exhibit monoclinic phase. The obtained self-oriented nano-flake structures are attributed to high deposition rates and film growth conditions. After 100 MeV SHI irradiation, phase transformation, grain fragmentation and defect annihilation have been observed as a function of ion fluence. Ion induced track radius is calculated within the films by studying the changes in peak areas and peak widths of various peaks observed in the GIXRD patterns. The average track radii are estimated to be 3-4.5 nm and the corresponding calculated atomic temperatures reached the critical value for tetragonal phase transformation temperature. FESEM data confirms the ion induced grain fragmentation. PL emission at 377 nm, broad emission at 420

nm indicate the shallow oxygen defects and F-centers present in the as-grown hafnium oxide films. After irradiation, the sharp peak at 377 nm disappears completely. Ion-induced heat desorption and anisotropic thermal expansion in the nano-grains are expected to cause the observed grain fragmentation. Electronic energy loss induced sharp rise of thermal gradient is the most likely cause of the phase transformation in the film. Ion-induced defect annihilation, strain relaxation and defragmentation are found to be interdependent phenomenon.

5.5 References

1. Eva Zarkadoula, Marcel Toulemonde, and William J. Weber, *Appl. Phys. Lett.* **107**, 261902 (2015).
2. M. Toulemonde, C. Dufour and E. Paumier, *Acta Physica Polonica A,* **109,** 311-322 (2006).
3. M. C. Ridgway, R. Giulian, D. J. Sprouster, P. Kluth, L. L. Araujo, D. J. Llewellyn, and A. P. Byrne, *Phy. Rev. Lett.* **106**, 095505 (2011).
4. Saif Ahmed Khan, D K Avasthi, and Sonu Hooda, *Appl. Phys. A*, **124**, 2-9 (2018).
5. H Amekura, S Mohapatra, U B Singh, S A Khan, P K Kulriya, N Ishikawa, N Okubo and D K Avasthi, Nanotechnology 25, 435301 (2014).
6. Udai B. Singh, Dinesh C. Agarwal, Saif A. Khan, Satyabrata Mohapatra, Ambuj Tripathi, Devesh K. Avasthi, *J. Phys. D: Appl. Phys.***45,** 445304 (2012).
7. N. Srinivasa Rao, A.P. Pathak, N. Sathish, G. Devaraju, S.A. Khan, K. Saravanan, B.K. Panigrahi, K.G.M. Nair, D.K. Avasthi, Nuclear Instruments and Methods in Physics Research B 268 (2010) 1741–1743.
8. G.S. Virdi, B.C. Pathak, D.K. Avasthi, D. Kanjilal, Nucl. Instr. and Meth. in *Phys. Res.* B **187,** 189–200 (2002).
9. G. Szenes, *Phys. Rev.* B **5,1** 8026 (1995).
10. N.C. Mishra, *Rad. Eff. Def. Solids*. **166,** 657–665 (2011).
11. M.K. Sharma, Aloke Kanjilal, Matthias Voelskow, D. Kanjilal, Ratnamala Chatterjee, *Nucl. Instr. Meth. Phys. Res. B,* **268,** 1631–1636 (2010).
12. S. K. Singh, R. Singhal, R. Vishnoi, V. V. S. Kumar and P. K. Kulariya, *Indian J. Phys.* **91**, 547-554 (2017).
13. A. Biswas, R. Gupta, and N. Kumar, D. K. Avasthi and J. P. Singh, S. Lotha, D. Fink, S. N. Paul and S. K. Bose, *Appl. Phys. Lett.* **78**, 4136 (2001).
14. Kiran Jeet, V. K. Jindal, L. M. Bharadwaj, D. K. Avasthi, and Keya Dharamvir, J. *Appl. Phys.* **108**, 034302 (2010).

15. Subodh K. Gautam, Abdelhak Chettah, R.G. Singh, Sunil Ojha, Fouran Singh, *Nucl. Instr. Meth. Phys. Res. B* **379,** 224–229 (2016).
16. J. Larkin, R. Henley, D. C. Bell, T. Cohen-Karni, J. K. Rosenstein, and M. Wanunu, *ACS Nano* **7,** 10121 **(**2013).
17. Justin J F and Jankowiak A, *J. Aerosp. Lab* **3,** 1–11 (2011).
18. Simonenko E P, Sevast'yanov D V, Simonenko N P, Sevast'yanov V G and Kuznetsov N T, *Russ. J. Inorg. Chem.* **58,** 1669–93 (2013).
19. M. Lee, N. Zine, A. Baraket, M. Zabala, F. Campabadal, R. Caruso, M. G. Trivella, N. J. Renaulta, and A. Errachid, *Sens. Actuator B-Chem.* **175**, 201-207 (2012).
20. L. Maggiorella, G. Barouch, C. Devaux, A. Pottier, E. Deutsch, J. Bourhis, E. Borghi, and L. Levy, *Future Oncol.* **8(9),** 1167–1181 (2012).
21. C. Wiemer, L. Lamagna, S. Baldovino, M. Perego, S. Schamm-Chardon, P. E. Coulon, O. Salicio, G. Congedo, S. Spiga and M. Fanciulli, *Appl. Phys. Lett*. **96**, 182901 (2010).
22. J. Niinistö, K. Kukli, M. Heikkila, M. Ritala, and M. Leskela, *Adv. Eng. Mater*. **11**, 223-234 (2009).
23. C. Wiemer, L. Lamagna, S. Baldovino, M. Perego, S. Schamm-Chardon, P. E. Coulon, O. Salicio, G. Congedo, S. Spiga and M. Fanciulli, *Appl. Phys. Lett.* **96**, 18290 (2010).
24. V. Pervak, F. Krausz, A. Apolonski, *Thin Solid Films* **515,** 7984-7989 (2007).
25. J.D. Traylor Kruschwitz, W.T. Pawlewicz, *Appl. Opt*. **36,** 2157-2159 (1997).
26. Tingting Tan, Zhengtang Liu, Hongcheng Lu, Wenting Liu, Hao Tian, *Opt. Mat.* **32,** 432-435 (2010).
27. S K Singh, R Singhal, R Vishnoi, V V S Kumar and P K Kulariya, *Indian. J. Phys.* **91**, 547–554 (2017).
28. M. Dhanunjaya, S.A. Khan, A. P. Pathak, D.K. Avasthi and S. V. S. Nageswara Rao, *J. Phys. D: Appl. Phys.* **50,** 505301, (2017).
29. A. Benyagoub, *Phys. Rev.* B **72,** 094114 (2005).
30. J. F. Ziegler, "SRIM-2003". *Nucl. Instr. Meth. B.* **1027**, 219-220 (2004).
31. M. Mayer, SIMNRA: Simulation of RBS, ERD and NRA Spectra. <http://www.rzg.mpg.de/mam/>
32. N. Manikanthababu, M. Dhanunjaya, S.V.S. Nageswara Rao, A.P. Pathak, *Nucl. Instr. Meth. Phys. Res. B* **379**, 230–234 (2016).
33. N. Manikanthababu, N. Arun, M. Dhanunjaya, S.V.S. Nageswara Rao & A. P. Pathak, *Radiation Effects & Defects in Solids*, **171**, 77–86 (2016).

34. M. Dhanunjaya, N. Manikanthababu, A. P. Pathak, and S. V. S. Nageswara Rao, AIP Conference Proceedings **1731**, 080071 (2016).
35. A.M. Hofe, J. Schlacher, J. Keckes, J. Winkler, and C. Mitterer, *Vacuum.* **99,** 149-152 (2014).
36. Xinyi Dai, Aijun Zhou, Lidong Feng, Ying Wang, Jin Xu, Jingze Li, *Thin Solid Films* **567,** 64–71 (2014).
37. P. Scherrer, *Göttinger Nachrichten Gesell.*, **2**, 98 (1918).
38. T. V. Perevalov, V. Sh. Aliev, V. A. Gritsenko, A. A. Saraev, V. V. Kaichev, *Microelectronic Engineering* **109,** 21–23 (2013).
39. Manvendra Kumar, Ratnesh K. Pandey, Parasmani Rajput, S.A. Khan, Fouran Singh, D.K. Avasthi, Avinash C. Pandey, *J. Alloy and Comp.* **695,** 83-90 (2017).
40. M. Toulemonde, A. Benyagoub, C. Trautmann, N. Khalfaoui, M. Boccanfuso, C. Dufour, F. Gourbilleau, J. J. Grob, J. P. Stoquert, J. M. Costantini, F. Haas, E. Jacquet, K. O. Voss, and A. Meftah, *Phy. Rev. Lett*. **85**, 054112 (2012).
41. R. C. Garvie and P. S. Nicholson, *J. Am. Ceram. Soc*. **55**, 303-305 (1972).
42. H.S. Lokesha, K.R. Nagabhushana, Fouran Singh, *J. Alloy and Comp.* **647,** 921-926 (2015).
43. H.S. Lokesha, K.R. Nagabhushana, Fouran Singh, *Nucl. Instr. Meth. Phys. Res. B* **379,** 131-135 (2016).
44. A. Benyagoub, *Eur. Phys. J*. B **34,** 395–398 (2003).
45. Rui-Tao Wen, Lai-Sen Wang, Hui-Zhang Guo, Yuanzhi Chen, Guang-Hui Yue, Dong-Liang Peng,Takehiko Hihara, Kenji Sumiyama, *Materials Chemistry and Physics*, **130**, 823–826 (2011).
46. Manvendra Kumar, Ratnesh K. Pandey, Parasmani Rajput, S. A. Khan, Udai B. Singh, D. K. Avasthi and Avinash C. Pandey, *Phys. Chem. Chem. Phys.* **19**, 23229 (2017).
47. L. Kumari, W.Z. Li, J.M. Xu, R.M. Leblanc, D.Z. Wang, Y. Li, H. Guo, J. Zhang, *Cryst. Growth Des.* **9**, 3874–3880 (2009).
48. D. R. Islamov, V. A. Gritsenko, T. V. Perevalov, *ECS Trans.* **69**, 197-203, (2015).
49. Vladimir A. Gritsenko 1, Timofey V. Perevalov 1, Damir R. Islamov, *Phys. Rep.* **613,** 1–20 (2016).
50. T. V. Perevalov, D. V. Gulyaev, V. S. Aliev, K. S. Zhuravlev, V. A. Gritsenko, and A. P. Yelisseyev, *J. Appl. Phys.* **116,** 244109 (2014).
51. Ran Jiang, Xianghao Du, Weideng Sun, Zuyin Han & Zhengran Wu, *Scientific Reports* **5**, 15574 (2015).

52. Curtis. C. E L, M. Doney, and J. R. Johnson, *J. Amer. Ceram. Soc.* **37,** 458-465 (1954).
53. Coppola, J. A. and R. C. Bradt, *J. Amer. Ceram. Soc.* **56,** 214-218 (1991).
54. Siebeneck, H. J, D. P. H. Hasselman, J. J. Cleveland and R. C. Bradt. *J. Amer. Ceram. Soc.* **58,** 241-244 (1976).
55. Kirchner, H. P. and R. M. Gruver. *J. Amer. Ceram. Soc.* **53,** 232-236 (1970).
56. R. Materlik, C. Künneth, A. Kersch, *J. Appl. Phys.*, **117**, 134109 (2015).
57. C. David, E. Nicolas, and Emilien Azéma, *Comp. and Geotech.*, **67**, 150–156 (2015).
58. J. A. Astrom, and H.J. Herrmann, *Eur. Phys. J.* B **5**, 551–554 (1998).

SHI Assisted Fabrication of Embedded Nanoparticles (Si and Ag) in HfO_2 Matrix and Laser Ablated HfO_2 Nanoparticles

The main aim of this chapter is to fabricate the metal (Ag) and semiconductor (Si) Nanoparticles (NPs) embedded in Hafnium Oxide (HfO_2) thin films. For that, silicon co-deposited HfO_2 films were prepared by Radio Frequency (RF) magnetron sputtering method. HfO_2 and Silver (Ag) multilayer thin films were prepared using electron beam (e-beam) evaporation system. 100 MeV Ag ion irradiation was performed on these films to get the embedded NPs within the HfO_2 matrix. Grazing Incident X-Ray Diffraction (GIXRD), Transmission Electron Microscope (TEM), Ultra Violet -Visible (UV-Vis), and Photo Luminescence (PL) measurements were employed to characterization. In both cases, NPs (Si and Ag) are formed within the HfO_2 matrix with the assistance of 100 MeV Ag ion. The Surface Plasmon Resonance (SPR) peak position is affected by the surrounding matrix. The observed luminescence attributed to the emission from Si nanoparticles and defect states present in the HfO_2 matrix. The calculated particle sizes from TEM and GIXRD were in agreement with each other. In addition to that, pure HfO_2 NPs were prepared by employing the laser ablation method. Different size and phase of the HfO_2 NPs were observed by impinging the different laser energies. These results provide the useful information of understanding of ion and laser interaction with nanomaterials.

6.1 Introduction

Hafnium oxide is a well-known high-k dielectric material that has replaced the Silicon Dioxide as gate oxide material in metal oxide semiconductors (MOS) in Integrated Circuit (IC) technology [1] with a promise to scale down as per Moore's law [2]. HfO_2 with high dielectric constant (~25), better compatibility and band-offset values with Silicon has made HfO_2 to replace the SiO_2 in MOS devices and attain its significance in memory applications [3]. Along with that, HfO_2 Nanoparticles (NPs) have been employed as flash memory [4], charge trapping layer in metal oxide semiconductors [5, 6] etc.

Simultaneously, there is a growing interest in nanoparticles embedded in a dielectric matrix. Especially NPs that are embedded in HfO_2 matrix for the optical and electronic applications. Metal and semiconductors NPs embedded in the dielectric matrix have proven their importance in floating gate memories [7], plasmonic [8], high-density solar cell [9] and light-emitting diodes [10] applications. The use of non-volatile memory devices with embedded NPs offer the fast read and write operations at small operating voltages compared to conventional flash memories [11] and polarization memories [12]. Noble metal NPs (Au, Ag, Pt, and Ni, etc.) embedded in HfO_2 matrices for memory, biomedical, optical and plasmonic applications have been studied extensively [13-18]. The optical properties of noble metal nanoparticles lead to many uses in sensing and imaging technologies [19, 20]. Tiwari et al. [21] reported a study on Si based semiconductor NPs embedded in HfO_2 matrix for memory application. HfO_2 films doped with Si exhibit ferroelectric behavior and depending on doping concentration there is a transformation from ferroelectric to anti-ferroelectric phase [22]. Si-doped HfO_2 nanoscale devices have been used as CMOS compatible Ferroelectric Field Effect Transistors (FeFETs) [23]. Different groups have studied the importance of Si-doped HfO_2 with respect to their applications [24-26]. Along with HfO_2 matrix, Si nanocrystals embedded in other materials like SiC [27], SiN [28], SiO_2 [29, 30] have also been reported in the literature. Researchers have also reported the Si NPs fabricated by ion implantation and MeV ion irradiation [31-34]. However, still, there is uncertainty in fabrication, usage, and performance of embedded NPs in oxide matrix like HfO_2. Here we report a study on the effects of swift heavy ion irradiation on the structural and optical properties of Si and Ag NPs embedded in HfO_2 matrix.

As mentioned earlier that HfO_2 NPs have wide-ranging applications in various fields including biomedical applications. Recent studies show that the inert behavior of HfO_2 NPs makes them suitable candidates for cancer therapy [35], nanocrystalline HfO_2 based biosensors [36], HfO_2

nanowire-based Ion-Sensitive Feld Effect Transistor (ISFT) for pH sensors [37], X-ray contrast agent and mid-IR biosensor [38] applications. Recently, there have been reports where Gamma and X-Ray radiations were used to treat cancer with HfO_2 NPs since these are better in absorbing the high-energy radiation and in targeting cancer by localizing the radiation damage within the tumor tissues [39].

The material scientists and physicists have adopted several synthesis methods to fabricate the HfO_2 NPs. The cubic HfO_2 NPs were prepared by microwave-assisted reduction and oxidation methods [40]. Monoclinic hafnia NPs were prepared by annealing the ALD grown hafnia thin films [41]. HfO_2 nanorods were prepared by injection method [42]. Radio Frequency (RF) magnetron sputtering method [43], chemical route method [44] and nanosecond (ns) laser ablation techniques have also been employed [45, 46]. Laser ablation method is one of the versatile techniques to synthesize the materials in the nanoscale region in a liquid environment. Using laser ablation with femtosecond (fs) pulses, one can change the material in bulk to nanomaterial by evaporation, sublimation and condensation processes. Further, one can tune the materials properties like particle size, phase and shape by varying the pulse energy, wavelength and repetition rate. In the literature, several reports demonstrate the efficacy of synthesizing NPs by fs laser ablation method [47-53]. To the best of our knowledge, there are no reports on the fabrication of HfO_2 NPs using fs laser ablation though there are few reports on NPs obtained using ns laser ablation. In an earlier report HfO_2 NPs were prepared by ns laser ablation of pure Hf target in different liquid environments and the obtained NPs size varied from 4.3 nm to 5.3 nm in different liquid environments [45]. They observed that the produced hafnia NPs were in the monoclinic low temperature phase and in the tetragonal and fcc high temperature phases.

Herein, we report the fabrication of SHI assisted Si NPs embedded in HfO_2 matrix, SHI assisted Ag NPs embedded in HfO_2 matrix and HfO_2 NPs and nanoribbons (NRs) using fs ablation from bulk HfO_2 in de-ionized water (DIW).

6.2 Experimental details

The main aim of this chapter is to fabricate the semiconductor and metal NPs that are embedded in HfO_2 matrix by different possible ways and secondly, to fabricate the HfO_2 NPs by laser ablation method. In this connection we have deposited HfO_2 thin films, "HfO_2 and Si" co-sputtered thin films, "HfO_2 and Ag" multilayer thin films to fabricate the embedded NPs in HfO_2. Pure HfO_2 films and Si: HfO_2 composite thin films were deposited using RF magnetron

sputtering method which is available in house. Ag: HfO_2 multilayer thin films were deposited using electron-beam (e-beam) evaporation method at IUAC, New Delhi. All these films were deposited on Boron doped p-type Si (100) substrates, 1×1 cm^2 quartz substrates and 200 mesh Carbon coated Copper TEM grids of their respective studies. Si and quartz substrates were cleaned ultrasonically in acetone, ethanol and methanol followed by deionized water to remove the organic and inorganic contaminants and finally dried in nitrogen gas to remove the water residues. TEM grids are placed on the glass slide and the edges of the TEM grids covered with the thin glass cover slip. Each of the cover slip stuck with high-vacuum grid with double sided tape such a way that TEM grids should not fall down during deposition. Specific details of each set of films are explained in the following subsections:

6.2.1 HfSiOx composite thin film:

Initially, HfO_2 thin films, and "Si and HfO_2" co-sputtered thin films were fabricated using RF magnetron sputtering method. These pure HfO_2 thin films and nanocomposite thin-films were deposited on TEM grids, Quartz and Si substrates. 99.99% pure, 2-inch diameter and 3 mm thick commercially purchased HfO_2 target was used for depositing the films. The pre-cleaned substrates and TEM grids were clamped to the substrate holder and were loaded into the sputtering chamber. A turbo-molecular pump backed by a rotary pump was used to achieve the base pressure of 8×10^{-6} mbarr for each of the deposition. Ar (99.99 % pure) gas was introduced into the sputtering chamber for depositing the films. A 60 W of RF (13.5 MHz) power was used to deposit the films. In the first experiment, pure HfO_2 thin films were deposited for 10 min on TEM grid and Si substrate. In the second experiment, about 30 percent of the HfO_2 target was covered using a silicon strip of 5×1.2 cm^2 as shown in Fig-6.1 to deposit the nano-composite films.

Fig-6.1: Schematic diagram showing of 30 % of Si coverage on the HfO_2 target.

The deposition was carried out at room temperature for 10 minutes. While depositing this set of films, substrate rotation was maintained at a uniform rate of 10 rpm, and the substrate to target distance was kept at 12.5 cm. The estimated thickness was 10 nm, and 20 nm respectively for these films.

6.2.2 HfO_2 and Ag multilayer thin films:

Similarly, "Ag, and HfO_2" multilayer thin films were deposited using e-beam evaporation method at IUAC, New Delhi. Before deposition, ultrasonically cleaned Si and Quartz substrates were loaded into the deposition chamber. This e-beam chamber has a facility to deposit layer by layer thin films of different materials. Also, the chamber is equipped with e-beam deposition facility for oxides and the thermal evaporation facility for metals. In our case, HfO_2 films were deposited using e-beam deposition method and Ag films were deposited using thermal evaporation process. HfO_2 pellet was prepared using commercially purchased 99.99 % pure HfO_2 powder. The powder was compressed into 5-mm thick and 1-cm diameter pellet with a pressure of 20 MPa. These pellets were used for HfO_2 deposition. On the other side, pure Ag wire was used to deposit the Ag thin films. Before depositing multilayer films, the chamber was evacuated to a base pressure of 9×10^{-7} mbar. The nominal structure and estimated film thickness of multilayer films is shown in Fig-6.2. Initially HfO_2 thin film of about 15 nm was deposited by applying 25 mA current and 300 V to the e-gun. After reaching the estimated thickness, e-beam deposition was stopped for a while and the Ag deposition was started using thermal evaporation. Ag thin films about 5 nm was deposited over the HfO_2 film by applying the 300 A current and 1V to the thermal evaporation system. These HfO_2 and Ag films were deposited simultaneously one over other in the same manner as per the above-mentioned conditions.

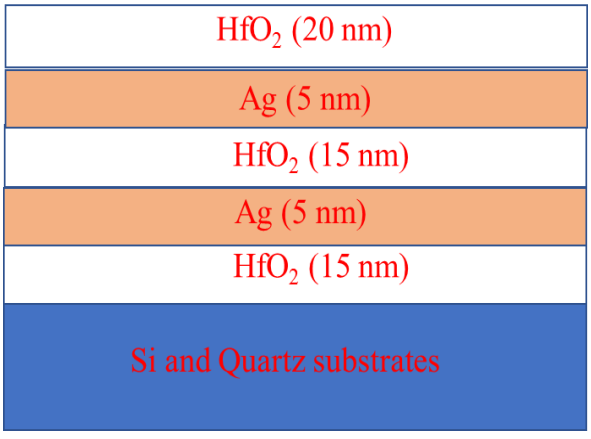

Fig-6.2: Schematic diagram of HfO_2 and Ag films multilayer structure.

HfSiOx and HfO_2: Ag multilayer thin films deposited samples on TEM grids, Si and quartz substrates were irradiated using 100 MeV Ag^{7+} ions using 15 MV Pelletron accelerator facility at IUAC, New Delhi. These SHI irradiations were carried at different fluences. The ion range (7.74 µm), electronic and nuclear energy loss (S_e - 23.2 keV/nm and S_n - 0.15 keV/nm) were estimated using Stopping and Range of Ions in Matter (SRIM-2013) simulation code [54]. The ion beam was scanned over 1×1 cm^2 of the sample area at a constant beam current of 1 particle nano-Ampere (pnA) to minimize possible local heating effects. The irradiation details like sample name, ion fluence and ion energy have been tabulated in Table-6.1.

Table-6.1: Sample type and irradiation details.

S. No	**Sample type**		**Fluence (Ions/cm^2)**	**Ion Energy (MeV)**
	$HfSiO_x$ films	**HfO_2: Ag films**		
1	$HfSiO_x$ -1	H/Ag/H– 1	Pristine	100, Ag^{7+}
2	$HfSiO_x$ -2	H/Ag/H – 2	3×10^{12}	
3	$HfSiO_x$ -3	H/Ag/H – 3	1×10^{13}	
4	$HfSiO_x$ -4	H/Ag/H – 4	3×10^{13}	
5	$HfSiO_x$ -5	H/Ag/H – 5	1×10^{14}	

6.2.3 Fabrication of HfO_2 NPs by laser ablation method:

HfO_2 pellets were prepared using 99.9% pure commercial HfO_2 powder with a grain size of 20-30 µm. The powder was compressed into 5-mm thick and 1-cm diameter pellets under a pressure of 20 MPa and sintered at 500^0 C for three hours. These HfO_2 pellets were submerged in deionized water containing Pyrex cell. The effective height of liquid layer above HfO_2 pellet was maintained at 5 cm during the ablation process. Ablation was performed using a Ti: sapphire laser (LIBRA, Coherent) delivering 800 nm pulses with a duration of ~50 fs and at a repetition rate of 1 kHz. The target was placed normal to the laser beam on a two-dimensional motorized stage (Nano direct). The computer program has been developed in such way that the stage can move in X-Y directions with a velocity of 250 □m/sec [55]. The sample was scanned over 5×5 mm^2 and each line was separated by 100 µm. The same procedure was followed for

different laser energies of 200 µJ, 300 µJ, 400 µJ and 500 µJ. The colloidal HfO_2 NPs were collected in airtight glass bottles. The colloidal NPs were drop casted on carbon-coated Cu TEM grids and silicon substrates and subjected to subsequent wetting at 70° C for 1 hour to remove the moisture.

As-deposited samples, SHI-irradiated samples, and laser ablated colloidal HfO_2 NPs were characterized by available and suitable techniques. Grazing Incident X-Ray Diffraction (GIXRD) was employed to investigate the effects of ion irradiation on the phase and crystallinity of HfO_2 and $HfSiO_x$ thin-films deposited on Si substrates. These measurements were performed using Bruker D8 Advance diffractometer with Cu K_α source ($\lambda = 0.154$ nm) at an incident angle of 4^0. The films deposited on TEM grids were investigated by using a TEM – Technia with electron gun working at 200 kV. Photo Luminescence (PL) measurements were performed using a Fluorolog Fluorescence Spectrometer equipped with a Xenon lamp of 450 W and configured to have a resolution of 0.3 nm. Micro Raman measurements were performed using WITech Alpha 300 spectrometer (Ex: 632 nm).

6.3 Results and Discussion

6.3.1 HfO_2 and Si composite films and SHI irradiation effects:

HfO_2 thin-films and $HfSiO_x$ nanocomposite thin-films deposited on TEM grids have been investigated by TEM analysis. The High Resolution TEM (HR-TEM) image shown in Fig-6.3 confirms the formation of HfO_2 NPs in as-grown pure HfO_2 thin-films. The average size of the NPs is around 5-7 nm, and these HfO_2 NPs are amorphous as per the Selective Area Electron Diffraction (SAED) pattern shown in the inset of Fig-6.3. This result is consistent with results presented in 4^{th} chapter and in our recent report on the synthesis of HfO_2 NPs by RF sputtering [56]. Fig-6.4 depicts the TEM image of as grown HfO_2: Si co-deposited (i.e. $HfSiO_x$ nanocomposite) thin-film. It is evident that the co-deposited HfO_2 and Si have been formed in chain-like structures when deposited on TEM grids. This kind of formation is not observed when pure HfO_2 is deposited in same conditions even on TEM grids. Each bead like grain in the nano-chain is amorphous and has a size of around 10-12 nm. However, the rings in SAED pattern suggests the co-existence of poly crystalline phase in the structures. Each of the nanostructured composites is connected with another nanostructure and forms nano chain-like structures. Energy Dispersive x-ray Spectroscopy (EDS) has confirmed nanocomposite formation of both HfO_2 and Si.

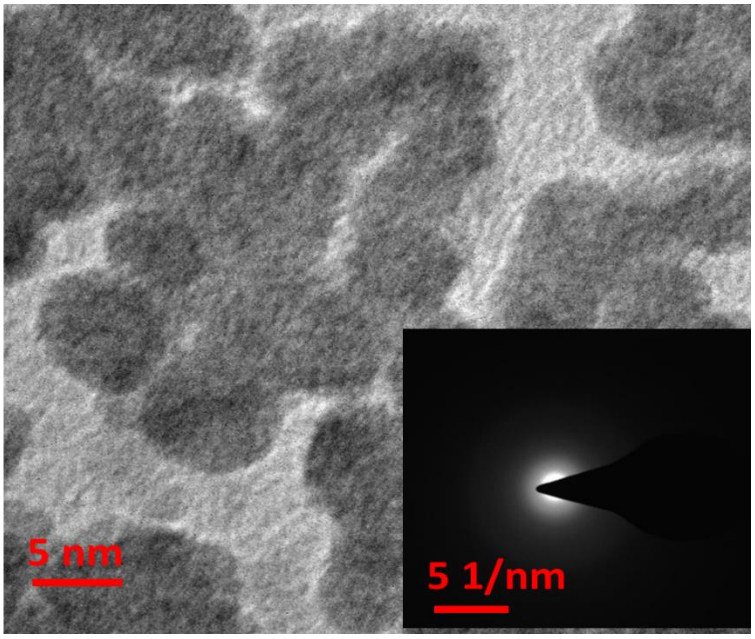

Fig-6.3: HR-TEM image of HfO_2 NPs (inset shows electron diffraction pattern).

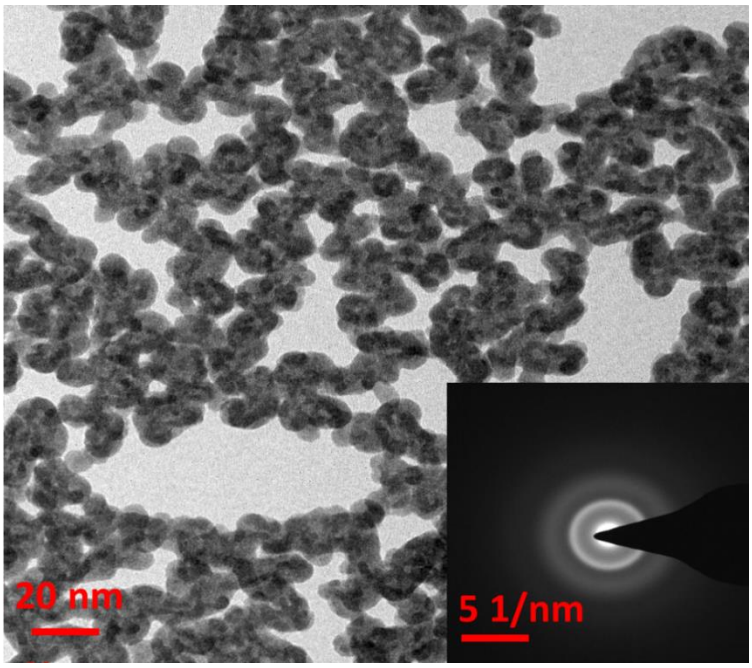

Fig-6.4: TEM image of Si and HfO_2 co-deposited nano-chains (inset shows the electron diffraction pattern).

After 100 MeV Ag ion irradiation, we see different size distribution of Si nanoparticles for different ion fluences within the nano-chains. The HR-TEM images shown in Fig-6.5 confirm the formation of Si NPs. Fig-6.5(a) and 6.5(b) show the image for the fluences of $1x10^{13}$ ions/cm^2 and $3x10^{13}$ ions/cm^2 respectively. During the irradiation, Si NPs got crystallized and HfO_2 phase is changed from amorphous to monoclinic as shown in Fig-6.6. The phase change in HfO_2 is consistent with the results shown in chapter 4 and in our recent report [56]. Fig-

6.6(a) shows the interlunar spacing (d- spacing) of 0.31 nm corresponding to the Si NPs (111) phase wherever the Si NPs are present. The contrast in TEM images indicates the formation of embedded Si NPs with the HfO_2 matrix. It appears in these images as though the Si NPs are surrounded by HfO_2.

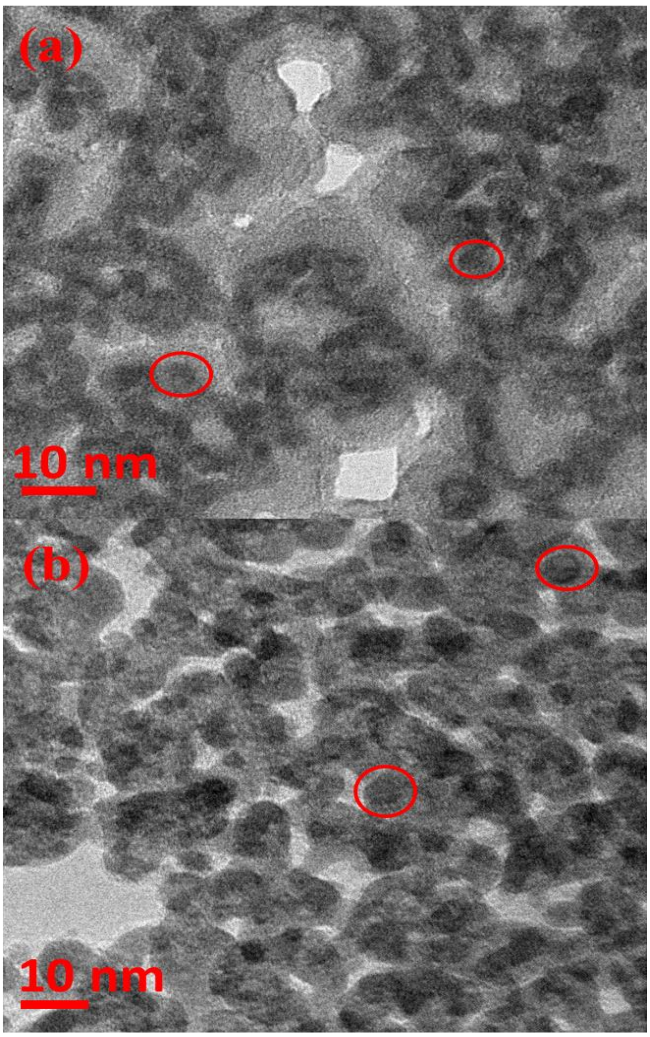

Fig-6.5: HRTEM images of Si and HfO_2 co-deposited thin-films showing nano-chains like structures a) with fluence $1x10^{13}$ ions/cm^2 and b) with fluence $3x10^{13}$ ions/cm^2.

Fig-6.6(b) shows the d spacing of 0.28 nm corresponding to the (-111) of monoclinic phase of HfO_2 wherever the Si NPs not present. The right-side images in Fig-6.6 shows the Inverse Fast Furrier Transform (IFFT) of the corresponding left side images. Fig-6.7(a) and Fig-7(b) show the EDS spectra with and without the Si NPs, respectively which indicate an increase in Si concentration with respect to as deposited samples. The phases of the films and composition of both HfO_2 and Si components in co-sputtered films can be examined by using GIXRD measurement. Even though the film thickness is very small, with grazing incident angle (4^o of θ), we can scan over entire film during the period of scanning.

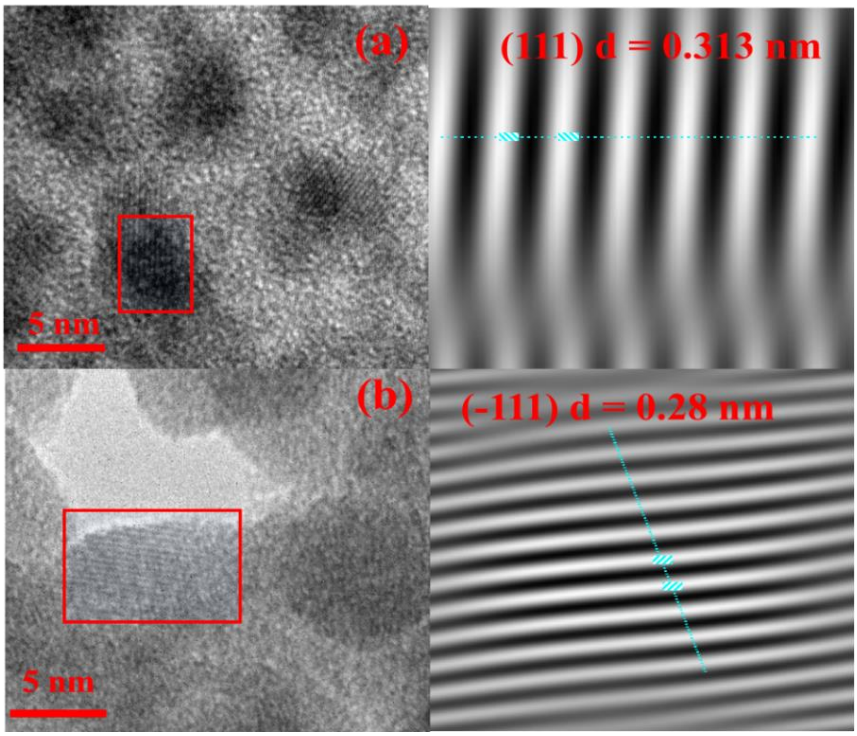

Fig-6.6: HRTEM images on a) at Si NP b) at a HfO_2 portion (Corresponding IFFTs are shown on right side).

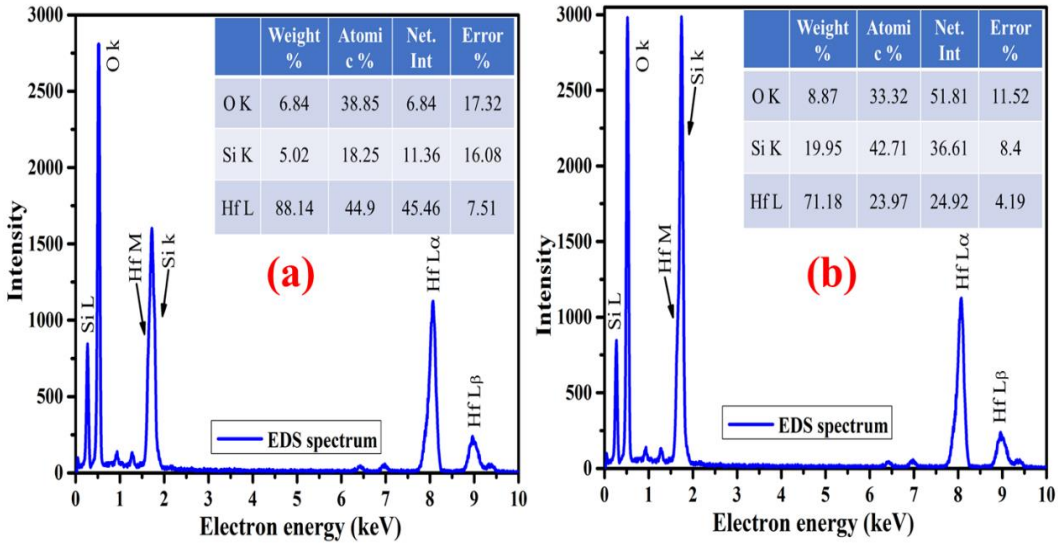

	Weight %	Atomic %	Net. Int	Error %
O K	6.84	38.85	6.84	17.32
Si K	5.02	18.25	11.36	16.08
Hf L	88.14	44.9	45.46	7.51

	Weight %	Atomic %	Net. Int	Error %
O K	8.87	33.32	51.81	11.52
Si K	19.95	42.71	36.61	8.4
Hf L	71.18	23.97	24.92	4.19

Fig-6.7: EDS spectra of films a) away from the area of Si NPs b) within the area of Si NPs.

The GIXRD patterns of co-deposited films on a silicon substrate are shown in Fig-6.8. The pristine sample shows amorphous nature producing no diffraction peaks. These are similar to those films deposited on TEM grids. From the irradiated films, the diffraction peak at 2θ of 31.7º corresponds to the monoclinic phase of HfO_2 (JCPDS- 00-047-1186). This diffraction peak at a 2θ value of 30.4º corresponds to the Si nanoparticles (JCPDS- 00- 040 -0932). The

particle size of both HfO_2 and Si nanoparticles were estimated using Scherrer's formula as given below [57].

$$d = \frac{0.94\lambda}{\beta cos\theta} \tag{6.1}$$

Where λ is the wavelength of X-rays (Cu Kα radiation, λ = 1.5405 Å), β is the full width at half-maximum of the XRD peak, and θ is the Bragg diffraction angle.

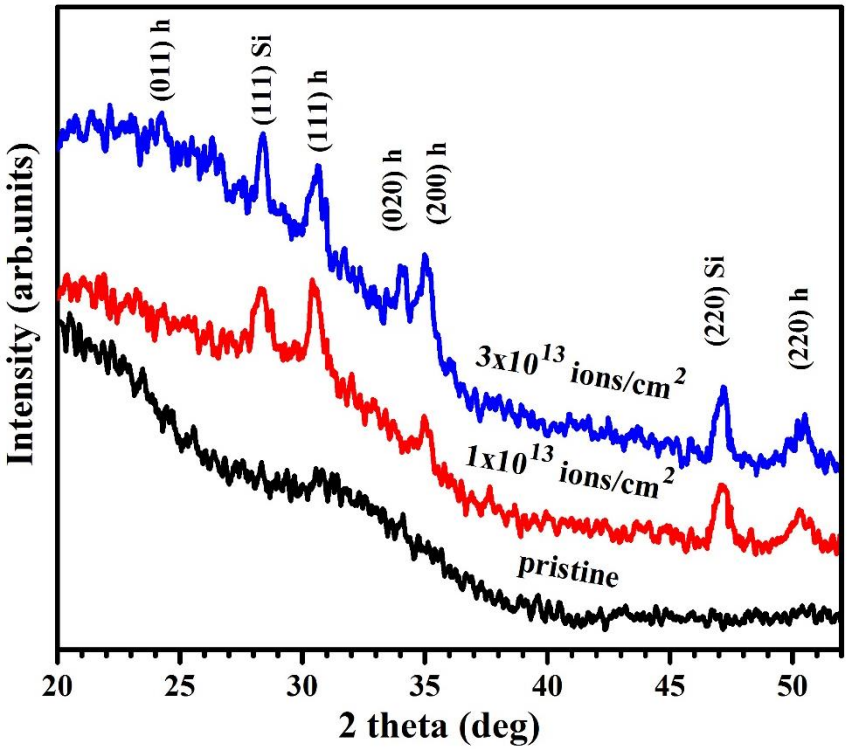

Fig-6.8: GIXRD patterns of pristine and irradiated samples of HfO_2: Si co-deposited on Si substrates.

The estimated particle sizes are shown in Table-6.2. From these results, we see that the Si nanoparticle size strongly depends on the irradiation fluence. Here it is important to note that the HfO_2 particles are elongated whereas the spherical Si NPs are observed within this nanochain like HfO_2 structures. However, the size estimated by this method corresponds to the average size / dimension of particles in the direction of particular planes considered in the calculation.

Table-6.2: Sample name, irradiation fluence and particle sizes.

Sample Name	Fluence (ions/cm^2)	Si particle size (nm)	
		HR-TEM	GIXRD
HfO_2: Si-1	pristine	10-12	--
HfO_2: Si-2	1×10^{13}	5.1	8.2
HfO_2: Si-3	3×10^{13}	8.3	12.1

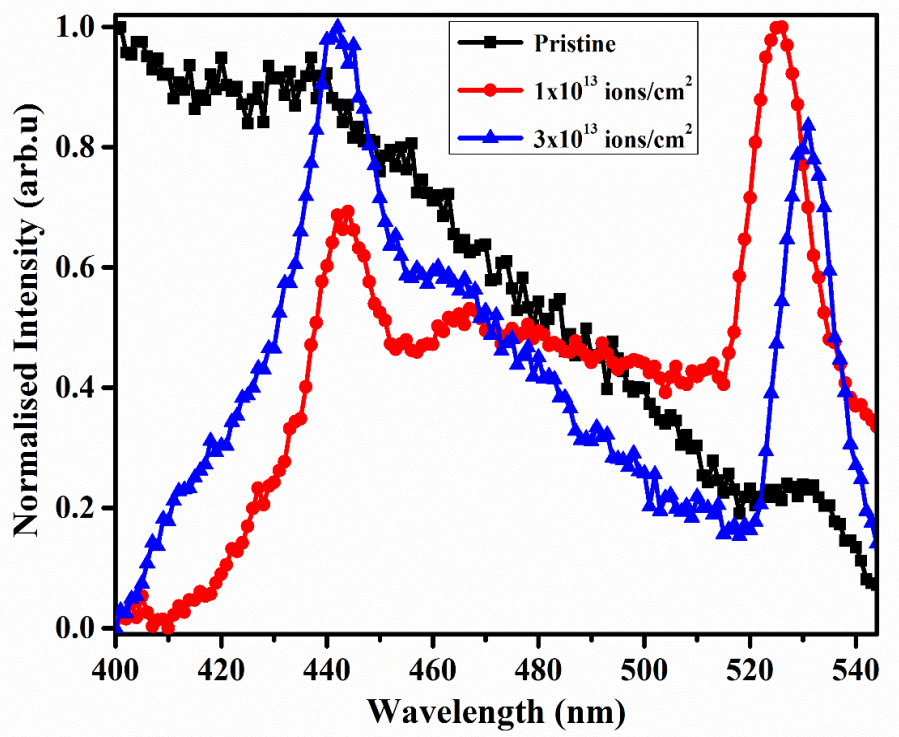

Fig-6.9: PL spectra of HfO_2: Si co-deposited on Si substrates.

PL spectra of Si and HfO_2 co-sputtered films on Si substrates are shown in Fig-6.9. The PL measurements were performed on both the pristine and irradiated films using 350 nm (3.5 eV) excitation wavelength. As deposited sample shows a broad luminescence spectrum over a range of 400 to 500 nm and a small hump at 530 nm giving the information about the presence of Si nanostructures. The broad PL spectrum of HfO_2 is largely characterized by oxygen-related vacancy defects and is consistent with previous reports [58-60]. After irradiation, there are observable luminescence peaks at 445 nm and 530 nm. The luminescence at 445 nm at various fluences correspond to the defects present in the HfO_2. These are middle bandgap electron trap states or F-centers [61-63], which we have discussed in our previous reports [64, 65]. Here the emphasis is on the emission around 530 nm which is expected by the embedded Si NPs within

HfO_2 matrix. It is important to note that the average size of Si NPs is close to the Bohr exciton radius of Si which is around 5.5 nm [66]. Hence the luminescence at 525 nm and 530 nm can be attributed to the Si NPs with respect to the ion fluence of 1×10^{13} and 3×10^{13} ions/cm^2. The emission from isolated Si NPs is mostly in the red to orange (around 700 nm) region. The observed emission at little higher energies confirms the significance of confinement effects caused by core-shell (Si NP / HfO_2) like structures. This further confirms the formation of embedded Si NPs within HfO_2 matrix by SHI irradiation of $HfSiO_x$ nanocomposite films. Further, the observed shift of luminescence to the higher wavelength side (redshift) at higher fluence implies an increase of Si NP size due to ion irradiation. The luminescence at 440 nm belongs to the defects in HfO_2 or surface defects present in the polycrystalline Si NPs [67].

6.3.2 HfO_2 and Ag multilayer films and SHI irradiation effects

HfO_2 and Ag multilayered film were deposited at IUAC, New Delhi and irradiated using 100 MeV Ag ions. The main motivation of this study is to study the evolution of Ag NPs with respect to their size, shape and effects of the surrounding medium during the SHI irradiation. The size and shape of the Ag NPs can be studied by UV-Vis absorption spectroscopy, TEM, and GIXRD. The observations made are as follows: The absorption spectra of HfO_2 and Ag multilayer films are shown in Fig-10(a). A small hump in the absorption spectra at 250 nm is due to HfO_2 and the main absorption peak at 450-500 nm is due to Surface Plasmon Resonance (SPR) of Ag NPs. Normalized SPR peaks of Ag NPs with respect to SHI irradiation are shown in Fig-6.10(b). It is evident that the SPR peak is blue shifted with SHI irradiation. The FWHM of SPR peak decreases with fluence, which means that the Ag NPs size increases with the increase of ion fluence. Pristine sample shows SPR peak at 570 nm with broad peak width. This is expected due to the large sized and irregular Ag clusters while depositing the films. After SHI irradiation, the two layers got overlapped and Ag NPs were formed in the HfO_2 matrix. The SPR peak shifted to lower wavelength side and peak width decreased with ion fluence. The decrease of the peak width and redshift of SPR peak position indicates the growth of the NP size. In metal NPs there are many factors that can influence the SPR position. The shift in the peak position, broadening of the peak and intensity variation may change owing to the changes in the 1) particle size, 2) shape, 3) aspect ratio and 4) material of the surrounding medium [68].

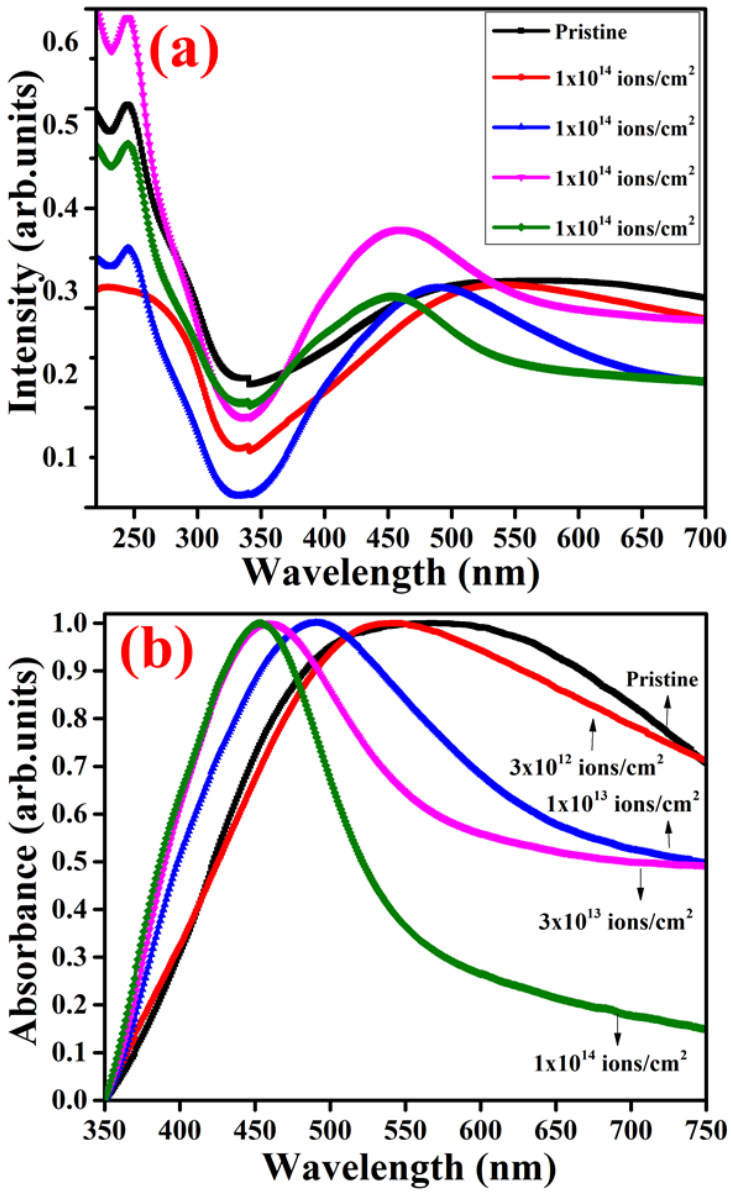

Fig-6.10: a) absorption spectra of HfO_2: Ag multilayer film on quartz substrates and b) normalized absorption spectra.

Above three cases give only slight variation in SPR peak position, but in our case, the SPR blue shift is around 120 nm for highest fluence. Hence, the most probable reason is to do with SHI induced change of dielectric constant of host matrix and possibly also the change of NPs shape and size. If the surface geometry of NPs changes than the resonating electric field density on the surface can change. If the surface density of electrons differs from metal to host matrix, then also such a blue shift is expected [69]. This can be attributed to the change of the dielectric constant of the host matrix during irradiation. There are few reports of SHI induced blue shift of SPR peak even though there is a growth of NPs [70-72]. According to Mie theory, spherical Ag NPs exhibit single SPR peak, while anisotropic particles like prisms, dendrites, triangles

and rod exhibit multi SPR peaks [73]. Since in our case we got only single SPR peak, one can assume that spherical NPs are produced during SHI irradiation.

Bandgap mainly represents the electronic structure of the material. Insulators have a large bandgap, semiconductors have moderate bandgap and metals either have very small bandgap or no bandgap due to the overlap of the valence band and the conduction band. Due to the strong interaction of metal NPs with the incident light, the free electrons oscillate resonantly at

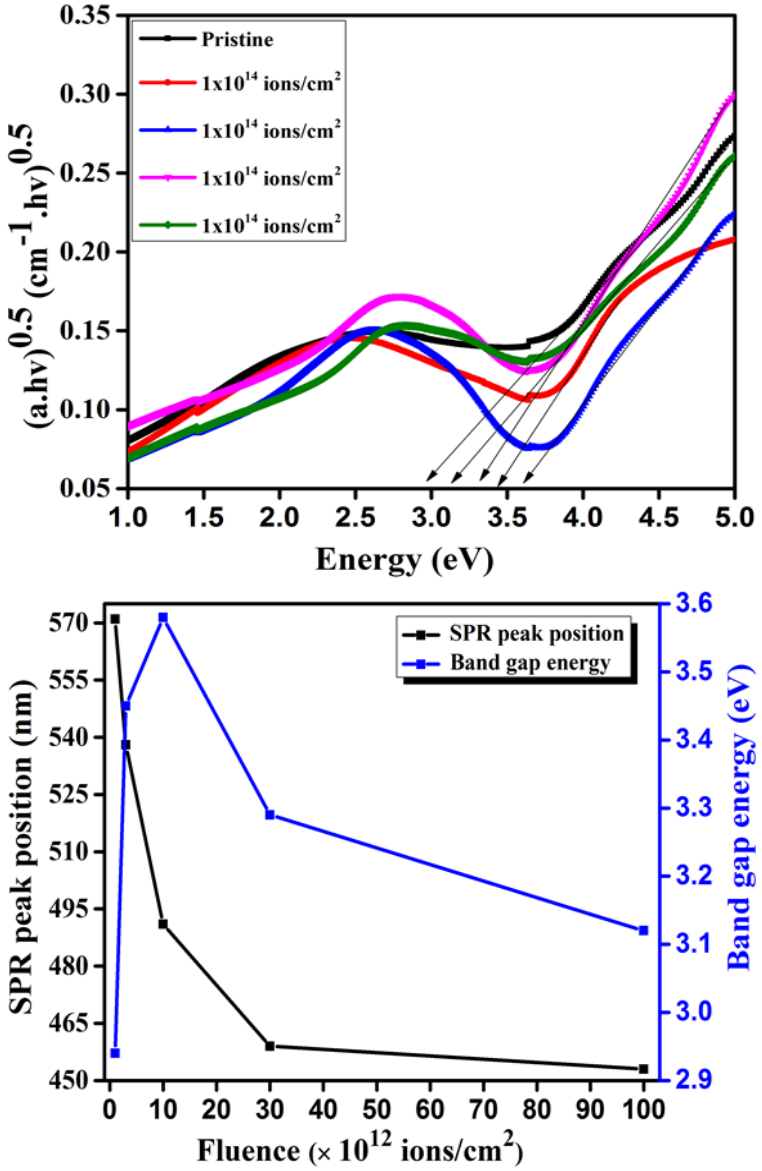

Fig-6.11: a) Bandgap calculation using Tauc's relation and b) SPR peak position and bandgap value in terms of ion fluence.

Particular incident light wavelengths. The oscillating electrons virtually create a gap between the core electrons. Kubelka–Munk [74, 75] proposed a model of exhibiting bandgap in metal

NPs especially with those exhibiting SPR. The optical band gap energy for the Ag NPs is calculated using Tauc equation given below

$$(\alpha h\nu) = B^*(h\nu - E_g)^n \quad (6.2)$$

where 'A' is a constant, α is the absorption coefficient, E_g is the band gap, 'h' is the plank's constant, and ν is the frequency. Where n represents the direct (n=2) or indirect (n=0.5) transition. The absorption coefficient is calculated by dividing the thickness with absorbance. The bandgap of the HfO_2 and Ag composite shown in Fig-6.11(a). Fig-6.1,1(b) represent the SPR peak position and obtained bandgap in terms of irradiated fluence. The bandgap of the HfO_2: Ag film increased sharply from 3.1 eV to 3.6 eV and decreased to 3.2 eV with an irradiation fluence.

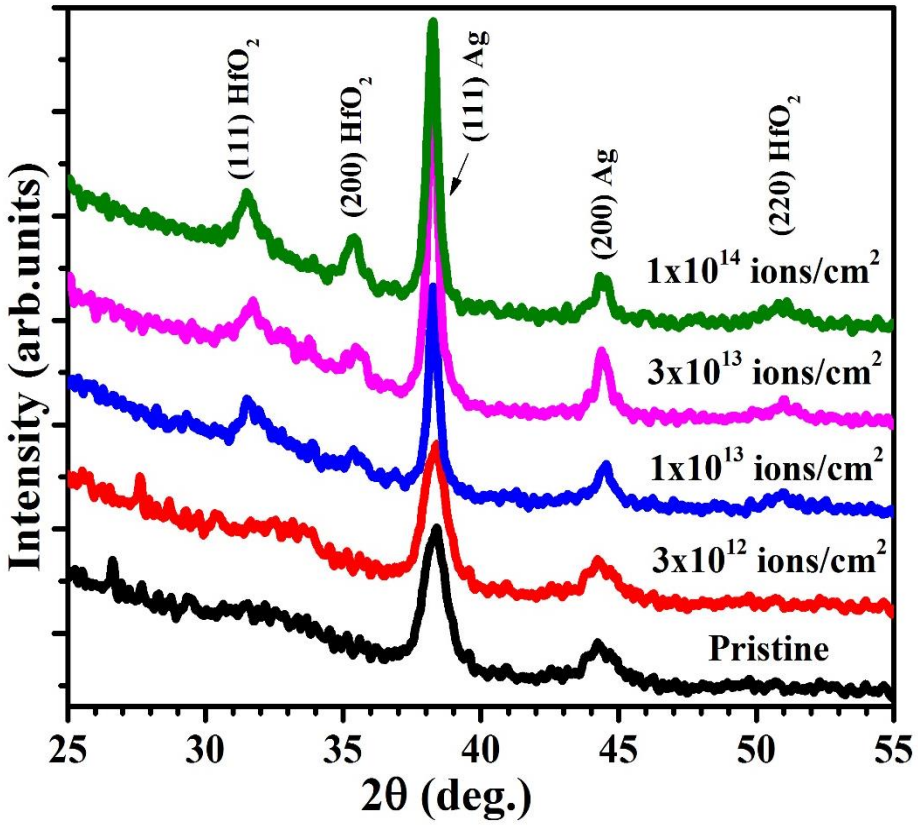

Fig-6.12: GIXRD spectra of Ag and HfO_2 multilayer thin film on Si substrate.

The GIXRD measurements were performed on HfO_2 and Ag multilayered films before and after irradiation shown in Fig-6.12. Before irradiation, HfO_2 is amorphous. After irradiation, both the HfO_2 and Ag show some patterns in GIXRD spectra. The peaks positioned at 2θ value of 31.7º, 35.5º, and 50.4º corresponds to the monoclinic HfO_2. They belong to the (111), (200) and (220) planes respectively. These planes are matching with the JCPDS file no. 00-006-0318. The peaks positioned at 2θ of 38.1 ° and 44.2 ° belong to the (111) and (200) planes of cubic

Ag NPs. These are well matching with the JCPDS file no. is 00-004-0783. Full-width at half maxima of Ag NPs (111) peak is decreasing with the fluence, it indicates that Ag NPs size increases with ion fluence. The grain size of Ag NP is estimated using Scherrer's formula given in Eq-6.1. After irradiation, the Ag nanocluster size increases from 9 nm to 20.6 nm with increase in the ion fluence.

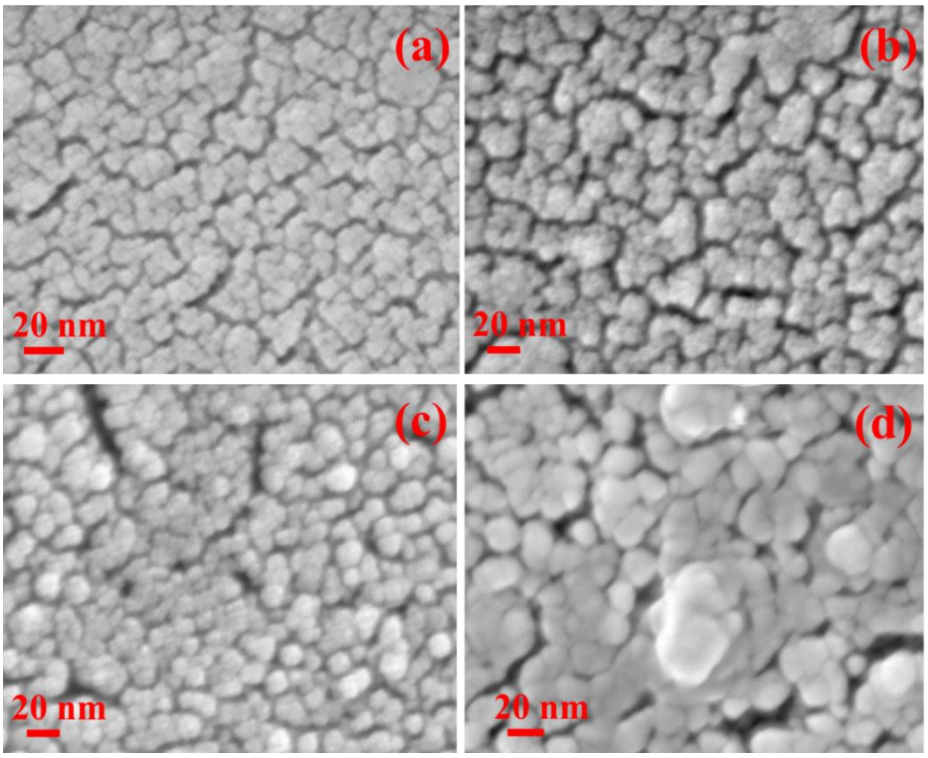

Fig-6.13: FESEM images of HfO_2: Ag multilayer thin films a) as deposited film, b) with fluence 1×10^{13} ions/cm^2, c) with fluence 3×10^{13} ions/cm^2, and d) with fluence 1×10^{14} ions/cm^2.

Fig-6.13 shows the FESEM images of the HfO_2 and Ag multilayer thin films before and after irradiation. Fig-6.13(a) shows the as-deposited film and the rest of the images Fig-6.13(b), 6.13(c), and 6.13(d) correspond to samples irradiated at fluences of at 1×10^{13} ions/cm^2, 3×10^{13} ions/cm^{2,} and 1×10^{14} ions/cm^2 respectively. The pristine sample exhibits the uniform distribution of HFO_2 grains of each size 15 nm. After irradiation, HfO_2 grain size is reduced from 15 nm to 10 nm at different fluences. At highest fluence, $1x10^{14}$ ions/cm^2, the HfO_2 grain size is around 10 nm. The reduction in the grain size due to grain fragmentation or ion induced strain relaxation can be seen in Fig-6.13(b) for the fluence 1×10^{13} ions/cm^2. Ag NPs were formed due to SHI irradiation and some of the NPs got diffused to the surface as shown in Fig-6.13(c) for the fluence 1×10^{13} ions/cm^2. At the highest fluence, 1×10^{14} ions/cm^2, shown in Fig-6.13(d), one can observe the composite like film formation due to coagulation of Ag NPs. The

Ag NP size increases from 7 nm to 15 nm after irradiation. The results are in good agreement qualitatively with the GIXRD data. Ag NPs look like spherical particle at the surface.

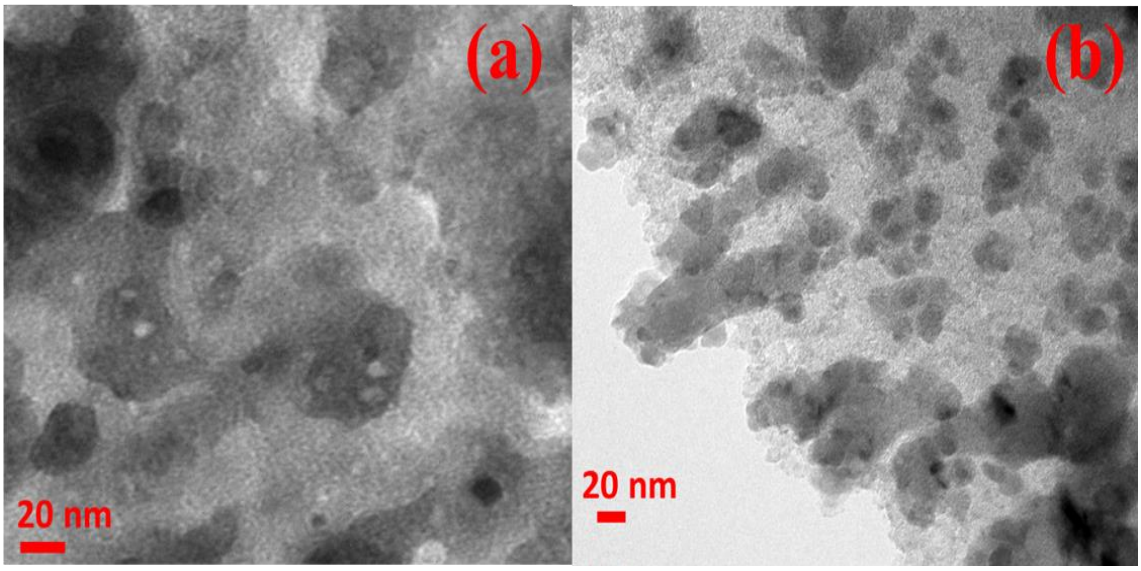

Fig-6.14: TEM images of scratched HfO_2: Ag multilayer thin films a) as deposited film, b) with fluence 1×10^{14} ions/cm^2.

The films on Si substrates are scratched and the drop casted on the TEM grids and examined using TEM. Fig-6.14(a) shows the as-deposited sample and illustrates the large Ag nanoclusters formed under the HfO_2 layers. In some other areas, sheet like structures of the Ag films beneath the HfO_2 film were observed. After irradiation with 100 MeV Ag ion, Ag nanoclusters started the formation of NPs. Fig-6.14(b) shows the TEM image for the fluence of $1x10^{14}$ ions/cm^2, the observed particle size is around 20 nm. The evolved Ag NPs size is in agreement with the GIXRD and FESEM analysis.

6.3.3 HfO_2 NPs by laser ablation method

Fig-3.15 illustrates the TEM images of laser ablated HfO_2, which contains both NPs and NRs. As seen from the histograms shown in Fig-3.15 right hand side, a wide distribution of sizes (5 to 100 nm) was observed for all the input energies. The average NP size varied from 13.5 nm to 18.8 nm with increasing laser energies (200 µJ to 500 µJ). The right-hand bottom side of Fig-3.15(a-d) depicts the high-resolution TEM images clearly indicate that the NPs have extended to form NRs. It is also observed that the density of NRs increases with increase in laser energy, which were found to be amorphous. Similar observations of nano-chain formation in various materials ablated in water environment have been reported elsewhere [76, 77]. The probable reason for the observed nano-chain formation could be due to collision induced-

aggregation and laser induced-sintering [78]. A few other studies of the occurrence of nano-chains in water environment are attributed to the quenching of plasma plume generated during the laser ablation process [79]. The growth mechanism of nano-chains/nano-ribbons may not be due to the vapor-liquid-solid [80, 81] process, in which catalytic assisted mechanism plays a vital role in the formation of nano-chains/nanoribbons. Normally the metal NPs act as catalyst active sites but in the present case, no metal was used. The growth of nano-chains could be a vapor-solid process [82], in which vapor was produced from the HfO_2 target due to the high-temperature plasma generated at the target liquid surface and gets deposited as nanoclusters through the aggregation near to the target surface. As the ablation progresses, continuously emitting plasma generates more HfO_x vapor and results in the formation of more nanoclusters, which are favorable sites for adhesion of additional HfO_x molecules and consequently result in the formation of NRs [83]. However, the exact mechanism of NRs formation is still unclear and, therefore, needs more systematic studies. The phase of the HfO_x nanostructures is comprehended using HRTEM and SAED data, which is presented in Fig-3.16(a-d). Fig-3.16(a) illustrates the SAED pattern of HfO_x NPs which confirms the monoclinic phase with 'd' spacings of 0.28 nm, 0.31 nm, corresponding to the planes of (111) and (-111) at lower laser energies. Fig-3.16(b) and Fig-3.16(c) illustrate the SAED patterns clearly suggesting the existence of rhombohedral and hexagonal phases in samples ablated at higher laser energies. Fig-3.16(d) depicts the HRTEM image and the'd' spacing's of 0.48 nm and 0.44 nm corresponding to the planes of (100) and (101) respectively, of hexagonal HfO_2. Furthermore, the EDS data also confirmed the Hf/O ratio of 45.6/54.4 at lower energy and 78.6/21.4 at higher energy. We have also observed that at lower input energies the NPs exhibited monoclinic polycrystalline nature while for higher input energies, pure crystalline nature with a combination of monoclinic and hexagonal structures are seen. Therefore, we believe that that the fs laser ablation of HfO_2 pellets in deionized water leads to the formation of HfO_2 NPs when ablated at lower input energies whereas Hf (metal) rich (like Hf_6O) NPs are formed at higher energies in otherwise same conditions. We believe that this is an important result that provides useful information to understand the basic process of ultrafast laser ablation of oxide materials in liquids.

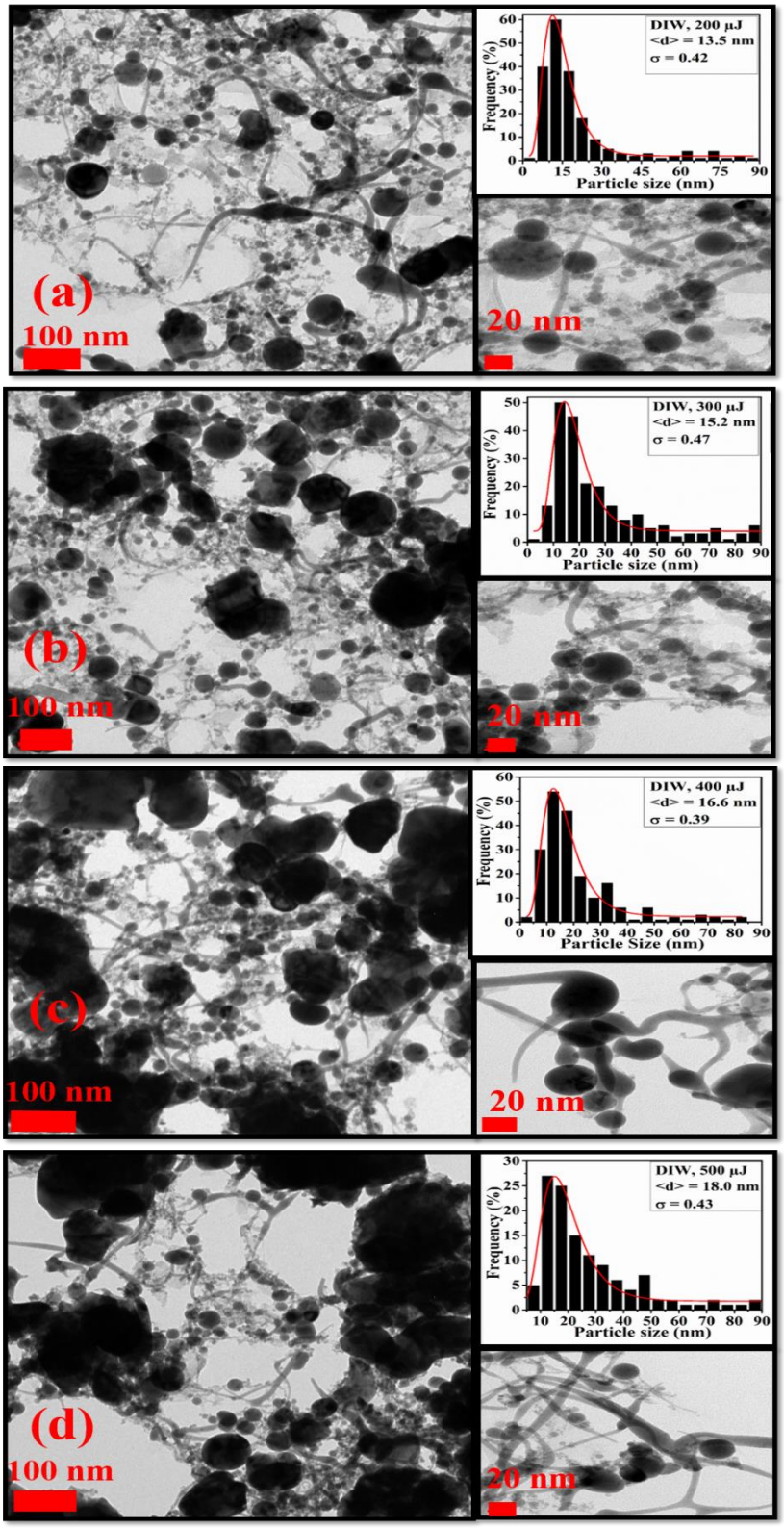

Fig-3.15: TEM images of HfO_2 NPs synthesized in DIW at different laser energies a) 200 µJ b) 300 µJ c) 400 µJ and d) 500 µJ. The right side of each image depicts the corresponding size distribution histograms and below are the high-resolution TEM images illustrating the NRs. <d> represents the average nanoparticle diameter while 'σ' represents the deviation.

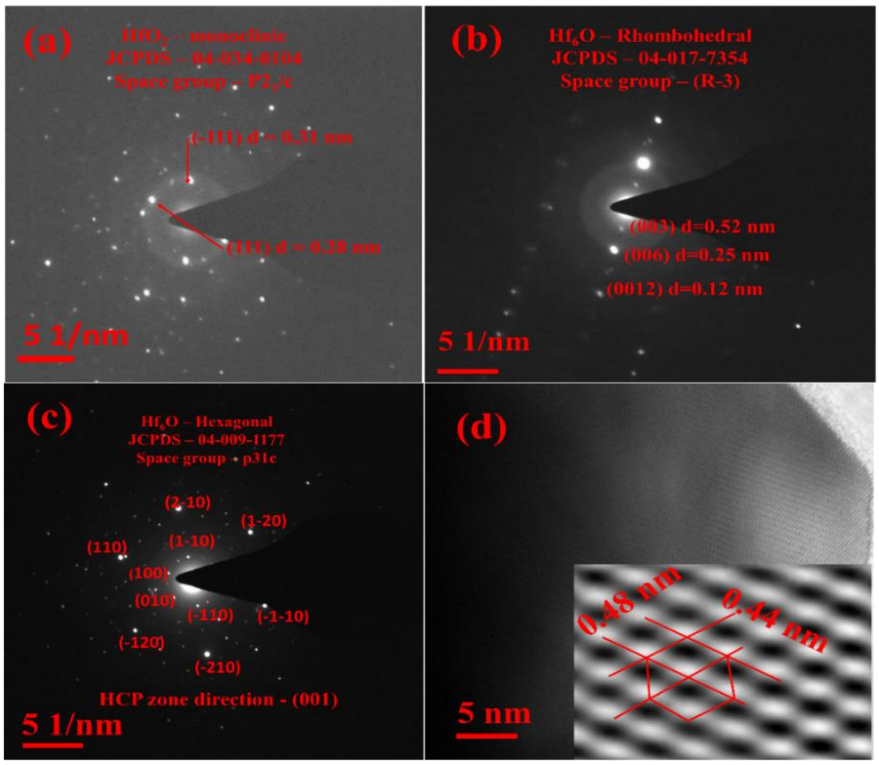

Fig-3.16: (a), (b), (c) SAED patterns of monoclinic, rhombohedral, hexagonal structures, respectively (d) HRTEM images of HfO_2 NPs. Inset of (d) shows IFFT pattern.

The metallic nature of NPs generated at higher input energies needs to be thoroughly investigated. The advantage with the present technique is that the produced NPs are bare and possess ligand-free surfaces, which is desirable and beneficial in high-*k* dielectric applications. HfO_2 exhibits distinct phases depending on the synthesis conditions: some are pressure-induced phase transitions [84] while others are temperature-induced phase transitions [85]. All these phase transitions are dependent on Hf and O concentration levels as well.

GIXRD measurements have been performed on HfO_x NPs drop casted on Si substrates, and GIXRD patterns are shown in Fig-3.17. For lower energies of 200 µJ and 300 µJ, the NPs exhibited monoclinic phase. Further increase in the energy to 400 µJ and 500 µJ has resulted in the combination of monoclinic and hexagonal phase for the generated NPs. GIXRD patterns strongly support the observations from HRTEM and SAED data which demonstrated distinct phases of HfO_2 at different laser fluences. The 2θ values at 28.3º and 31.5º confirm the monoclinic phase of the corresponding (-111) and (111) planes of HfO_2. These peaks match well with JCPDS file # 01-006-0318 (monoclinic HfO_2). The 2θ values of 35.2º and 44.2º confirm the presence of hexagonal phase, which is noticed for higher energies. These peaks again match well with JCPDS file #01-078-5817 (hexagonal Hf_6O). The GIXRD data

coordinated well with the hexagonal Hf_6O ratios. TEM and EDS (energy dispersive spectroscopy) data confirmed that the hafnium-rich oxide nanostructures are formed by laser ablation at higher energies. Several theoretical studies [86-88] have predicted the occurrence of Hf_6O and other binary hafnium oxides (e.g. Hf_8O_7) at very high pressures, which can possibly be present during high energy ablation using fs pulses. Further detailed studies are essential to confirm the formation of these unusual and exotic structures.

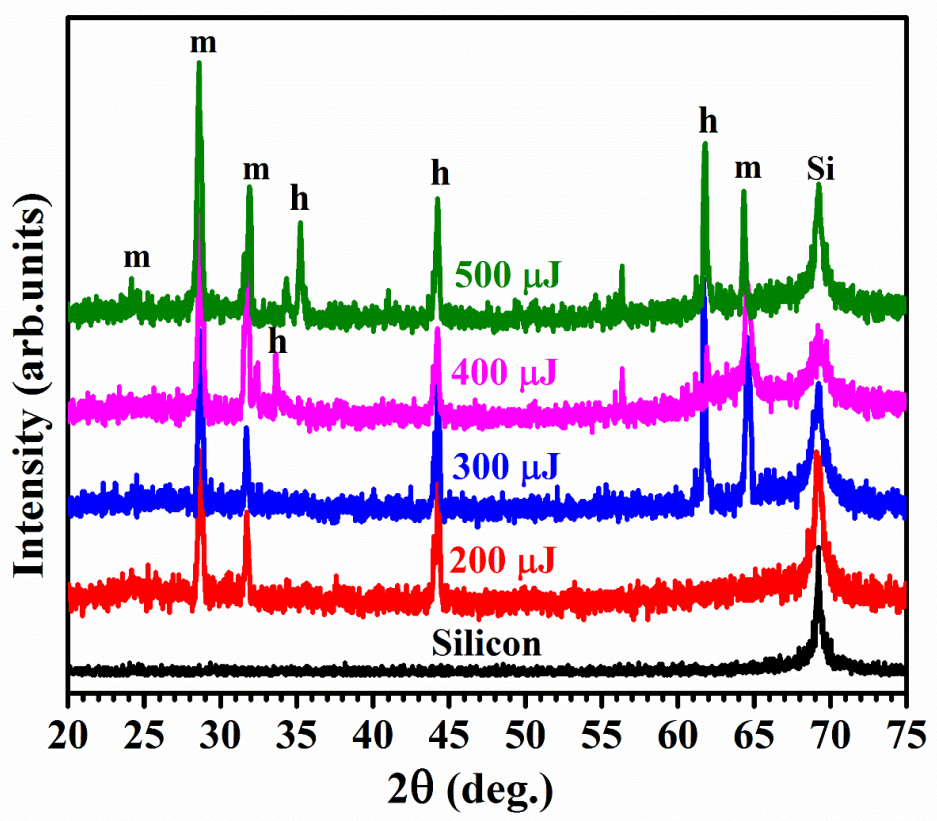

Fig-3.17: GIXRD spectra of HfO_2 NPs prepared at different laser energies and drop casted on Si substrates (m- monoclinic, h- hexagonal structures).

Hafnium oxide exhibits a total of about 36 vibrational modes. However, among those 18 modes (9 A_g+9 B_g) are Raman active, 15 modes (8 A_u+7 B_u) are IR active and remaining 3 modes are acoustic vibrations [89]. The monoclinic phase of HfO_2 exhibits all the 18 vibration modes and tetragonal phase exhibits 3 IR and 3 Raman modes [90]. Micro Raman spectra of the HfO_2 NPs drop casted on Si substrates are shown in Fig-3.18. The Raman peaks observed at 300 and 521 cm^{-1} represent the characteristic lines of Si and the corresponding FWHM is ~3.4 cm^{-1}. Bulk HfO_2 Raman peak at 523 cm^{-1} matched exactly with the monoclinic phase of HfO_2 [42-44]. We have observed a deviation of 2-4 cm^{-1} for each peak in HfO_x NPs with respect to those of pure HfO_2. Monoclinic HfO_2 NPs exhibited a peak at 523 cm^{-1} that is beneath the dominant Si 521 cm^{-1} peak. The experimental and theoretical calculations of HfO_2 vibrational modes for

monoclinic, tetragonal, orthorhombic and cubic phases have been reported in the literature [91-94]. However, in the present work, we have not observed any tetragonal, cubic or orthorhombic phases. For the input energies of 300 µJ and 400 µJ, the Raman peak positions agreed with the original peaks, but the intensity ratios were different. For the case of 500 µJ input energy, the two dominant peaks at 136 and 152 cm^{-1} merges into a single peak at 144 cm^{-1}. Similarly, the peaks at 244 and 258 cm^{-1} merge and produce a dominant peak at 250 cm^{-1}. All the major peaks observed are indexed along with the Silicon peak near 521 cm^{1}. Most of the observed lower vibrational modes correspond to metal (Hf) and at higher range modes are oxygen dominated modes. According to the existing reports [95-96], the higher order modes concur with the original results while lower modes merge and yield a dominant peak as a function of Hf content and laser ablation energy.

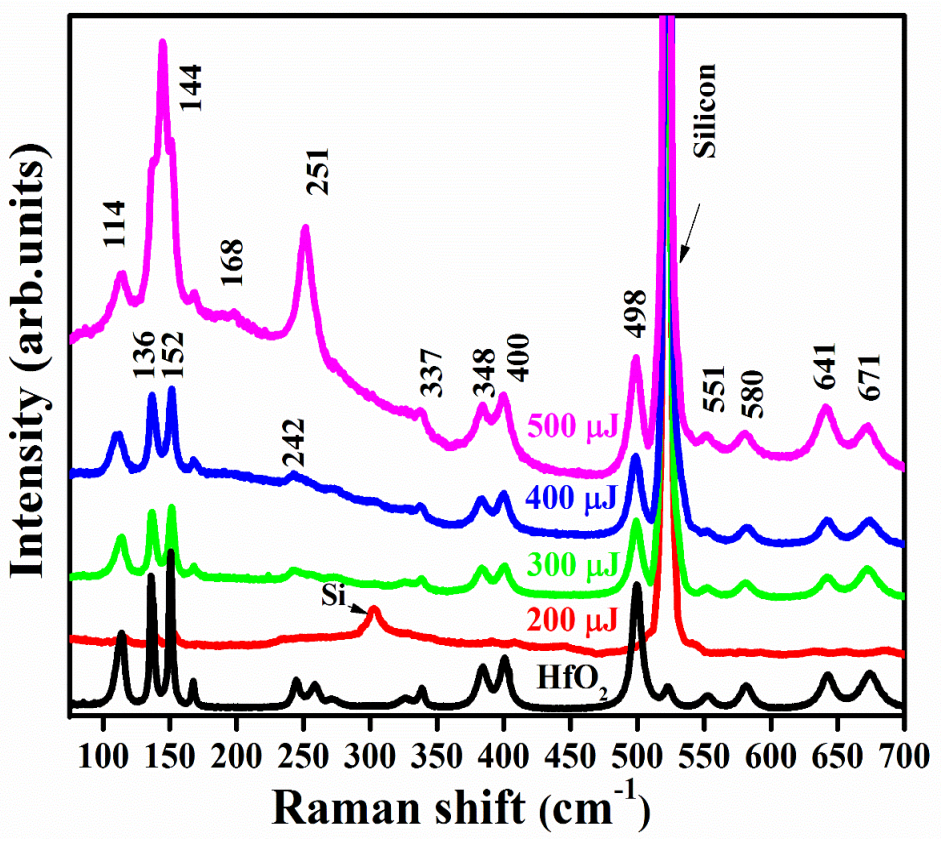

Fig-3.18: Raman spectra of HfO_2 NPs prepared at different laser energies and drop casted on Si substrates.

6.4 Conclusion

Pure HfO_2 films were deposited by RF magnetron sputtering. Investigations suggest the formation of 5-7 nm of amorphous HfO_2 NPs. Whereas in the case of HfO_2: Si co-sputtering, chain-like nanostructures were formed when 30 % of the HfO_2 target was covered with Si while

depositing. In the above two cases, the formation of NPs and chain like structures might be due to effect of deposition conditions of the RF magnetron sputtering system and the nature of substrate. The $HfSiO_x$ nano-clusters of 10-12 nm in size were formed and these nanoclusters got connected with other clusters in such a way that nano-chains were formed. When subjected to 100 MeV Ag ion irradiation, Si NPs were formed within the nano-chains. The Si NP size increases from 5.1 to 8.3 nm with an increase in ion fluence. The luminescence at 420 nm is attributed to 'O' related defects in HfO_2. The luminescence peak at 530 nm is attributed to embedded Si NPs within HfO_2 matrix and redshift indicates the increase in the NP size with increase in irradiation fluence.

Whereas in the case of HfO_2: Ag multilayers, metal NPs size increases with ion fluence and the calculated particle size from GIXRD, FESEM and TEM are in agreement with each other. Even though the Ag NP size increases with ion fluence, SPR is blue shifted in absorption spectra. The blue shift in SPR peak might be due to SHI induced changes in the dielectric constant of the host matrix. Surface HfO_2 grain size decreases due to ion-induced grain fragmentation. These results provide useful information to understand the effects of ion irradiation induced synthesis and modification of nanoparticles. The observed stable and visible luminescence from core-shell structures may find practical applications.

HfO_2 NPs are fabricated in DIW using fs laser ablation with varying input pulse energies. The size of HfO_2 NPs increases from 13.5 nm to 18 nm with increase in laser energy (200-500 μJ). Along with NPs, 10-20 nm wide and few hundred nm long NRs were also observed. The NRs density increases with increasing input energy. At lower input energy, HfO_2 NPs exhibited monoclinic structure and at higher energy both monoclinic and hexagonal structures were observed, indicating the formation of a new phase (Hf_6O) which is otherwise formed at high pressures. This result provides useful information of understanding ion and laser interaction with nanomaterials.

6.5 References

1. L. Khomenkova, X. Portier, J. Cardin and F. Gourbilleau, *Nanotechnology*, **21,** 285707 (2010).
2. Moore, Gordon E, *Electronics.* **38**, 8, 33-35 (1965).
3. Buhro W.E. and Colvin V.L, *Nat. Mater*, **2**, 138-139 (2003).
4. Yu-Hsien Lin, Hsin-Chiang You, Jin-Shi Hong, Jay-Chi Chou, Jyun-Hong Shih, *Advances in Information Sciences and Service Sciences*, **4**, 18-26 (2012).

5. Joel Molina, Carlos Zuniga, Edmundo A. Gutierrez, Wilfrido Calleja, Pedro Rosales, Francisco J. Hidalga and Alfonso T, *Trans. Mat. Res. Soc. Japan.* **38,** 569-572 (2013).
6. Joel Molina, Ana Luz Munoz, Wilfrido Calleja, Pedro Rosales, Alfonso Torres, *J. Mater. Sci*, **47,** 2248–2255 (2012).
7. F L Martınez, M Toledano-Luque, J J Gandıa, J Carabe, W Bohne, J Rohrich, E Strub and I Martil, *J. Phys. D: Appl. Phys*, **40,** 5256–5265 (2007).
8. Lionel Trojman, *IEEE Trans. Electron Devices*, **61,** 3632-3638 (2014).
9. Eun-Chel Cho, Martin A. Green, Gavin Conibeer, Dengyuan Song, Young-Hyun Cho, Giuseppe Scardera, Shujuan Huang, Sangwook Park, X. J. Hao, Yidan Huang, and Lap van Dao, *Advances in Opto. Elec.* **11,** 69578, 1-11 (2007).
10. Canham LT, *Appl. Phys. Lett,* **57,** 1046-1048 (1990).
11. Souvik Mahapatra, S. Shukuri, and Jeff Bude, *IEEE Trans. Electron Devices*, **49,** 1302-1307 (2002).
12. T. Chulapakorn, I. Sychugov, S. S. Suvanam, J. Linnros, M. Wolff, D. Primetzhofer, G. Possnert, and A. Hallén, *Phys. Status. Solidi. C,* **12** 1301–1305 (2015).
13. Jianyong Ouyang, *Org. Ele.* **14,** 1458–1466 (2013).
14. Weibo Cai, Ting Gao, Hao Hong, Jiangtao Sun, *Nanotech. Sci. and Appl.* **1,** 17-32 (2008).
15. Monika Benkovicova, Karol Vegso, Peter Siffalovic, Matej Jergel, Stefan Luby, Eva Majkova, *Thin Solid Films*, **543,** 138–141 (2013).
16. Zengtao Liu, Chungho Lee, Venkat Narayanan, Gen Pei, and Edwin Chihchuan Kan, *IEEE Trans. Electron Devices*, **49**, 1606-1613 (2002).
17. Jung Yup Yang, Ju Hyung Kim, Won Joon Choi, Young Ho Do, Chae Ok Kim, and Jin Pyo Hong, *J. Appl. Phys*. **100** 066102, 1-3 (2006).
18. Ch Sargentis, K Giannakopoulos, A Travlos and D Tsamakis, *J. Phy.: Conference Series,* **10,** 53–56 (2005).
19. F. M. Yang, T. C. Chang, P. T. Liu, U. S. Chen, P. H. Yeh, Y. C. Yu, J. Y. Lin, S. M. Sze and J. C. Lou *Appl. Phys. Lett.* **90,** 222104, 1-3 (2007).
20. M. Bayle, C. Bonafos, P. Benzo, G. Benassayag, B. Pécassou, L. Khomenkova, F. Gourbilleau, and R. Carles, *Appl. Phys. Lett.* **107**, 101907, 1-5 (2015).
21. S. Tiwari, F. Rana, H. Hanafi, A. Hartstein, E.F. Crabbe, K. Chan, Appl. Phys. Lett. **68,** 10-16 (1996).
22. Chris M. Fancher, Lili Zhao, Matthew Nelson, Ligang Bai, Guoyin Shen and Jacob L. Jones, *J. Appl. Phys.* **117,** 234102, 1-5 (2015).

23. Johannes Müller, Tim S. Böscke, Uwe Schröder, Stefan Mueller, Dennis Brauhaus, Ulrich Böttger, Lothar Frey, and Thomas Mikolajick, *Nano. Lett.* 12, 4318−4323 (2012).
24. Dong Hou, Chris M. Fancher, Lili Zhao, Giovanni Esteves, and Jacob L. Jones, *J. Appl. Phys*. **117**, 244103,1-5 (2015).
25. D. A. Neumayer and E. Cartier, *J. Appl. Phys*. **90**, 1801 -1808 (2001).
26. K. Chang, K. Shanmugasundaram, J. Shallenberger, and J. Ruzyllo, *Thin Solid Films*, **515,** 3802-3809 (2007).
27. Rimpy Shukla, C. Summonte, M. Canino, M. Allegrezza, M. Bellettato, A. Desalvo, D. Nobili, S. Mirabella, N. Sharma, M. Jangir, I. P. Jain, *Adv. Mat. Lett.* **297**, 304-309 (2012).
28. F Delachat, M Carrada, G Ferblantier, J-J Grob and A Slaoui, *Nanotechnology*, **20**, 415608, 1-5 (2009).
29. Tsutomu Shimizu-Iwayama, Norihiro Kurumado, David E. Hole, and Peter D. Townsend, *J. Appl. Phys*. **83**, 6018-6022 (1998).
30. P. Kluth, B. Johannessen, G. J. Foran, D. J. Cookson, S. M. Kluth, and M. C. Ridgway, *Phys. Rev. B*, **74**, 014202, 1-9 (2006).
31. V. Saikiran, N. Srinivasa Rao, G. Devaraju, A.P. Pathak, *Nucl. Instr. Meth. Phys. Res. B*, **323,** 14–18 (2014).
32. T. Chulapakorn, I. Sychugov, S. S. Suvanam, J. Linnros, M. Wolff, D. Primetzhofer, G. Possnert, and A. Hallén, *Phys. Status Solidi. C*, **12,** 1301–1305 92015).
33. Yukari Ishikawa, N. Shibata, and S. Fukatsu, *Appl. Phy. Lett.* **72,** 2592-2594 (1998).
34. V. Saikiran, V.S. Vendamani, S. Hamad, S.V.S. Nageswara Rao, S. Venugopal Rao, A.P. Pathak, *Nucl. Instr. Meth. Phys. Res. B*, **333,** 99–105 (2014).
35. L. Maggiorella, G. Barouch, C. Devaux, A. Pottier, E. Deutsch, J. Bourhis, E. Borghi and Laurent Levy, *Future Oncol.* **8**, 1167–1181 (2012).
36. J. Shim, J. Rivera and R. Bashir, *Nanoscale* **21,** 10887-10893 (2013).
37. M. Lee, A. Baraket, N. Zine, M. Zabala, F. Campabadal, N. Jaffrezic-Renault and A. Errachid, *Sensors & Transducers.* **27**, 233-238 (2014).
38. T.L. McGinnity, O. Dominguez, T.E. Curtis, P.D. Nallathamby, A.J. Hoffman and R.K. Roeder, *Nanoscale*, **8,** 13627–13637 (2016).
39. L. Maggiorella, G. Barouch, C. Devaux, A. Pottier, E. Deutsch, J. Bourhis, E. Borghi and L. Levy, *Future Oncol.* **8**, 1167-1181 (2012).

40. N. Kumar, B.P.A. George, H. Abrahamse, V. Parashar, S.S. Ray and J. C. Ngila, *Sci. Rep.* **7**, 9351 (2017).
41. W. Zhou, S.V. Ushakov, T. Wang, J.G. Ekerdt, A.A. Demkov, and A. Navrotsky, *J. Appl. Phys.* **107**, 123514 (2010).
42. K.K. Bharathi, N. R. Kalidindi, and C. V. Ramana, *J. Appl. Phys.* **108** (2010) 083529.
43. M. Dhanunjaya, S. A. Khan, A. P. Pathak, D. K. Avasthi and S. V. S. Nageswara Rao, *J. Phys. D: Appl. Phys.* **50**, 505301 (2017).
44. Xiaoli Liu, Yuanzhi Chen, Laisen Wang, and Dong Liang Peng, *J. Appl. Phys.* **113**, 076102 (2013).
45. M. A. Pugachevskii, and V. I. Panfilov, *J. Appl. Spectroscopy*, **81**, 640-643 (2014).
46. N. G. Semaltianos, J. M. Friedt, R. Chassagnon, V. Moutarlier, V. Blondeau-Patissier, G. Combe, M. Assoul, and G. Monteil, *J. Appl. Phys.* **119**, 204903 (2016).
47. V. S. Vendamani, S. Hamad, V. Saikiran, A. P. Pathak, S. Venugopal Rao, V. V. Ravi Kanth Kumar, S. V. S. Nageswara Rao, *J. Mater. Sci.* **50**, 1666–1672 (2015).
48. G.K. Podagatlapalli, S. Hamad, and S. Venugopal Rao, *J. Phys. Chem. C* **119**, 16972–16983 (2015).
49. S. Hamad, G. Krishna Podagatlapalli, M.A. Mohiddon, and S. Venugopal Rao, *Appl. Phys. Lett.* **104**, 263104 (2014).
50. D. Zhang, B. Gökce, S. Barcikowski, *Chem. Rev.* **117,** 3990-4103 (2017).
51. J. Xiao, P. Liu, C.X. Wang, G.W. Yang, *Prog. Mater. Sci.* **87,** 40–2201 (2017).
52. H. Zeng, X.-W. Du, S.C. Singh, S.A. Kulinich, S. Yang, J. He, and W. Cai, Adv. *Funct. Mater.* **22**, 1333–1353 (2012).
53. D. Zhang, J. Liu, P. Li, Z. Tian, C. Liang, *Chem. Nano. Mat.* **3**, 512-533 (2007).
54. J. F. Ziegler, "SRIM-2003". *Nucl. Instr. Meth. B.* **1027**, 219-220 (2004).
55. S. Venugopal Rao, G. K. Podagatlapalli, and S. Hamad, *J. Nanosci. Nanotechnol.* **14**, 1364-1388 (2014).
56. M Dhanunjaya, S A Khan, A P Pathak, D K Avasthi and S V S Nageswara Rao, *J. Phys. D: Appl. Phys.* **50** 505301, 1-8 (2017).
57. P. Scherrer, *Göttinger Nachrichten Gesell.*, **2**, 98 (1918).
58. T. V. Perevalov, V. Sh. Aliev, V. A. Gritsenko, A. A. Saraev, V. V. Kaichev, E. V. Ivanova and M. V. Zamoryanskaya, *Appl. Phys. Let.* **104**, 071904, 1-4 (2014).
59. T. V. Perevalov, D. V. Gulyaev, V. S. Aliev, K. S. Zhuravlev, V. A. Gritsenko, and A. P. Yelisseyev, *J. Appl. Phys.* **116**, 244109, 1-4 (2014).

60. D. R. Islamov, V. A. Griteinko and T. V. Perevalov, *ECS Transaction,* **69,** 197-203 (2015).
61. D. Muñoz Ramo, J. L. Gavartin, and A. L. Shluger, *Phys. Rev. B,* **75,** 205336, 1-12 (2007).
62. N. Manikanthababu, M. Dhanunjaya, S.V.S. Nageswara Rao, A.P. Pathak, *Nucl. Instr. Meth. Phys. Res. B*, **379,** 230–234 (2016).
63. Steffen Hallmann, Mark J. Fink, and Brian S. Mitchell, *J. Mater. Res.*, **26**, 8 (2011).
64. T. G. Ulusoy Ghobadi, A. Ghobadi, T. Okyay, K. Topalli and A. K. Okyay, *RSC Adv.* **6**, 112520–112526 (2016).
65. R. S. Knox, Theory of excitons, Solid state physics (Ed. by Seitz and Turnbul, Academic, NY, 5, (1963).
66. Sachin Kumar, Animesh K. Ojha, *Journal of Alloys and Compounds* **644**, 654–662 (2015).
67. S. A. Elizia´rio, L. S. Cavalcante, J. C. Sczancoski, P. S. Pizani, J. A. Varela, J. W. M. Espinosa, E. Longo, *Nanoscale Res Lett* **4**, 1371–1379 (2009).
68. R. Singhal, J.C. Pivin, R. Chandra, D.K. Avasthi, *Surface & Coatings Technology*, **229**, 50–54 (2013).
69. R. Singhal, D.C. Agarwal, Y. K. Mishra, S. Mohapatra, D.K. Avasthi, A.K. Chawla, R. Chandra, J.C. Pivin, *Nucl. Instr. Meth. Phys. Res. B*, **267,** 1349–1352 (2009).
70. van de Hulst, H. C., Light Scattering by Small Particles Dover Publication p 470 (1981).
71. Mulvaney, P, *Langmuir,* **12**, 788-800 (1996).
72. Gans, R. v., Uber die, *Ann. Phys.* **37**, 881-900 (1912).
73. Shawkat Salameh Gasaymeh, Shahidan Radiman, Lee Yook Heng, Elias Saion and G. H. Mohamed Saeed, *Afric. Phys. Rev. B*, **4** 0006 (2010).
74. R. Singaravelan, S. Bangaru Sudarsan Alwar, Appl Nanosci, **5**, 983–991 (2015).
75. M. Bayle, C. Bonafos, P. Benzo, G. Benassayag, B. Pécassou, L. Khomenkova, F. Gourbilleau, and R. Carles, *Appl. Phys. Lett.* **107**, 101907 (2015).
76. T.X. Phuoc, *J. Mater. Sci. & Nanotech.* **2,** 1-7 (2014).
77. V. S. Vendamani, A. Tripathi, A.P. Pathak, S. Venugopal Rao, A. Tiwari, *Mater. Lett.* **192**, 29-32 (2017).
78. H. He, W. Cai, Y. Lin and B. Chen, *Chem. Commun.,* **46,** 7223-7225 (2010).
79. O.V. Overschelde, J. Dervaux, L. Yonge, D. Thiry and R. Snyders, *Laser Phys.* **23,** 055901 (2013).
80. R.S. Wagner and W. C. Ellis, *Appl. Phys. Lett.* **4,** 89-90 (1964).

81. Z. R Dai, J. L. Gole, and Z. L. Wang, *J. Phys. Chem.* B. **106**, 1274-1279 (2002).
82. J. Q. Hu, Y. Bando, Q.L. Liu, D. Golberg, *Adv. Funct. Mater*. **13**, 493-496 (2003).
83. Y. Al-Khatatbeh, K.K.M. Lee, and B. Kiefer, *Phys. Rev. B* **82**, 144106 (2010).
84. J. Zhang, A. R. Oganov, X. Li, H. Dong, and Q. Zeng, *Phys. Chem. Chem. Phys*. **14**, 17301-17310 (2015).
85. J. Zhang, A.R. Oganov, X. Li, K.-H. Xue, Z. Wang, and H. Dong, *Phys. Rev. B* **92**, 184104 (2015).
86. P. Blaise and B. Traore, arXiv:1511.07665v1, (2015).
87. L. Bayarjargal, W. Morgenroth, N. Schrodt, B. Winkler, V. Milman, C. R. Stanek and B. P. Uberuaga, *High Pressure Research*, **37,** 147-158 (2017).
88. N. Selvakumar, H.C. Barshilia, and K. S. Rajam, *Solar Energy Materials and Solar Cells.* **94,** 1412- 1420 (2010).
89. X. Zhao and D. Vanderbilt, *Phys. Rev. B* **65,** 233106 (2002).
90. M. Yashima, H. Takahashi, K. Ohtake, T. Hirose, M. Kakihana, H. Arashi, Y. Ikuma, Y. Suzuki and M. Yoshimura, *J. Phys. Chem. Solids.* **57,** 289-295 (1996).
91. P.E. Quintard, P. Barbe´ris, A.P. Mirgorodsky, and T. Merle-Mejean, *J. Amer. Ceram. Soc.* **85,** 1745-1749 (2002).
92. A. Jayaraman, S. Y. Wang, and S. K. Sharma, L. C. Ming, *Phys. Rev. B*. **48,** 9205-9211 (1993).
93. J.S. Quintero-García, B.A. Puente-Urbina, L.A. García-Cerda, O.S. Rodríguez-Fernández, E. Mendoza-Mendoza, *Mater. Lett.* **159,** 520–524 (2015).
94. S.N. Tkachev, M.H. Manghnani, A. Niilisk, J. Aarik, H. Mandar, *J. Mater. Sci.* **40,** 4293-4298 (2005).
95. V. Jayaraman, G. Bhavesh, S. Chinnathambi, S. Ganesan, and P. Aruna, *Mater. Express*, **4,** 375-383 (2014).
96. B. Zhou, H. Shi, X. D. Zhang, Q. Su, and Z. Y. Jiang, *J. Phys. D: Appl. Phys.* **47,** 115502 (2014).

Conclusions and Scope of Future Work

This chapter presents a brief note on overall conclusion of the thesis. Possible future directions are also discussed.

7.1 Conclusions

In this thesis we have discussed our results on the fabrication of Hafnium Oxide (HfO_2) thin films, SHI irradiation induced modifications of HfO_2 thin films, and Nanoparticles (NPs) embedded in HfO_2 matrix.

Initially, we have deposited HfO_2 films by RF magnetron sputtering method at different deposition conditions like deposition power, pressure and different annealing temperatures. All the deposited samples were characterized and investigated using several techniques. We noticed that with increasing the RF power, the film thickness increases linearly. Lower RF powers gave low deposition rates and higher RF powers gave higher deposition rates. Along with that we noticed lower RF power grown films have shown good morphology and higher RF power grown films shown irregular grain growth. From the above observations, moderate RF powers are suitable for further work. Then, we kept the deposition power constant and varied the deposition pressure. We noticed that with increase in the deposition pressure, the film thickness decreases, the grain size decreases and the porosity of the film increases. From the above observation, we conclude that lower deposition pressure is more suitable to get better morphology with moderate film thickness. As deposited films have shown amorphous nature and after annealing at higher temperatures, these films got transformed to monoclinic phase.

From the above optimized conditions, we have synthesized thin HfO_2 films of thickness about 15 nm deposited by using RF Magnetron sputtering method. Initial observation shows that these films are amorphous in nature. These thin films consist of non-spherical nanoclusters of size about 2.6 nm. After irradiation, we noticed that the same nanoclusters were transformed into crystalline, non-agglomerated and well dispersed spherical crystallites. The characterization techniques like XRD and TEM confirm the phase transformations and particle size growth. This growth of nanoparticles is attributed to the agglomeration of surrounding NPs

by ion induced diffusion process. The defect configuration is also found to change after SHI irradiation as seen from the PL emission spectra. We have used thermal spike model to explain the above observed SHI induced results. These results give useful information for understanding the ion induced crystallization of NPs in general and HfO_2 NPs in particular.

Similarly, we have deposited thick HfO_2 films of thickness about 500 nm using the same RF magnetron sputtering method at higher powers. The as-deposited film show monoclinic phase and self-oriented nano-flake structures because of the high deposition rates and film growth conditions. We have performed the SHI irradiation on these films. XRD, FESEM, and PL confirm the phase transformation, grain fragmentation and defect annihilation in SHI irradiated films. Using the GIXRD spectra, ion induced damage cross sections and ion induced track radius have been estimated. In this case of thick films also, we observed the ion induced defect reconfiguration. As discussed earlier these defects are mid-bandgap electron trap centers. Ion-induced heat desorption and anisotropic thermal expansion in the nano-grains are expected to cause the observed grain fragmentation. All these observed effects are expected due to electronic energy loss induced sharp rise of thermal gradient.

Similarly, we have studied the SHI induced effects on the embedded nanoparticles in HfO_2 matrix. $HfSiO_x$ composite films were deposited using RF magnetron sputtering method as discussed in the above section. With SHI irradiation, Si NPs were formed with the composite films. These Si NPs size increases with ion fluence as studied in the literature. Similarly, we have deposited the $Ag/HfO_2/Ag$ multilayer thin films using e-beam deposition. As expected embedded Ag NPs were formed within the HfO_2 matrix after SHI irradiation. Quietly, Ag NPs induced SPR peak blue shifted even though the size of NPs increases. This effect is due to the effect of change in dielectric constant of the host matrix. These results provide useful information to understand the effects of ion irradiation induced synthesis and modification of nanoparticles. Along with these we have fabricated the HfO_2 NPs using laser ablation method in DIW. The HfO_2 NPs size increases from 13.5 nm to 18 nm with increase in laser energy. With the increase in the laser fluence, a new phase (Hf_6O) is nucleated.

7.2 Scope of Future Work

Metal (Au, Ag, and Pt etc.) and Semiconductor (Si, and Ge) nanoparticles embedded in dielectric matrix have generated significant interest in electronics (storage memory) applications and opto-electronic applications. These studies are important because, we know that HfO_2 has replaced the SiO_2 as a gate dielectric material in the microelectronics. The NPs

embedded in HfO_2 dielectric matrix are currently under extensive investigations due to their potential application in non-volatile memory devices. We have achieved the fabrication of HfO_2 thin films and studied the SHI irradiation effects. We have achieved the fabrication of metal (Ag) and semiconductor (Si) NPs and control on their size and shape embedded in HfO_2 matrix with the assistance of SHI irradiation. The preliminary investigations are initiated and those are in progress. To understand more about ion induced phase changes, studies can be extended to investigate the HfO_2 based phase change memory applications. Still there is a room to study the different type of NPs embedded in HfO_2 matrix and these are open challenges for the scientific society. From all the above investigations, there is a possibility to use SHI irradiation as an interesting tool to modify the material and to control the nanoparticle embedded thin films in various materials.

List of Publications

1. **M. Dhanunjaya**, S.A. Khan, A. P. Pathak, D.K. Avasthi and S. V. S. Nageswara Rao, "Ion Induced Crystallization and Grain Growth of Hafnium Oxide Nano-particles in Thin-films deposited by Radio Frequency Magnetron Sputtering" *J. Phys. D: Appl. Phys.* 50, 505301 (2017).
2. **M. Dhanunjaya**, N. Manikanthababu, A. P. Pathak and S. V. S. Nageswara Rao, "Effect of Growth Rate on Crystallization of HfO_2 Thin Films Deposited by RF Magnetron Sputtering" *AIP Conference Proceedings* 1731, 080071 (2016).
3. V. S. Vendamani, Saif A Khan, **M. Dhanunjaya**, A. P. Pathak and S.V.S. Nageswara Rao, "An Energetic ion induced desorption of hydrogen from porous silicon studied by on-line elastic recoil detection analysis", *Microporous and Mesoporous Materials*, **246**, 81-88 (2017).
4. N. Manikanthababu, **M. Dhanunjaya**, S. V. S. Nageswara Rao and A. P. Pathak, "SHI induced effects on the electrical and optical properties of HfO_2 thin films deposited by RF sputtering", Nucl. Inst. Meth. B 379, 230-234 (2016).
5. N. Manikanthababu, N. Arun, **M. Dhanunjaya**, S. V. S. Nageswara Rao and A. P. Pathak "Gamma irradiation induced effects on the electrical properties of HfO_2 based MOS devices" *Radiation Effects & Defects in Solids*, **171**, 1–2,77–86 (2016).
6. Andrey Baydin, Halina Krzyzanowska, **M. Dhanunjaya**, S.V.S. Nageswara Rao, Jimmy L. Davidson, Leonard C. Feldman, Norman H. Tolk, "Measurements of depth dependent modification of optical constants arising from H^+ implantation in n-type 4H-SiC using coherent acoustic phonons", *APL Photonics*, **1**, 036102 (2016).
7. N. Manikanthababua, N. Arun, **M. Dhanunjaya**, V. Saikiran, S.V.S. Nageswara Rao and A.P. Pathak, "Synthesis, characterization and radiation damage studies of high-k dielectric (HfO_2) films for MOS device applications", *Radiation Effects & Defects in Solids* **170**, 207 (2015).
8. **M. Dhanunjaya**, D.K. Avasthi, A. P. Pathak, S.A. Khan, and S. V. S. Nageswara Rao, "Grain Fragmentation and Phase Transformations in Hafnium Oxide induced by SHI Irradiation", (under review).
9. **M. Dhanunjaya**, A. P. Pathak and S. V. S. Nageswara Rao, "Silicon Nanoparticles Embedded in Hafnium Oxide Matrix and Swift Heavy Ion Induced Effects, (under review).

10. **M. Dhanunjaya**, Chandu Byram, Venugopal Rao Soma, V. S. Vendamani, A. P. Pathak and S. V. S. Nageswara Rao, "Hafnium Oxide Nanoparticles Fabricated by Femtosecond Laser Ablation in Water" (to be submitted).
11. **M. Dhanunjaya**, K. Vinod, S.A. Khan, A. P. Pathak, D. Kabiraj and S. V. S. Nageswara Rao "100 MeV Ag Ion Induced Silver Nanoparticles Embedded in Hafnium Oxide Matrix", (to be submitted).
12. **M. Dhanunjaya,** Venugopal Rao Soma, Chandu Byram, A. P. Pathak and S. V. S. Nageswara Rao, "Hafnium Oxide Nanoparticles Fabricated by Femtosecond Laser Ablation in Liquid Environment" (to be submitted).
13. **M. Dhanunjaya,** A. P. Pathak, and S. V. S. Nageswara Rao "Growth rate and thickness dependent phase change in HfO_2 thin films prepared by RF magnetron sputtering method", (Manuscript under preparation).

List of Attended Conferences

1. Attended and performed an **oral presentation** in 4th international conference Nano Structuring by Ion Beams (**ICNIB-2017**) organized by Devi Ahilya University at Indore, M.P, India, during 11th to 13th October 2017.
2. Attended and performed an **oral presentation** in 24th Conference on Application of Accelerators in Research and Industry **(CAARI-2016**) organized by University of North Texas, Sandia National Laboratories, and Los Alamos National Laboratory at FT. Worth, Texas, US during 30th October to 4th November 2016.
3. Attended and presented the **poster** in Radiation Effects in Insulators (**REI-18**) Conference conducted by MNIT-Jaipur, Rajasthan and IUAC, New Delhi during the period of October 26–31, 2015.
4. Participation and Poster presentation in the National Conference on Frontiers in Physics (FIP-2014) organized by School of Physics at University of Hyderabad during 17th - 18th October 2014.
5. Participated and worked as a volunteer in AP Science Congress 2013, at UoH, Hyderabad from 14th to 16th November 2013.
6. Participation and Poster presentation in the National Conference on Frontiers in Physics (FIP-2012) organized by School of Physics at University of Hyderabad during 27th - 29th September 2012.